Chem Soc Rev

Interfacing Proteins with Graphitic Nanomaterials: from Spontaneous Attraction to Tailored Assemblies

Journal:	*Chemical Society Reviews*
Manuscript ID:	CS-SYN-03-2015-000190.R2
Article Type:	Review Article
Date Submitted by the Author:	25-May-2015
Complete List of Authors:	De Leo, Federica; University of NAmur, Magistrato, Alessandra; CNR-IOM-Democritos c/o International School for Advanced Studies, Bonifazi, Davide; Facultes Universitaires Notre Dame de la Paix Rue, Chemistry Department

Chemical Society Review

– Critical Review –

Interfacing Proteins with Graphitic Nanomaterials: from Spontaneous Attraction to Tailored Assemblies

Federica De Leo[a], Alessandra Magistrato[b] and Davide Bonifazi[a,c]*

[a]) *Department of Chemistry and Namur Research College (NARC), University of Namur (UNamur), B-5000 Namur, Belgium. E-mail: davide.bonifazi@unamur.be*

[b]) CNR-IOM-Democritos c/o International School for Advanced Studies (SISSA), 34136, Trieste, Italy

[c]) *Dipartimento di Scienze Chimiche e Farmaceutiche and INSTM UdR Trieste, Università degli Studi di Trieste, 34127 Trieste, Italy*

Abstract Table of Contents
This *critical review* presents a detailed overview of the chemico-physical principles ruling the non-covalent association between proteins and the three most representative nanomaterials of the graphitic family, *i.e.* fullerene, carbon nanotubes and graphene. By sieving the most significant examples, we highlight how the topography of the carbon nanomaterials and the biomolecules' nature can mutually influence their way of interactions leading to fascinating and innovative hybrid materials for biotechnological applications.

TOC Figure

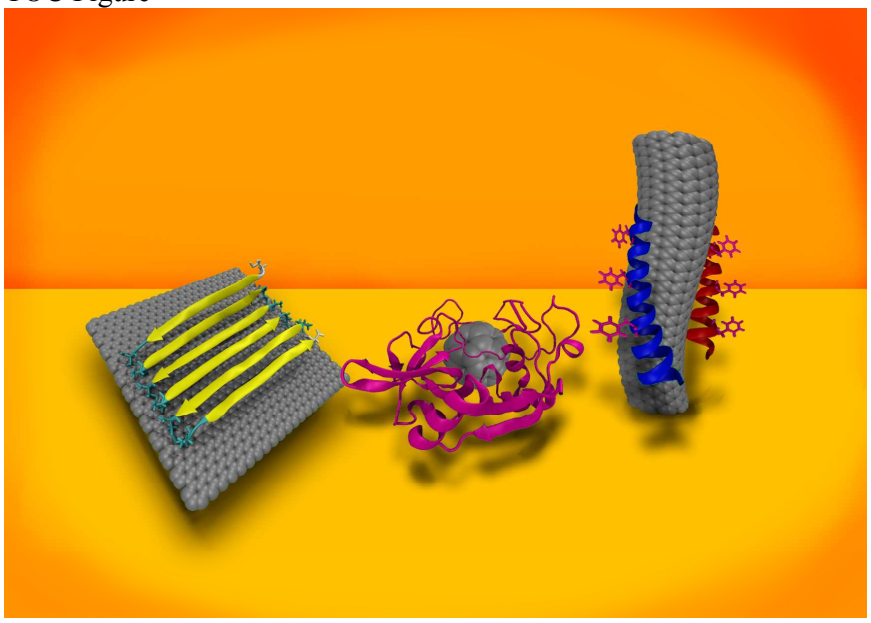

Table of Content

Abstract		**5**
1.	**Introduction**	**6**
1.2	Methodological approaches towards structured materials	*8*
2.	**Fullerene hybrids**	**10**
2.1	Fullerene and amino acids	10
2.2	Fullerene and polypeptides	12
2.3	Fullerene and proteins	16
3	**CNT hybrids**	**23**
3.1	CNT and amino acids	23
3.2	CNTs and polypeptides	28
3.3	CNTs and proteins	36
4.	**Graphene hybrids**	**45**
4.1	Graphene and amino acids	45
4.2	Graphene and polypeptides	56
4.3	Graphene and proteins	72
5.	**Conclusions**	**85**
6	**References**	**86**

Authors

Federica De Leo was born in S. Pietro Vernotico (Italy) in 1984. After obtaining her degree in Medicinal Chemistry in 2009 at the University of Parma, she moved to the University of Namur as Marie-Curie PhD fellow (2010-2014) under the supervision of Prof. D. Bonifazi. Since 2015, she is a post-doc in the group of Dr. G. Musco at S. Raffaele Scientific Institute. She spent one-year in the group of Dr. A. Magistrato at the SISSA (Trieste). She theoretically investigates the non-covalent interactions between biomolecules and nanomaterials and the chemico-physical properties of optoelectronic organic materials.

Alessandra Magistrato received her degree in chemistry in 1997 at the University of Perugia, Italy. She moved then to ETH-Zurich where she received the PhD in computational inorganic chemistry, working in the group of Prof. U. Roethlisberger in (1998-2001). In 2001-2003 she worked as post doc in the group of Prof. M.L. Klein at the University of Pennsylvania, Philadelphia, USA. Since 2006, she is permanent researcher of CNR-IOM@SISSA, Trieste, Italy. Her research interests are principally devoted to study the mechanism of pharmacologically relevant enzymes and of drug/DNA interactions via force field, ab initio and hybrid quantum-classical (QM/MM) molecular dynamics simulations.

Davide Bonifazi was born in Guastalla (Italy) in 1975. After obtaining the "Laurea" from the University of Parma (1999), working with Prof. E. Dalcanale, he joined the group of Prof. F. Diederich at the ETH-Zurich (2000–2004). He was awarded the Silver Medallion of the ETH (2005). After a post-doctoral stay with Prof. M. Prato, he joined the University of Trieste as part-time researcher. Since 2006, he has joined the University of Namur, where is a professor in organic chemistry. His research focuses on the synthesis of optelectronically-active molecules and their self-organisation at interfaces, porphyrin chemistry and functionalisation of carbon nanostructures.

Abstract

This *critical review* aims at giving insights on the spontaneous tendency of proteins and their constitutive parts to adsorb on graphitic nanomaterials (GNMs) through non-covalent interactions occurring at their interfaces. Specifically, it focuses on the theoretical and experimental studies carried out to comprehend in depth the forces ruling the adsorption processes of proteins on fullerene, carbon nanotubes and graphene. In a systematic way the reader is guided through the most recent and representative examples describing at the atomistic level of detail the structural modalities and the chemico-physical principles through which amino acids, polypeptides and folded proteins interact with GNMs' surface, thereby taking into consideration the mutual effects of both protein structural complexity and nanomaterial topology. Based on their chemical and structural features, the study and understanding of the protein/nanomaterial interfaces can be exploited in the view of design and control the spontaneous formation of biologically-active hybrid materials for the development of new tailored applications in the field of sensing, nanomedicine and biochemistry.

1. Introduction

After the discoveries by Kroto *et al.* in 1985,[1] Iijima in 1991,[2] and Novoselov *et al.* in 2004,[3] the vast world of nanotechnology has drastically changed (Figure 1a-d). By discovering, isolating and characterizing fullerenes, carbon nanotubes (CNTs) and graphene, they revolted the field of carbon-based materials, in particular that of graphitic nanomaterials (GNMs) broadening their potential applications in a myriad of fields.[1–3]

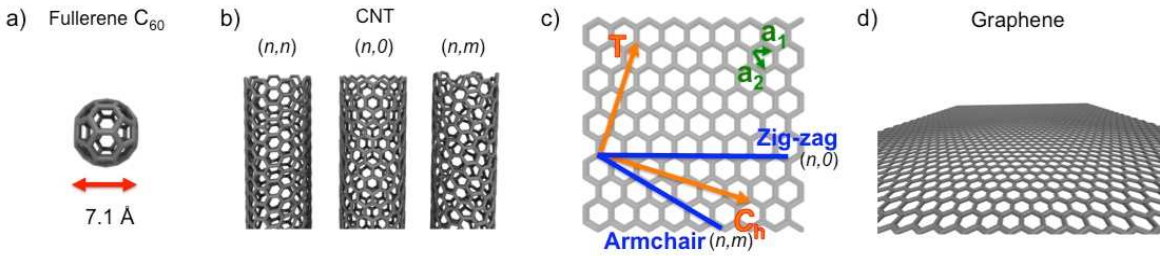

Figure 1. Structural representation of C_{60} (a), armchair, zig-zag and chiral single walled CNTs (with the (*n,m*) labelling based on the a_1 and a_2 vectors and the rolling vector C_h (c). Structural representation of graphene (d).

With its 7.1 Å wide cage (Figure 1a), C_{60} contains 12 pentagons and 20 hexagons that, fused in the football-like shape, conjugate all the double bonds within its geodesic structure.[4] The presence of both five and six-membered rings introduces more reactive sites for covalent derivatization,[5,6] in particular at the 6,6-junction, but it might also represent a specific anchor point for non-covalent interactions. For their part, CNTs are constituted by rolled graphitic sheets and can be considered as monodimensional nanostructures due to the high length/diameter ratio, *i.e* 10^4-10^5.[7] In fact, when a single layer of graphene sheet is rolled up to form a single-walled CNT (SWCNT), its diameter can range between 0.7 to 1.4 nm, while its length can go up to several micrometres.[8,9] On the other hand, when multiple graphene sheets are simultaneously rolled up concentric multi-walled CNTs (MWCNTs) characterized by a bigger diameter are obtained.[10] The modality in which the graphene sheet rolls and closes itself in a tube determines the CNT helicity (Figure 1c). The helicity is defined by a vector, named Chiral vector (C_h), labelled by a pair of integers (*n,m*) and by the two unit graphene vectors (a_1, a_2) as described by the equation $C_h = na_1 + ma_2$. Specifically, presuming an uncapped tube, when $n = m$ the hexagon orientation will display an armchair extremity in the resulting CNT, meanwhile when $m = 0$ a zig-zag termini is obtained for the resulting CNT; all the other cases lead to the formation of chiral CNTs (Figure 1b-c).[11] By

tuning the synthetic conditions,[12] one can produce CNTs with different chirality, diameters and length.

Finally, graphene is the planar, one atom-thick allotropic form of sp^2-hybridized conjugated[13] carbon atoms (Figure 1d). Akin to CNTs, graphene can also exist with armchair or zig-zag edges. It has been demonstrated that the edges manifest a different chemical reactivity than that of the side wall,[14] with the zig-zag topology showing a more pronounced chemical reactivity as compared to that of the armchair edges.[15] Additionally to the thermal, mechanical and electrical properties of the graphene sheets,[16] it is also worth mentioning the exposed double-sided surface, which can provide a versatile platform for double-sided functionalization.[14,17]

1.2 Methodological approaches towards structured materials

One of the recent and fascinating avenues to confer a new functional essence to GNMs through chemical modification is represented by the idea of merging nanotechnology and biology. By designing biomimetic nanomaterials, one could open great opportunities towards the use of graphitic structures in combination with biomolecules, *i.e.* peptide, proteins, or nucleic acids. By this way, the biomolecular modification would increase the poor solubility and low biocompatibility of these graphitic materials, leading to biohybrids exerting new functional properties exploitable for a large variety of applications ranging from imaging[18] and bio-sensing,[19–21] nanomedicine and cancer therapy,[22] gene therapy, drug delivery[23–25] and tissue engineering.[26] Aware of the concerns about the toxicological aspects of graphitic nanomaterials, the reader is redirected to other reviews that broadly tackle this topic.[27–31]

One of the main aspects to take into account when using GNMs, is their insolubility in aqueous and organic solvents. Regardless of their structural and geometrical dissimilarities, all the GNMs tend to form insoluble aggregates that stack in bundles. Therefore, by exploiting the knowledge in the chemical reactivity of the graphitic frameworks, substantial efforts have been carried out to modify their external surface in order to increase their solubility in organic solvents as well as in water,[32,33] thus implementing their practical manipulation and separation. Up to now, many reports support the successful functionalization of GNMs that can be achieved by a twofold approach: either by covalent functionalization taking advantage of the exohedral reactivity or surface defections, or by a non-covalent approach relying on weak interactions between the nanomaterial and the functional appendices.[32,34–39] The covalent functionalization implies the irreversible disruption of the conjugated aromatic network, thereby modifying the structural and

conductive properties of the nanomaterial. On the other hand, the non-covalent approach can be reversible preserving the structural and electronic properties of the GNMs.

Among the different biomolecular functionalizations (with proteins, enzymes, polysaccharides, lipids, DNA, RNA), the exponential interest in combining GNMs and proteins, as main exponents of biomolecular repertoire, requires a deep understanding of their way of interaction. In fact, the deep knowledge of the spontaneous tendency of GNMs to interact with proteins results of pivotal importance for the achievement of a controlled manipulation of these carbon nanostructures towards tailored applications.[26,40–42] The full understanding of the processes occurring at their interface is therefore the central key point to proficiently handle the two entities reaching smart hybrid ensembles or avoiding toxic consequences.

While examples, potentialities, prospects and challenges about hybrid carbon-based materials in nano-biotechnology have been extensively described in several recent reviews,[17,43–47] here we want to focus on the theoretical and experimental understanding of the main non-covalent interactions governing the interface between GNMs and proteins. Hence, in the present review, only the behaviour of non-functionalized GNMs will be considered to figure out the modalities and the main chemico-physical driving forces through which they spontaneously undergo association and bind biomolecules. The provided picture of the non-covalent interactions between pristine GNMs and proteins can serve both as reference to the exploitable aspects for engineering new materials for applications in the biomedical field as well as a guide to predict parasite adsorbing processes that would lead to toxicological effects.[28,42,48–50] Furthermore, this can represent the prologue of the comprehension of the more complex phenomenon of protein-corona formation occurring when nanomaterials are in contact with biological fluids. In this respect, the interested readers can refer to recent reviews tackling this topic into more details.[51–55]

Aimed at understanding in depth the forces ruling the adsorption of proteins onto GNMs surface, a systematic review of the experimental and theoretical studies carried out on non-covalent GNMs/proteinic biomolecules conjugates (fullerenes, CNTs and graphene) with amino acids (aa), polypeptide and proteins will be discerned separately in the following sections. This will provide an exhaustive picture at the molecular level of the specific driving forces governing the GNMs/proteins adsorption process. The reports dedicated to the covalent functionalization of the buckyball,[34,35,56–59] CNT[60–62] and graphene[41,63–65] and their biological applications[17,24,40,42,63,66–71] can be found elsewhere.

2. Fullerene hybrids

2.1 Fullerenes and amino acids

We start analyzing the behavior of C_{60} in complex with the 20 proteinogenic aa. For the sake of clarity, Figure 2 displays the structures and the nomenclature of the proteinogenic aa.

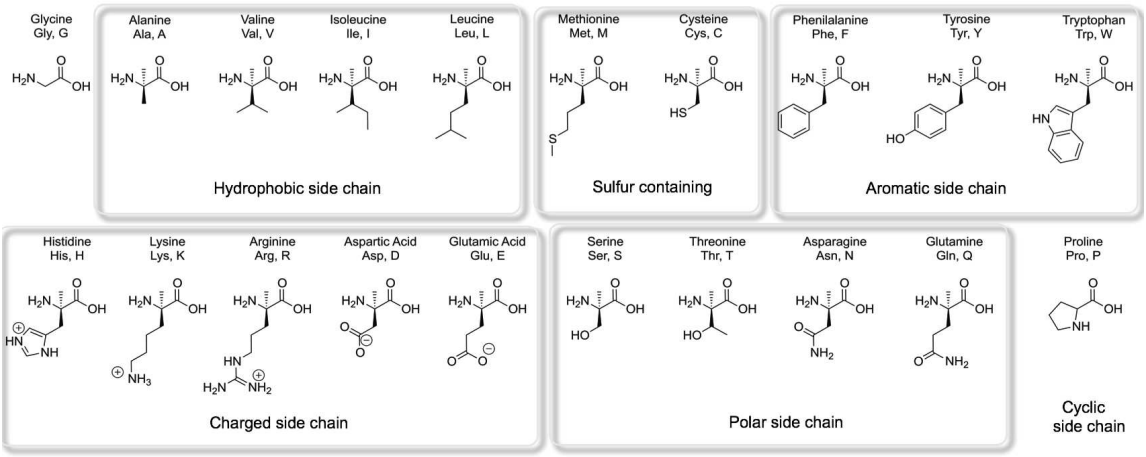

Figure 2. The structures of the 20 proteinogenic amino acids (aa) are reported and classified according to the nature of the side chains: hydrophobic, sulfur-containing, aromatic, charged, polar and cyclic. For each aa the common nomenclature, the full name, the three letters and the one-letter abbreviations are reported.

De Leon *et al.*[72] reported in 2008 a computational study on the interaction of C_{60} with the 20 proteinogenic aa performing density functional theory (DFT) calculations at the BLYP/DND (double-numerical plus diffusion basis set) level of theory *in vacuum*. The aa were classified according to the nature of their side chains and analyzed considering the interacting sites as well as the geometric and energetic properties. It results that all the 20 aa form favorable complexes with C_{60}, with the Leu, Arg, Trp and Glu units featuring the highest calculated binding energies (ΔE = -3.91, -3.36, -2.36 and -2.36 kcal mol^{-1} respectively). Despite the presence of different functional groups, the Leu, Arg, Trp and Glu units commonly feature hydrophobic alkyl chains that, thanks to their conformational flexibility, can embrace the spherical surface of C_{60} further stabilizing the complex (Figure 3). This has been further demonstrated when the adsorption of aa on C_{80} was modeled with the same computational approach,[73] demonstrating the formation of significantly stronger complexes compared to those formed with C_{60}. Notably, the sulfur-containing Met and Cys aa featured higher

interaction energies (ΔE = -12 and -11.45 kcal mol^{-1}, respectively). Beside van der Waals (vdW) and C-H···π interactions (α-CH···C_{80} distance of 2.07 and 2.91 Å), it appears that the low HOMO/LUMO gap of C_{80} favor sulfur-fullerene surface (S···π) interactions. Also, Lys, Tyr and Trp residues were found to form strong complexes, with the Trp term tangentially lying on the fullerene surface. Notably, the contact between each aa and the C_{80} cage is occurring through the amino acidic α-CH proton, rather than with the β□□□.

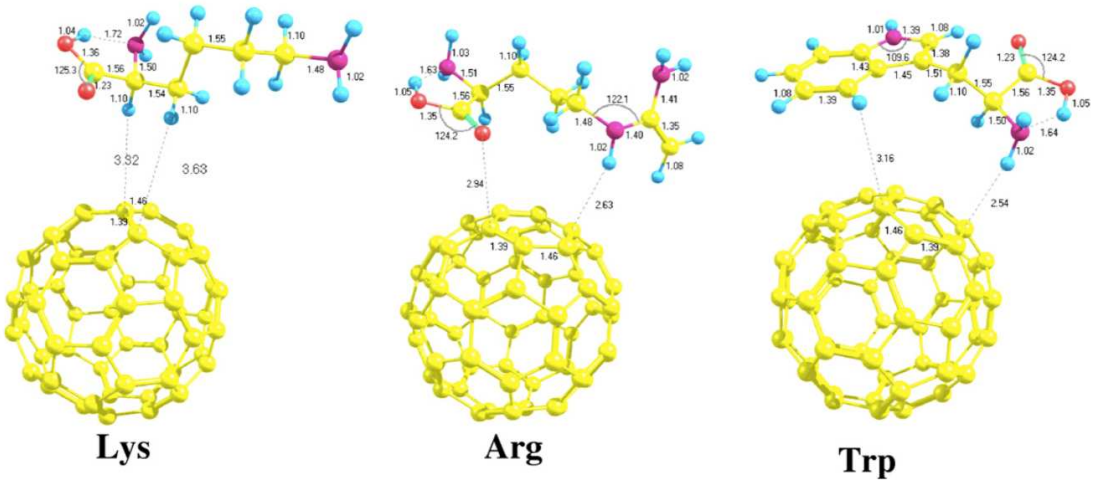

Figure 3. Optimized structure of the three most interacting aa with C_{60}. Also some geometrical parameters are reported, namely bond lengths (Å) and angle (°). Adapted with permission from ref. 72. Copyrights 2008, Elsevier.

In summary, by applying DFT methods to estimate the interaction of the 20 proteinogenic aa and different size fullerenes, the authors demonstrated a general stability of the complex formed with C_{60} mainly ruled by Lys and Arg residues that, bearing long alkyl chains, can establish shape-adaptable hydrophobic interactions.[72] At the same time, bigger the cage, lower is the fullerene HOMO/LUMO gap, thus favoring other types of interactions towards the formation of more stable complexes, in particular with aa bearing electron-donating moieties like Cys and Met.[73]

2.2 Fullerenes and polypeptides

As discussed above, the 20 proteinogenic aa can differently adsorb onto the fullerenes' surface, thus suggesting that the interaction between a fullerene molecule and

proteins' primary structure strongly depends on the polypeptide sequence. This can have significant repercussions on the proteins folding pattern, and thus on its functionality. For instance, it has been demonstrated that fullerene derivatives inhibit amyloid fibrillation through tightly binding the central hydrophobic motif (KLVFF) of the *β*-amyloid peptide (Aβ).[74] The strong hydrophobic-driven binding of C_{60} to Aβ prevents it from polymerizing and aggregating into the typical β-sheet secondary structure. Specifically, it has been found that pristine C_{60} inhibit Aβ polymerization with an impressive median inhibitory constant (IC_{50}) of 9 μM, 15-fold higher than the control experiments carried out on other known potent inhibitors described in the literature.[74] Following these evidences, Xie *et al.* proposed a molecular mechanism for the C_{60}-ihnibition Aβ□□□□□□□□□□□□□□ by reporting their 600 ns of replica exchange MD (REMD) simulations, whose reliability was further validated by AFM measurements.[75] They simulated the octamer of the Aβ□□□□□□□□f□□□□□□□, consisting of the hydrophobic motif KLVFFAE, alone or in the presence of C_{60}, a cluster of three C_{60} ($3C_{60}$) or C_{180} molecules and measured the structural and energetic parameters quantifying the inhibition effect on the fibrillation. It results that the inhibition effect was due to the ability of the cage to intercalate into the β-barrels[76] with a concentration-dependent trend. Notably, the presence of three C_{60} molecules causes a drastic reduction of the β-sheet content (from 44.5 to 25.7% for Aβ□□□□ Aβ□□$3C_{60}$, respectively), consistently higher than that induced by one C_{60} (45.2 %), as also appreciable by the structural representation of the most-populated clusters shown in Figure 4a-b.

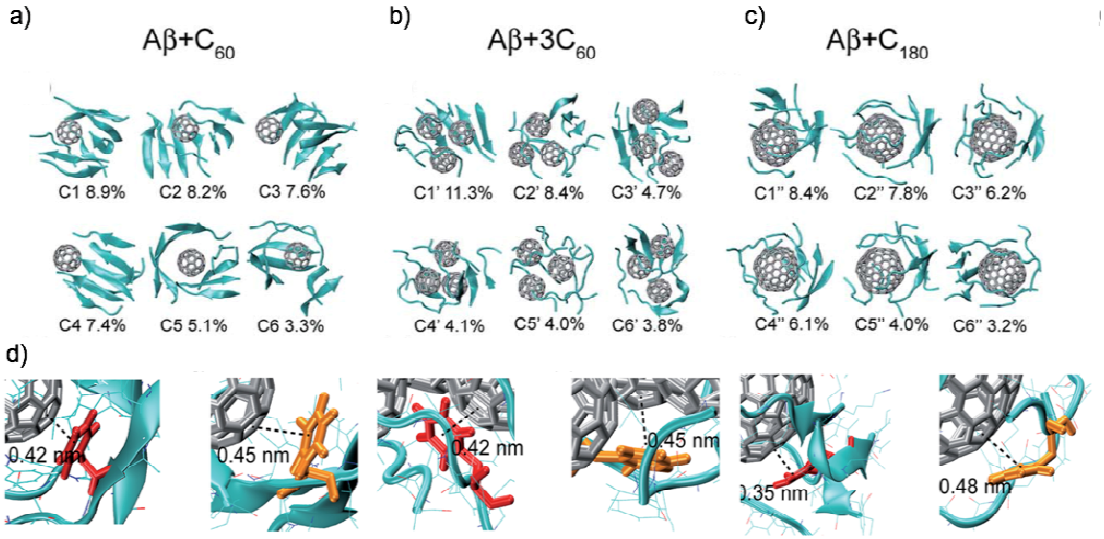

Figure 4. Representative structures of the top six most-populated clusters (C1-C6) and their percentage of occupancy for the systems Aβ□□C_{60} (a) Aβ□□$3C_{60}$ (b) Aβ□□$3C_{180}$ (c), the β-sheet secondary structure is denoted with the cyan arrows, random coils are represented otherwise. Analysis of aromatic stacking interactions (d), displaying in red the parallel-aligned hexagons-Phe interaction and in orange the pentagons-Phe, the distance between the centroids being also reported (d). Adapted with permission of ref. 75. Copyright 2014, Royal Society of Chemistry.

This was nicely confirmed by AFM images that show a strong diminution of the fibrils elongation and thickness upon increasing the C_{60} concentration (Figure 5). Whilst bearing the same number of atoms of $3C_{60}$ with a reduced surface area, C_{180} displays higher inhibition effect as detected by a lower β-sheet content (18.1%) and increased coils formation (Figure 4c). An in-depth analysis revealed that the inhibition effect was ascribed to the ability of the cages to compete for π-stacking interactions normally occurring between the aromatic side chains, the latters being responsible of the fibril compactness. In fact the aromatic Phe moieties are now engaged in π-π staking interactions with the hexagonal fullerenes' regions, thus losing the stabilizing effect on the fibrils.[75]

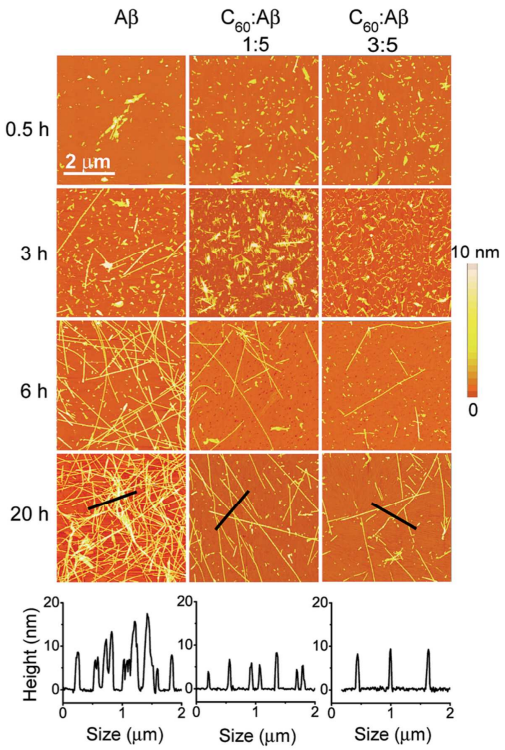

Figure 5. AFM images of Aβ, Aβ□C_{60} and Aβ□□$3C_{60}$ at four incubation times, and height analysis at 20h incubation time (bottom). Reprinted with permission of ref. 75. Copyright 2014, Royal Society of Chemistry.

Consistently, this hypothesis was in line with other simulations reported in the literature.[76] Noteworthy, the smaller curvature of C_{180} allows for closer parallel-aligned aromatic-stacking interactions (Figure 4d) as compared to C_{60} (0.35 and 0.42 nm, respectively), which corresponds to higher binding free energies (-217 *vs* -193 kcal mol^{-1}, respectively, estimated by using the Molecular Mechanics/Generalized Born Surface Area (MM/GBSA)). Conversely, for all the simulated systems the π-stacking interactions between aromatic aa and the pentagonal rings of the cages feature a staggered stacking at a distance of 0.45 nm (Figure 4d), demonstrating the preferential and predominant role of the fullerene carbon hexagons in these interactions. The active research on the inhibiting effect of fullerene on the amyloid formation denotes its importance as well as the potential role of GNMs in the field. For a comprehensive account, the interested reader is redirected to the topical reviews.[44,77]

Beside the chemical nature of aa sequence, high conformational freedom characterizes polypeptides before reaching the stable folded state. In this regard, the reader is addressed to section 5.2, where some comparative studies between the GNMs and different polypeptides are discussed.

2.3 Fullerenes and proteins

More than three decades ago with the pioneer work of Friedman *et al.* it was found out that the peculiar C_{60} structure presents the ideal and suitable size and shape for the formation of stable complexes with proteins.[78] They presented, aided by a molecular model and experimental binding essays, the surprising ability of a fullerene derivative to inhibit the HIV-1 protease.[78] The protein active site that, apart from the catalytic acidic residues, is characterized exclusively by hydrophobic aa, perfectly accommodates the fullerene derivative within its pocket consecrating an efficient antiviral activity of the modified nanomaterial.[40,59] Kinetic analysis characterized experimentally the binding revealing a competitive behavior with inhibition constant (K_i) of 5.3 μM,[79] and a dissociation constant (K_d) in the order approximately of 10^{-6}-10^{-9} M. The molecular model also validated the binding mode reporting the reduced solvent-exposed surface area before and after the binding thus showing that the 92% of the desolvated hydrophobic surface was due to C_{60} binding.

In line with the aforementioned work, in 1998, the group of Erlanger identified several anti-fullerene antibody (Ab), a subpopulation of which was also able to selectively discern C_{70} over C_{60}.[80] Aided by docking calculations, a combination of hydrophobicity matching, π-stacking and a combining site-fit between the Ab fragment antigen-binding region (Fab) and the geodesic structure was hypothesized to drive the mutual recognition. Two years later, the same group reported the crystal structure of the Fab of the first selective monoclonal Ab (mAb) against C_{60},[81] confirming the above-mentioned binding hypothesis. From one side, they managed to quantify experimentally a host-guest specific recognition with a binding affinity of 22 nM, while, due to the difficulties in co-crystalizing the Fab with the C_{60} cage, a molecular model of their complex complements the experimental evidences. It clearly showed that the nanomaterial, resembling the native Ab-antigen binding, establishes π-stacking interactions with aromatic aa (Trp, Tyr, Phe), while a weak OH···π interactions between the Tyr side chain and the fullerene surface was also observed (Figure 6a). Additionally, Asn and Gln are also found parallel to the curved cage, framing the nanomaterial in a perfect embrace within the mAb Fab as shown in Figure 6a.

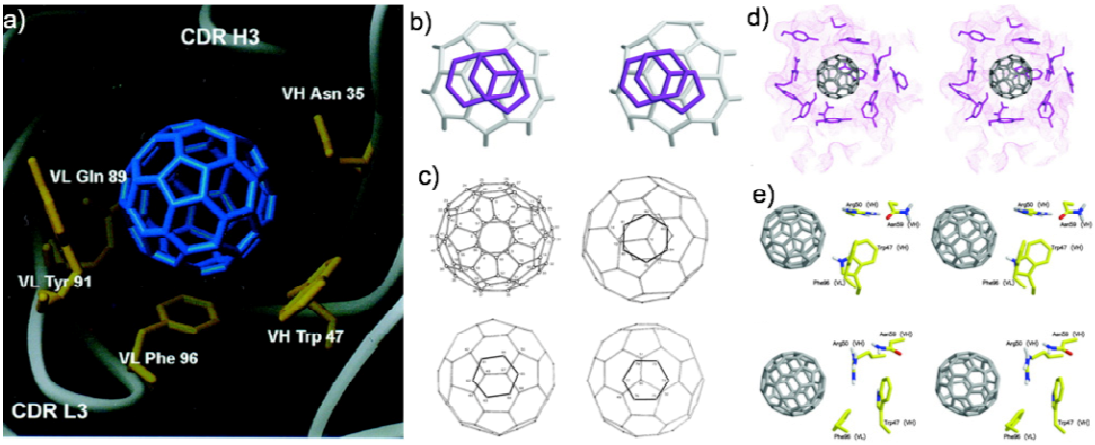

Figure 6. The model binding of C_{60}-Fab complex reported by Erlanger and co-workers shows the carbon cage in blue and the residues involved in the binding in yellow (a). Three π-stacking interactions involving an indole ring and two phenols are shown in (b), notably all stacks are localized at the 6,6-junctions as also observed in the crystal structure of C_{60} solvated by benzene (c).[82] The binding mode of C_{60}-Fab proposed by Noon *et al.* (d) and some snapshots of different interactions (e) (the main residues have been highlighted in yellow). Adapted with permission from refs. 81 and 83. Copyrights 2000 and 2002, National Academy of Science. Adapted with permission from ref. 82. Copyright 1969, Royal Society of Chemistry.

Similarly, Noon et al. displayed the net predominance of π-stacking of Phe, Tyr and Trp residues in the stabilization of C_{60}-Ab complex validated by 5 ns long MD simulations in explicit water.[83] Of particular interest is the triple π-stack surrounding the fullerene cage, the indole ring of Trp and the phenol group of a Tyr residue with a preferential localization over the 6,6-junction of the C_{60} (Figure 6b). The predicted displacement of the aromatic stacking was indeed consistent with the reported X-ray crystal structure of benzene-solvated C_{60} where the benzene ring is clearly located over the 6,6-junction of the carbon sphere (Figure 6c).[82] Along the dynamics of the C_{60}-Ab complex, CH···π interactions are also observed completing a general picture of dense network of π□electron rich connections (Figure 6d-e). The aforementioned cases were the first reporting the interesting ability of C_{60} to perfectly accommodate within a protein active sites (HIV-1 protease[78] and mAb[80,81,83]), to tightly bind it through □π-stacking interactions with aromatic aa (Trp, Tyr, Phe) and H···π contacts.

Afterwards, modulating effect of C_{60} on protein activity, in particular its antiviral inhibition, was thoroughly explored as the extensive theoretical and synthetic efforts give testimony.[59,67,84–88] Among others, many fullerene derivatives were prepared reporting their binding properties to several proteins, such as human and bovine serum albumin (HSA and BSA),[89,90] voltage-gated K^+ channel,[91] lysozyme,[92] glutathione S-transferase (GST)[93] and reductase (GSR),[94] and glutamate receptor.[95]

The targeting aptitude of C_{60} towards proteins was further investigated by Zerbetto and co-workers by docking calculations, quantifying the baiting protein tendency of a fullerene cage. In a remarkable work, they applied a reverse ligand-protein docking protocol, by which instead of testing the ability of a unique protein to bind several ligands they screened the tendency of the Protein Drug Target Database (PDTD), counting 1200 structures, to bind to a unique ligand, *i.e.* C_{60}.[96] This was aimed at identifying new potential C_{60} binding targets by validating the protocol with the available experimental data. The chosen docking algorithm includes additional binding scores that account for all the possible weak forces, namely the vdW interactions, partial electrostatics, explicit hydrogen and disulfide bonds contribution, π-stacking and cation-π interactions. This allowed for a thorough quantitative estimation of the interaction between C_{60} and the surface of all the available proteins in the database. The top 10% of the most binding proteins was selected and only a small percentage (20%) of the known fullerene binding proteins was discarded by the program as false negative, thereby validating the predictive power of the analysis.

Concerning the abovementioned proteins already known to experimentally interact with C_{60}, this protocol provides with important structural clues that give further explanation of the binding activity. At the same time, with this exhaustive docking procedure, they drafted a comprehensive list, equipped with structural information, of new binding proteins that might potentially interact with the carbon cage. For instance among the know proteins, they were able to identify the preferential binding site of C_{60} on GST and GSR, ascribing to a mixture of Ser, Phe, Asp, Ala, Tyr, Thr, Leu aa, located in the active site, the ability of C_{60} to bind and exert its inhibition activity. The previously reported noncompetitive activity of C_{60} derivatives on Acetylcholinesterase (AChE)[97] finds now an explanation in the preferential binding of fullerene to a hydrophobic cavity, other than the active site; the allosteric inhibition of cytochrome P450 by the carbon ball is unraveled by considering these docking results that find fullerene too bulky to fit in the active site; the binding to ATPase was now clarified by an allosteric behavior of fullerene that, overlooking the ATP binding pocket, finds a cavity that impedes protein rotational and conformational changes.

The first ranked protein was the voltage gated K^+ channel that, according to the docking algorithm, was plugged at the level of the chamber rather than at the entry region as previously postulated.[91] This is consistent with consecutive MD studies that identified a variety of binding sites within K^+ channel that C_{60}, passing through the hydrophilic mouth of the channel, occupies reaching an hydrophobic surface formed by an interhelical domain.[98]
To mention few among the unknown binding proteins, they show that the peculiar hydrophobic structure of the steroid hormones was nicely resembled by C_{60} when tightly binds different glucocorticoid and glucocorticoid-like receptors. The fullerene cage naturally competes for the steroids binding site that, rich in Trp, Phe and Tyr aa, easily lend itself for hydrophobic interactions. Furthermore, another binding pocket, particularly prone to hydrophobic interactions, was identified by fullerene on the Nitrile oxide synthase.

Hence, Zerbetto and co-worker shed light on the incredible affinity between a vast protein database and C_{60} and presented a peculiar and significant trend: the fullerene cage displays the outstanding ability of scanning a protein surface and identify the ideal pocket to accommodate and establish, through weak interactions, strong complexes.[96] The identified pockets, non-necessarily corresponding to the active site, have all in common aromatic, hydrophobic or charged residues that can entertain π-stacking and cation-π interactions. Among the 1200 proteins, the climb of the ranking, deciphered as the major or minor affinity to the C_{60}, is therefore achieved when the aforementioned interactions are maximized and the protein-fullerene surface complementarity leads to the perfect match.

Up to now it is hard to discourse about specificity and targeting, especially when the driving forces directing the association vdW and hydrophobic interactions that can come into play whenever aromatic or hydrophobic cavities can accommodate the C_{60}. But this is not all. The energetic gain derived from the solvophobic interactions, *i.e.* the desolvation free energy released by solubilizing the GNM with biomolecules, clearly plays a determinant role.[99] The latter is further maximized when a complete wrapping around the geodesic structure is achieved.[100] Therefore the appropriate size of the hosting cavity may represent the point of specificity in the binding activity with fullerenes.

In a following work, Zerbetto and co-worker applied the same reverse docking protocol on the PDTD to explore the possibility of accomplishing the selective and specific separation of different size cages (C_{60} and C_{70}).[101] By this way, they were able to classify the 1000 protein structures into 4 categories able to discern between C_{60} and C_{70} (p-C_{60} and p-C_{70}) via the same (homosaccic protein) or a different pocket (heterosaccic proteins). For instance Inosine-5-Monophosphate Dehydrogenase (IMPDH) results a p-C_{60} homosaccic protein, where C_{60} snuggles excellently in the binding site while C_{70} sterically clashes inside, lowering the resulting scoring function. On the other hand, the KcsA Potassium Channel is labelled here as p-C_{70} homosaccic protein due to the major number of contacts that the bigger cage can entertain within the channel pore, while the smaller fullerene is not able to fill completely the pocket (Figure 7).

From the exhaustive screenings performed by Zerbetto and co-workers, it was nicely confirmed that proteins easily accommodate fullerene cages within their hydrophobic clefts. Hydrophobic and aromatic aa play the main role in stabilizing the binding through π-π stacking interactions.[101] Furthermore, according to the nest's size, proteins are able to selectively bind the fullerene cage whose size satisfies the perfect protein-GNMs shape-complementarity. The highlighted relationship between volume fitting and binding capabilities of fullerenes interacting with proteins remind to the 55% rule, which states that the ideal binding can be expected when the ratio between the guest and the host volume is in the range of 55 ± 0.9 %.[102] The peculiar hydrophobic and vdW nature of binding that characterize fullerene-proteins interaction are indeed the ideal conditions in which the 55% rule holds, prompting that might efficiently describe this hybrid complexation.[103]

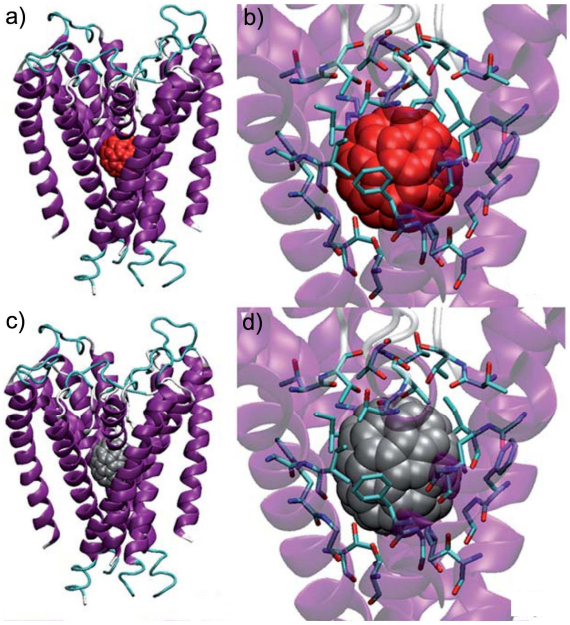

Figure 7. Docked complex of KcsA Potassium Channel and C_{60} (a-b) and C_{70} (c-d). Adapted from ref. 101 with permission. Copyright 2011 Royal Society of Chemistry.

Noteworthy, a very recent work by Calvaresi *et al.* showed the identification and characterization at the atomic level of details of the binding pocket where a 1:1 adduct between lysozyme and C_{60} is formed.[104] They were able to distinctively determine the adsorption of fullerene onto the protein surface by UV-Vis measurements, and the imperceptible variation in the circular dichroism (CD) plot demonstrates the structural stability of the protein upon binding. NMR chemical shift perturbation analysis in combination with docking calculations localize the fullerene in one of the six subsites of the endogenous ligand, with the direct involvement of two aromatic residues (Trp108 and Trp62, Figure 8a) and the catalytic aa (Glu35 and Asp52). The presence of the graphitic ball in this well-defined location was further demonstrated by the quenching of the fluorescent spectra of the Trp aa (Figure 8b). Notably, the identified binding site, pluri-validated experimentally and theoretically, is other than the one observed for CNT,[105] suggesting a controlled sorting process for different GNMs.

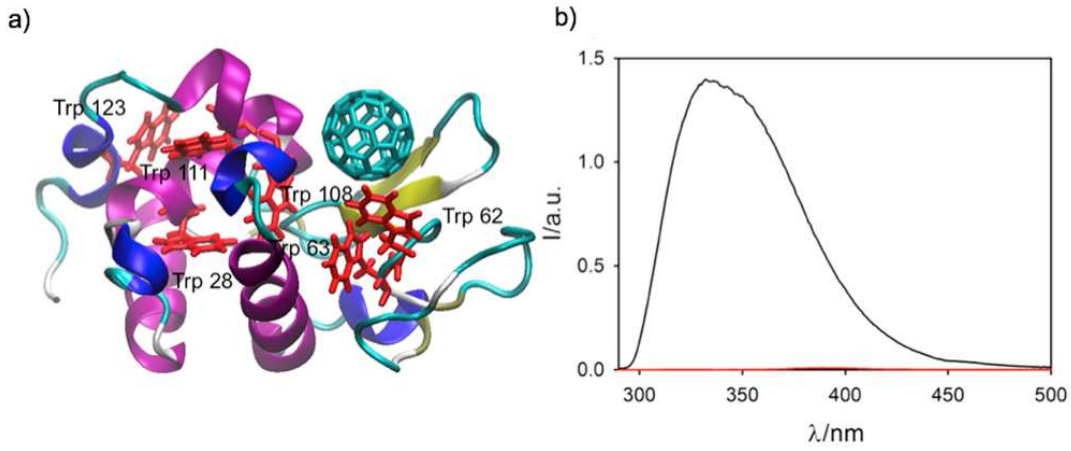

Figure 8. Trp residues are colored in red in the docked complex of lysozyme and C_{60} (a). The Steady-state fluorescence of monomeric lysozyme and C_{60}–lysozyme complex is plotted with black and red lines, respectively (b). Reprinted with permission from ref. 104. Copyright 2014, American Chemical Society.

3. CNT Hybrids

3.1 CNTs and amino acids

As observed for the fullerene-aa interaction in section 3.1, quantum mechanical (QM) calculations are particularly suitable for a detailed estimation of the nature and relative energy of the interaction ruling the adsorption between CNTs and aa. de Leon *et al.* extended the systematic study of the exohedral adsorption of the 20 proteinogenic aa[72,73] also on CNTs. In particular, the complex stability of the proteinogenic aa with both armchair (5,5)[106] and zig-zag (10,0) CNTs[107] treating the systems with the BLYP functional and the double-numerical plus diffusion (DND) basis set (nomenclature of the D-Mol^3 software that is comparable to the Gaussian 6-31G* basis set) has been evaluated. Their results were validated by comparison of Local Density Approximation (LDA) and gradient corrected DFT methods confirming the effectiveness of the chosen protocol. Surprisingly, the same stability order as that calculated for the fullerenes was also observed for the CNTs, with the Arg, Cys and Ala residues strongly interacting with the armchair CNTs (Figure 9), and the Arg, Cys, and Lys with the zig-zag CNTs.

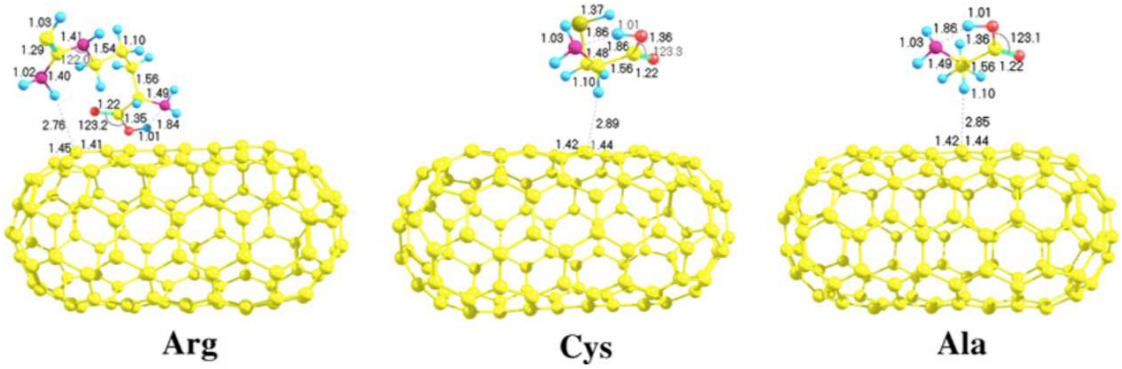

Figure 9. Optimized structure of the three most interacting aa with armchair CNTs. Also some structural parameters are reported, namely bond lengths (Å) and bond angle (°). Adapted with permission from ref. 106. Copyright 2008, Elsevier.

Interestingly, the positively charged Arg displayed the highest binding energies ΔE (-10.8 and -7.6 kcal mol^{-1} for armchair and zig-zag CNTs, respectively), this resulting from the hydrophobic interactions of the alkyl chain and the polar guanidinium group, whereas a specific thiol-CNT interaction is responsible of the notable stability of the Cys interaction with the graphitic surfaces (ΔE = -6.8 and -5.9 kcal mol^{-1} for armchair and zig-zag CNTs, respectively). Finally, Ala and Lys are noteworthy residues favoring hydrophobic association. Furthermore, they generally reported a lowered complex HOMO/LUMO gap that, together with the surface contacts, contribute to the aa/CNTs stability. It also emerged a major stability of the complexes formed with armchair CNT that the author ascribed to the enhanced density of state (DOS) near to the Fermi level of the metallic more than the semi-conductive case.[106]

Hence the authors described a significant influence of charged and sulfur-containing[108] aa in the interaction with both armchair and zig-zag CNTs. However, it is worth mentioning that important experimental evidences demonstrated that peptide sequences rich in Trp and His directly attach to the CNT surface showing strong adsorption, as it has been identified from a phage display analysis.[109] Indeed, the absence of the aromatic residues among the best-ranked aa in the works by de Leon *et al.*[106,107] is ascribable to the level of theory used (DFT/BLYP). Despite the fact that DFT calculations represent a good compromise in terms of computational time-accuracy, standard semilocal (gradient corrected) density functional approximations fail to describe the London dispersion energy,

thus being deficient in describing vdW and, more specifically, π-π stacking interactions. As a consequence the BLYP level of theory used to study the aa-CNT interaction did not describe properly the behavior of aromatic aa with different CNTs, as well as with different fullerenes mentioned above,[72,73] while was able to capture the significant contribution of positively charged and sulfur-containing aa thanks to the use of the polarized basis set.

By means of classical MD simulations, Az'hari *et al.* studied the adsorption of the 20 proteinogenic aa evaluating the SWCNTs' structural properties, like the chirality, length and diameter.[110] They performed 5 ns MD simulations in explicit water solvent modeling the proteinogenic aa on eighteen distinct CNTs, different in their chirality and length (chiral 4,1 and 5,2; zig-zag 5,0 and 7,0; armchair 3,3 and 4,4; each of them were simulated 2 and 4 nm in length) or chirality and diameter (chiral 8,2 and 10,5; zig-zag 10,0 and 14,0, armchair 5,5 and 8,8). According to their results, the aromatic aa were now found to have the largest interaction energies, with the aa displaying a tangential orientation with respect to the surface of CNT, which clearly accounts for π-π stacks. Following the ranking Trp, Tyr, Phe and His, these aa revealed to form the strongest complexes regardless the chirality, length and diameter of the tubular frameworks.[110] Among them, Trp and Tyr were particularly stable due to the presence of a bicyclic aromatic ring (*i.e.* indole) and an additional polar group (-OH), responsible of π-π stacking interactions and potential C□···π contribution. After aromatic aa, sulfur-containing, charged and polar residues bearing long alkyl chains were following. If the aa trend revealed to be constant, the chiral and zig-zag CNTs were yielding more stable complexes compared to armchairs tubes. This result was argued to be addressed to the major aromaticity of semi-conductive over the metallic CNTs.[111] Furthermore, increasing both length and diameter of the CNTs, the consequent increase in available surface induced an enhancement of the adsorption energies as well.

While it is well-established the effectiveness of the classical methods with fixed-charge force field to address electrostatic and hydrophobic interactions, less is certain when these kind of simulations are used to capture and efficiently reproduce π-π stacking contacts due to the lack of polarizability.[112,113] In a recent work, Yang *et al.* unraveled this issue by comparing QM calculations with three popular fixed-charge classical force fields (OPLS/AA, AMBER and CHARMM) contextually to the aa and CNTs interactions.[114] In order to verify the reliability in describing the π-π interactions of both QM and force field methods only the aromatic aa were considered in this study. Specifically, they have used density-functional tight-binding (DFTB) method with the inclusion of dispersion correction (DFTB-D), that

was previously benchmarked with other highly accurate QM methods (CCSD(T), QCISD(T), MP2) by performing calculations on small models (benzene dimer and indole/benzene complexes in different relative orientations) and comparing the relative energies of the different configurations. Then, the differences in the binding energy of Phe, Tyr, Trp in flat and edge conformation with respect to a CNT were calculated, also by minimizing the different adducts with different force fields *in vacuum*. This study showed that, the MM approaches with fixed-charge force fields may be incapable of predicting the exact binding structures as the structures of aromatic molecule-CNT complexes, obtained by the MM and QM predictions are slightly different. However, the relative energy differences among different conformations were predicted correctly so that standard force field appear to appropriately predict the strength of the π-π stacking interactions between aromatic molecules and CNTs. In fact, MM calculations well reproduce the energetic trend displaying the experimental-validated[115] order (Trp, Tyr and Phe). As expected, classical force fields were slightly overestimating the binding strength compared to QM calculations, but they can be considered as a valuable tool for studying the relative aa-protein/CNT interactions. The QM calculated induced charges and induction polarization energies of CNTs in the presence of the aromatic molecules are negligible. These findings exclude a polarization effect of these residues on the nanomaterial surface, nor the need to have a polarized force field to properly describe these interactions when the classical approach is chosen.

The same aromatic trend was also verified in the work of Lin and co-workers[116] that treated Trp, Tyr and Phe adsorbed onto both armchair and zig-zag CNTs at the DFTB-D level of theory *in the vacuum*. They additionally demonstrated that the π-π interactions are ruled by weak forces that do not affect the electronic profile of the CNTs, as the HOMO/LUMO shapes are identical in the presence and in the absence of the aa (Figure 10). The binding interactions of these residues generate tighter interaction when interfacing the zig-zag rather than the armchair CNTs, thus stating the preferential adsorption of aromatic aa on the semi-conductive CNT. Finally, the DOS profile of both CNTs results modified upon adsorption, in fact the presence of the aa induces the same shift in the Fermi level energy (from -4.6 eV to -4.4 eV) in armachair and zig-zag CNTs.

In short, when the interaction between single aa and CNTs is under investigation, one may rely on the binding rank according to the aromatic > sulfur-containing > charged > polar > hydrophobic aa adsorb onto the graphitic material.[106,107,110,114]

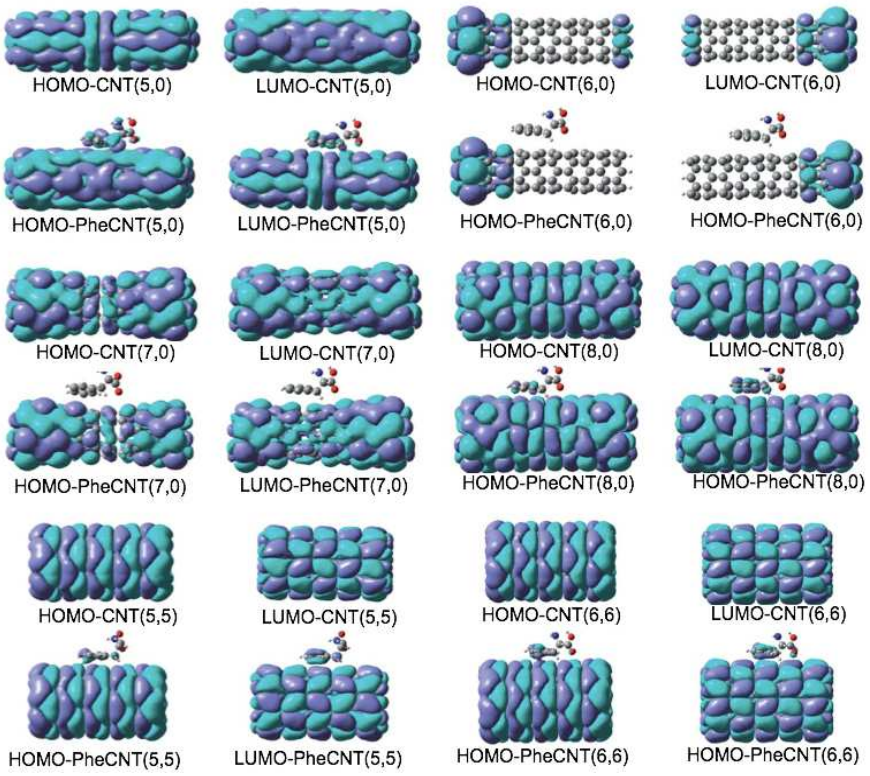

Figure 10. The highest occupied molecular orbitals (HOMOs) and lowest unoccupied molecular orbitals (LUMOs) of the different CNTs in the absence and in the presence of the Phe. Reprinted with permission of ref. 116. Copyright 2011, Royal Society of Chemistry.

3.2 CNTs and polypeptides

As observed in the previous sections, among the essential aa the strongest interacting residues with CNTs are those bearing aromatic appendages, whose peculiar tendency to non-covalently adhere on the CNTs surface through π-π□□□□□□□□□□ was also well-demonstrated experimentally.[109,115] In this respect, Zhang and co-workers carried out QM calculations (SCC-DFTB level of theory *in vacuum*) on complexes of NB1, B1 and B3 dodecapeptides with a SWCNT framework (Figure 11).[117] The different content of the aromatic aa in the three sequences clearly influences the binding properties on the graphitic surface. While NB1 peptide anchors the CNT's surface with the only aromatic residue (Tyr) giving rise to a low binding energy (E_B = -0.71 eV), B1 and B3 peptides, bearing 5 and 4 aromatic aa pieces, display stronger interaction energies (E_B = -2.85 and -2.22 eV, respectively). In fact, both peptides can adsorb onto the CNT framework wrapping their structures around the graphitic surface as favored by π-π and XH···π (where X = C and N) contacts. Furthermore, increasing the CNT diameter, an increasing binding energy was

observed as a major interacting surface is exposed to the peptide. The authors also investigated the CNT chirality reporting, according to their calculations, major interaction energy for the armchair CNTs in the complex with the B1 peptide.[117]

Hence, the natural tendency of polypeptide to adsorb onto CNT through aromatic aa, by establishing π-π and XH···π interactions, does not affect the conjugated π□□□□□□□□□□□□ properties of the nanomaterial as demonstrated by the exploration of the molecular orbitals and the DOS. As observed in above, CNTs face singularly the 20 aa (Figure 10),[116] also when interacting with a longer polypeptide its electronic profile in the presence and in the absence of the biomolecules is not perturbed (Figure 11), demonstrating that the governing forces are the weak stacking interactions. In confirmation of this, no charge transfer was detected.

Noteworthy, the aromatic interactions can be then exploited within designed structures to hierarchically control the CNT solubilization. At this regard, it is worth mentioning the example reported by Dieckmann *et al.* that shows the amphiphilic α-helix peptide nano-1 designed to solubilize CNTs and assemble in a macromolecular structure.[118] In fact, exploiting the amphiphilic nature of the designed nano-1, it was enabled the CNT solubilization through non-covalent interactions occurring at the nanomaterial interface with the hydrophobic (rich in Phe and Ala) side of the peptide, and the macromolecular assembly through inter-peptides interactions thanks to the hydrophilic (rich in Lys and Glu) one.

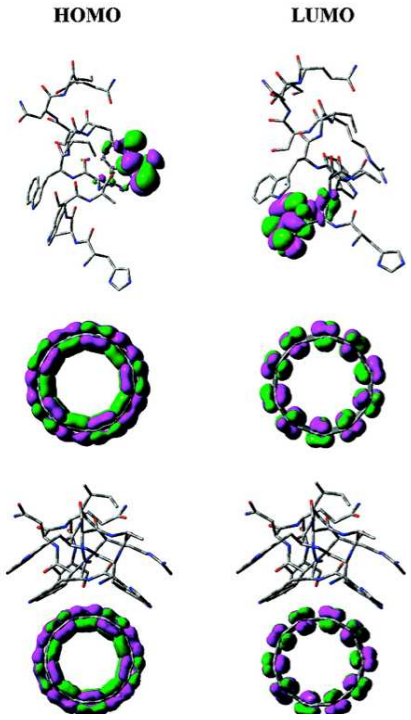

Figure 11. The highest occupied molecular orbitals (HOMOs) and lowest unoccupied molecular orbitals (LUMOs) of B3 peptide, (5,5) CNT and their complex. Adapted with permission from ref. 117. Copyright 2009, American Chemical Society.

Clearly, the secondary structure preservation results fundamental for the confinement of the functional sides that confer so the amphiphilic character to the designed peptide. Importantly, by performing CD measurements, it was demonstrated that the helical content of nano-1, increased in the presence of a CNT. Therefore, the nanomaterial assists the peptide folding in the designed amphiphilic helix, thereby exposing the hydrophobic face, prone to π-π stacking, towards the tubular surface. Increasing the concentration of the peptide up to the saturation point, the secondary structure content increases as well, further aided by the promoted inter-peptide contacts occurring between the lateral Lys and Glu residues. In order to allow the lateral electrostatic interactions, the peptides, once adsorbed onto CNT, align parallel to each other leading to a fiber-like organization as demonstrated by both polarized Raman measurements and transmission electron microscopy (TEM).[118] Additionally, the de-bundle process was thoroughly verified by several techniques such as scanning electron microscopy (SEM), atomic force microscopy (AFM) and UV-Vis measurements, observing the outstanding ability of the designed peptide to isolate a single CNT.[119] Notably, the AFM length and height analysis nicely shows the efficient dispersion

of CNT when in complex with nano-1 and, most importantly, the individual wrapped CNT by the helical peptide, as observed in the diameter distribution plot (Figure 12a).

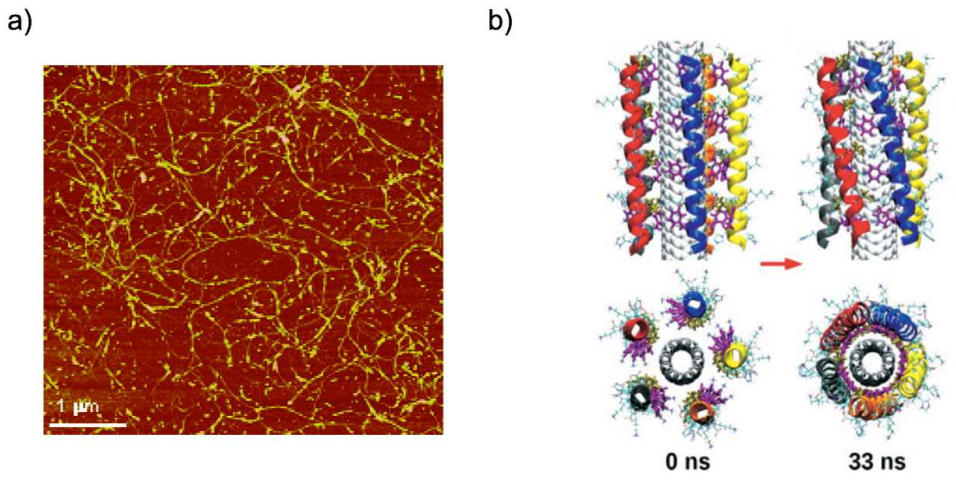

Figure 12. AFM image of nano1/CNT dispersion (a) and starting and last snapshot of the simulated adsorption of nano-1 pentamer onto a (6,6) CNT after 33 ns MD simulation (b) are reported. The views perpendicular (top) and parallel (bottom) to the CNT long axis are reported where the hydrophobic aa Phe and Val are colored in purple. Adapted with permission from refs. 121 and 123. Copyright 2004, American Chemical Society. Copyright 2009, Wiley Periodicals, Inc.

Indeed, the height measurements of the conjugate (~2 nm) match well with the diameter of the CNT (~1 nm) complemented with the peptide (1-3 nm) coating. Furthermore, the non-covalent interactions were characterized systematically varying the aromatic content within the nano-1 sequence, stating by this way the fundamental role of the Phe in anchoring the CNTs surface and ultimately disperse them through the π□stacking phenomena.[120] Additionally, extensive computational studies were carried out aiming at fully comprehend the non-covalent interactions involved at the nano-1/CNT as well as at the inter-peptides interfaces towards the formation of a hierarchized fibrillar organization.[121] Notably, by comparing the simulated adsorption process and the conformational changes of one single nano-1 approaching different hydrophobic surfaces (benzene, graphite and SWCNT), the nano-1 suitability towards the specific CNT solubilization was corroborated. In fact, the peptide fulfills its function only when adsorbed onto the tubular framework where, thanks to the CNT curvature, can properly anchor through the aromatic aa, expose the hydrophilic

faces and preserve the helical structure, lost otherwise.[122] Finally, the contribution of the lateral electrostatic inter-peptides H-bonds was demonstrated by MD simulations (30 ns long, explicit solvent) to be fundamental in strengthening the binding of nano-1 to CNT, to stabilize its secondary structure as well as the fibril formation around the nanomaterial.[123] Clearly, the adsorption onto the tubular network is driven first by the anchoring of the hydrophobic side of the peptide, then the fiber formation is settled by the lateral H-bonds between charged aa located at the hydrophilic sides (Figure 12b).

The masterful design of a helical peptide sequence to achieve the highly-order assembly around CNT was also reported by DeGrado and co-workers.[124] The designed surface-organized peptide functionalizes non-covalently the CNT surface through an Ala-rich side, while inter-helical interactions drive the assembly, and an external Cys represents the gold-binding site to ultimately induce the peptide-assisted gold assembly on CNT.

In general, it emerges a significant participation of hydrophobic and π-π stacking interactions when polypeptides interact with the curved surface of CNT. At this regards, the contribution and the importance of these aspects has been highlighted in the studies of the binding process between CNT and the monomeric amyloid Aβ peptide carried out by Jana *et al.*.[125,126] Performing extensive 100 ns long MD simulations in explicit water, the complete adsorption of Aβ peptide onto CNT was observed regardless the starting point, showing the main contacts at the level of the HP1 hydrophobic core of the peptide.[125] This domain is characterized by the peptide sequence $L_{17}VFFA_{21}$ where the aromatic Phe (F) in position 19 plays a determinant role. In fact, by simulating a single-point mutation with a non-aromatic but equally hydrophobic residue (Ile, I) or with an aromatic but less hydrophobic aa (Tyr, Y), different adsorption profiles were detected. The virtual mutation of the peptides is indeed reflected in their interaction propensity as not all the analyzed trajectories (four for each system) showed a full adsorption over the curved CNT. From one side, when the aromatic domain is substituted by the Ile, the π-π stacking cannot take place yielding a reduced interaction energy (4-simulations averaged interaction energy value of -10.5 ± 5.2 kcal mol^{-1}) as compared to the native peptide (-17 ± 2.6 kcal mol^{-1}) while adsorbing onto the CNT.[126] This suggests that the hydrophobic character of the HP1 still enables the adsorption on the nanomaterial, but, it is critically affected by the lack of π-π stacking interactions, owed to the absence of the aromatic component. On the other hand, the Tyr mutated peptide, even though able to establish strong interactions with the graphitic surface through π-π stacking, is weakened in the adsorption (-9.6 ± 9.5 kcal mol^{-1}), due to collateral solvent interactions,

that represent a barrier to the complete adsorption of the HP1 domain onto the tube. In this study the authors also performed free energy calculations, based on Adaptive Biasing Force method, showing that the presence of the CNT reduces the tendency of the peptide to collapse (with an energetic cost to avid collapse of 4 kcal mol^{-1} in the presence of CNT, with respect to 15 kcal mol^{-1} of the free peptide in solution).[125]

However, as stated in section 3.2, charged aa exert a remarkable tendency to adsorb also onto CNT mainly due to their peculiar surfactant-like structure where coexist hydrophobic and hydrophilic moieties. Based on this concept, recent experimental results demonstrate the remarkable ability of poly-L-arginine (PLA) peptide of efficiently bind and disperse CNT.[127] The authors used a tip sonicator to disperse SWCNT in the presence of PLA and poly-L-Lys (PLL) as reference polypeptide, reporting very different results between the two peptides. In fact, the adsorption spectra of different molecular weight polypeptides wrapped around the CNTs displays a smother profile when PLL is used (blue and green lines in Figure 13a) compared to the PLA (red and orange lines in Figure 13a), as a measure of the better CNT dispersion in Arg polypeptide. The dispersed nanomaterial was quantified by measuring the concentration of the supernatant after ultracentrifugation of the CNT in complex with different molecular weight polypeptides (5-, 10- and 20-mer labeled with R for PLA and K for PLL). The high concentration of CNTs in complex with the R rather than K oligomer reveals a significant solubilizing action of PLA over PLL.[127] The authors argued for the guanidinium group as main responsible of the efficient dispersion, addressing to its positive charges the ability of inducing electrostatic repulsions among the CNTs, thereby increasing their dispersibility. In fact, by playing with the pH up to acidic condition, the charged aa were deprotonated and the CNT aggregation occurred (Figure 13a). Furthermore, the authors availed themselves of steered (SMD) and classical MD simulations to clarify the way of interaction of the polypeptides understudy. 50 ns MD simulations in explicit solvent showed that both R15 and K15 adsorb onto the CNT sidewall wrapping around the graphitic framework (Figure 13b).

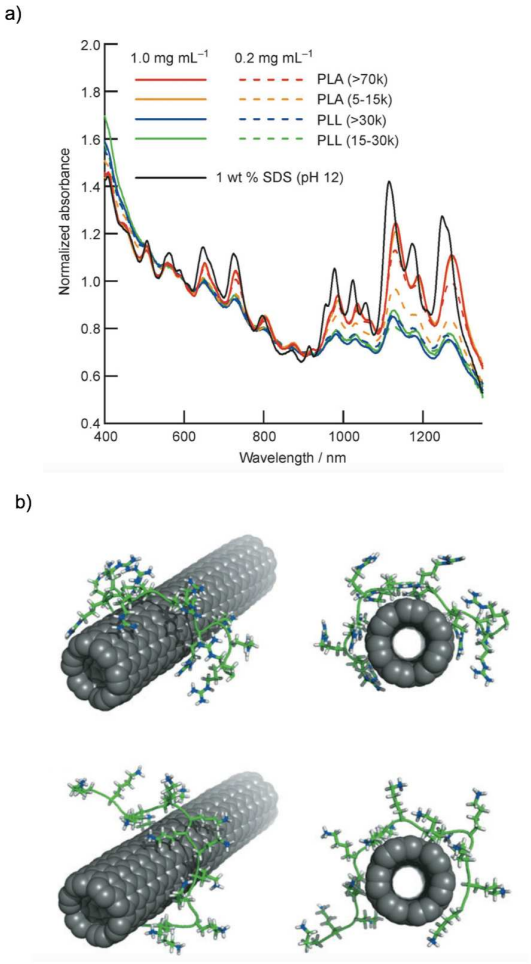

Figure 13. Adsorption spectra of SWCNTs dispersed by sodium dodecyl sulfate (black line), PLA > 70 k (red), PLA 5-15 k (yellow), PLL >30 k (blue) and PLL 15-30 k (green) are plotted (a). Significant snapshot of the MD simulation of PLA (b, top) and PLL (b, bottom) adsorbed onto the CNT sidewall. Adapted with permission from ref. 127. Copyright 2004, WILEY-VCH Verlag GmbH & Co. KGaA, Weinheim.

However, the radial distribution functions calculated between each atom of the side chain of the polypeptides and the CNT reveal that the PLA mainly interacts with the CNT surface through the guanidinium groups, while the PLL binds the nanomaterial through the backbone atoms pointing the charged moiety towards the solvent. This is then reflected in the force values estimated by the SMD when the unbinding process of the polypeptide was simulated: the force necessary to pull out PLA was double than that needed for PLL (200-225 pN and 100-125 pN, respectively), ultimately confirming the more efficient binding and thereof solubilizing effect of PLA over PLL.[127]

3.2 CNTs and proteins

In section 3.3, when the interaction between fullerenes and proteins was probed, it has been highlighted the incidence of the nature of aa within the exposed protein surface, size and shape variability in influencing the way of interfacing between the different biomolecules and the spherical GNM. On the other hand, when it comes into the evaluation of the non-covalent combination of complex and diversified proteins and CNT, also the variable size (length and diameter) of the latter has to be taken into account. In fact, SWCNT diameter can range between 0.7 and 1.4 nm, resembling at their tips approximately the fullerene size, while the length can reach even several microns. MWCNT, often used for experimental studies with biomolecules, can instead display several nm in diameter as well as in length. Reasonably, bigger CNT diameter corresponds to higher available surface and reduced degree of curvature of the external wall. As a matter of fact, none of these features can be underestimated in the study of the interaction of CNT and proteins.

If we start considering the small SWCNT size, several examples have been reported suggesting the actual insertion of the nanomaterial within hydrophobic pockets of proteins. For instance, the classical MD simulations in explicit solvent performed by Zuo *et al.*[128] show the snuggling of SWCNTs with different diameters (5.38, 6.73 and 8.08 Å) in the binding site of YAP65WW domain. This protein is characterized by a triple stranded β-sheet with a hydrophobic core that binds the natural ligand, the proline-rich motifs (PRMs) (Figure 14a). Several trajectories of 200 ns time scale were always converging towards the complementary shape fitting of the CNT within the hydrophobic pocket of WW protein, where Trp and Tyr were mainly found to stabilize the interaction (Figure 14b). These crucial residues normally stabilize the protein between the first and second β-sheet though the stacking between them. With the interaction of CNT, the distance between Trp and Tyr, denoting their π-stacking, increases in favor of the approach to the CNT.

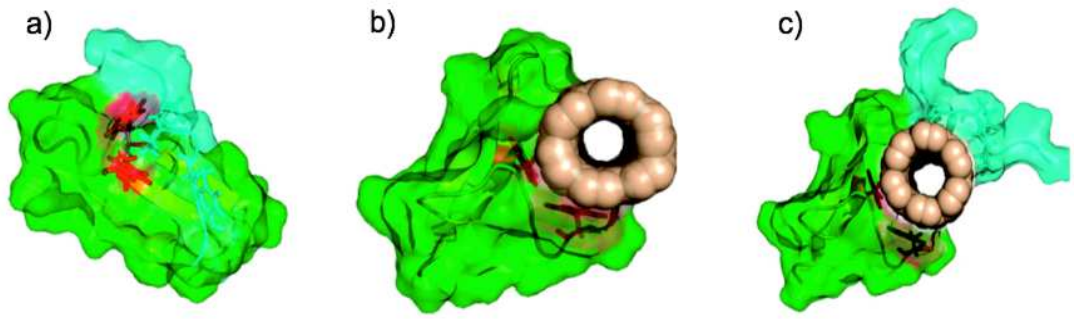

Figure 14. YAP64WW protein, in green, is represented in complex with the PRM in light green (a). Licorice representation of Tyr and Trp is highlighted in red. SWCNT is plugged into the WW protein (b). When CNT is bind to WW protein PRM is not able to bind anymore the active site (c). Adapted with permission from ref. 128. Copyright 2010, American Chemical Society.

Thus, the loss of the original contacts within the protein β-sheet and the formation of π-π stacking between the CNT and the aromatic aa cause the partial disruption of the active site that, occupied by the nanomaterial and thus unable to recognize the PRMs ligand, results altered in its functionality (Figure 14c). Similarly, the authors reported on the same plugging mode simulating the interaction between CNT and the SH3 domain, another PRMs-binding protein.[129] MD simulations show also in this case that the PRMs fails in binding the SH3 domain loosing the competition with CNT. This is confirmed by the major binding free energy (calculated from the average probability distribution function of the conformations spanned by the system during 10 200 ns long MD trajectories) obtained for the CNT compared to the endogenous ligand (-6.08 and -5.51 kcal mol^{-1}, respectively). As underlined above, aromatic aa, such as Trp and Tyr, and the cyclic Pro were found to stabilize the interaction of the CNT in the active site through hydrophobic interaction and π-stacking.

The CNT-protein shape complementarity driven by the interaction that a proteinic cavity can entertain with the hydrophobic nanomaterial surface directly remind to the ability of C_{60} to place in and tightly bind proteins. Notably, Sesti and co-workers demonstrated that C_{60} as well as SWCNT were suitable ion channel blockers thanks to their shape matching with the channel pore.[91] Very recently, a docking study performed by Turabekova *et al.* found that (5,5)CNT and C_{60} can stably bind to Toll-like receptors giving a plausible explanation of the cytokines and chemokines release induced by CNTs.[130] Additionally, the anti-fullerene antibody was demonstrated to similarly bind SWCNT by AFM measurements.[131]

However, these findings can be easily affected by a diameter dependent effect as we nicely demonstrated in recent works.[132,133] In this respect, we designed a magnetically-active hybrid material made of Fe-filled-MWCNT and the monoclonal Ab Cetuximab (Ctx), as targeting moiety for sorting cancer cells and magnetic fluid hyperthermia treatment.[132] Ctx activity refers to its selective recognition through the fragment antigen binding region (Fab) of EGFR receptor, overexpressed in several cancer cells. By performing in vitro magnetic filtration was demonstrated the selective separation of the model cancer cell from a population of healthy cells line operated by the covalent hybrid derivative. At the same time,

controlling experiments probed the cancer cells selective filtration, even though not quantitative, obtained with the physical hybrid mixture, assuming strong non-covalent interactions between the targeting moiety Ctx and the nanomaterial.[132] Remarkably, docking calculations showed that different Ctx conformations yield always the same interaction mode (Figure 15a), meanwhile increasing the CNT diameter (CNT30, 40, 60 and 80 Å) the outcomes converged to a unique orientation, where the CNT80 adsorbs preferentially on the fragment crystallizable (Fc), without hampering the two Fab regions (Figure 15b). This clearly states the diameter dependent effect adsorption process of Ab and CNT.

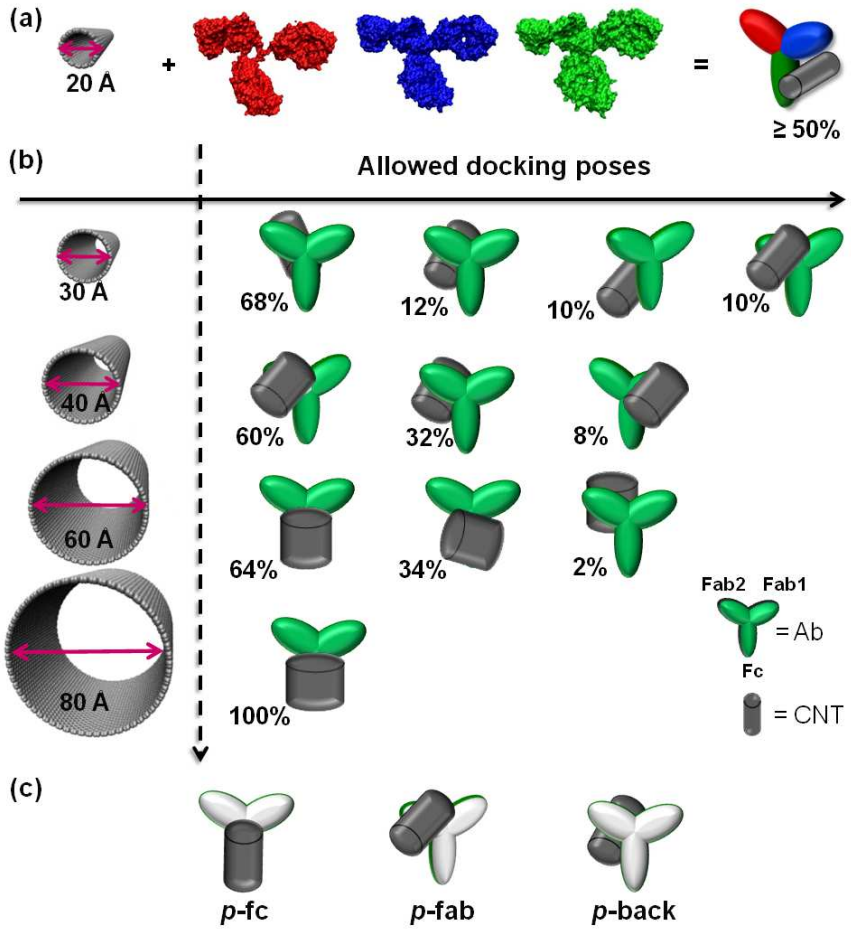

Figure 15. Adsorption orientation as calculated by docking simulations between CNT20 and the selected three most representative Ctx conformations (a). The most probable (≥ 50%) interaction mode is always the same for the three selected Ctx conformations. b) Systematic docking studies for different CNTs of increasing diameter values (30, 40, 60, and 80 Å labeled as CNT30, CNT40, CNT60, and CNT80, respectively). The predicted adsorption poses, sketched as cartoons in each row, are grouped into clusters from the most (left) to the lowest (right) populated one. c) The three different docking poses selected to perform the MD simulations are, from

the left to the right, *p*-fc (100%, as obtained from CNT80), *p*-fab (60%, as obtained from CNT40) and *p*-back (32%, as obtained from CNT40) the latter pose being recurrent also for CNT30 and CNT60. Reprinted with permission from ref. 132. Copyrights 2013 WILEY-VCH Verlag GmbH & Co. KGaA, Weinheim.

The dynamical properties of three main representative non-covalent adducts (Figure 15c) were investigated by 40 ns long MD simulations in aqueous solution and complemented by DFT calculations to investigate the physico-chemical origin of the main stabilizing interaction of the non-covalent adduct.[133] By reporting the unaffected secondary structure content it was highlighting the structural stability of Ctx upon adsorption onto the tubular framework, which exerts a stabilizing effect on the fluctuation of the antibody. The energetic analysis underlined the major vdW contribution in the stabilization of the complexes, that during the trajectories try to maximize the surface contact as clearly appreciable in the calculated variation of solvent accessible surface area (ΔSASA Figure 16a). The decreasing profile of ΔSASA point out the actual reduction of the exposed protein surface, instead occupied by the tubular framework.

Moreover, among the residues interplaying between Ctx and CNT, the most interacting were identified as the charged (Arg, Lys, and Glu) and polar (His and Thr) aa. Interestingly, the conformation of these residues over the CNT surface reveal a surfactant-like approach, where contact points are represented by the long alkyl chains these residues have in common, while the polar or charged moieties point towards the solvent (Figure 16b). The nature of this interaction was further characterized by DFT calculations (M06/6-31G*), which unambiguously attested the lack of polarization effects, confirming the pure hydrophobic nature of this binding. Notably, thanks to an accurate sequence and distribution analysis among other classes of Abs, the model of interaction between the biggest CNT and Ctx can be plausibly extended to all the antibody regardless their class of belonging.[133]

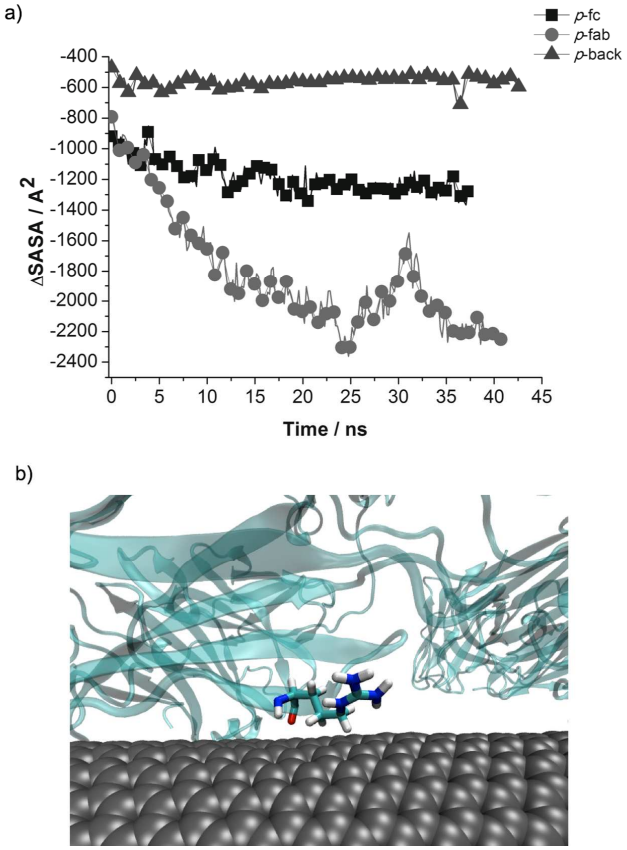

Figure 16. a) Calculated ΔSASA vs simulation time for *p*-fc (black square), *p*-fab (light grey sphere) and *p*-back (grey triangle) poses. b) Orientation of one of the most interacting residue, Arg, adsorbed onto the CNT surface. Adapted with permission from ref. 132. Copyrights 2013 WILEY-VCH Verlag GmbH & Co. KGaA, Weinheim.

The diameter-dependent behavior involved in the interaction of proteins and CNT was further analyzed by Regev and co-workers that, in a recent experimental study complemented by docking calculations, found the ability of a whey protein, the β-lactoglobulin, to solubilize CNT with two different diameter ranges.[134] They demonstrated that the solubilizing effect of milk is ascribable to its proteinic part and in particular to the β-lactoglobulin, that presents a narrow crevice (site A, Figure 17a-i/ii) where is able to accommodate CNT with a diameter < 4nm, while an external surface area (site B, Figure 17a-iii/iv) assist the solubilization of CNT with diameter > 40 nm. These outcomes were nicely verified by experimental, *i.e.* solubilization tests, UV-vis measurements (Figure 17b) and Cryo-TEM imaging, and in silico simulation, such as docking studies (Figure 17a). Both

site A and B are characterized by hydrophobic and positively charged aa, found to interact with the different diameter CNTs.

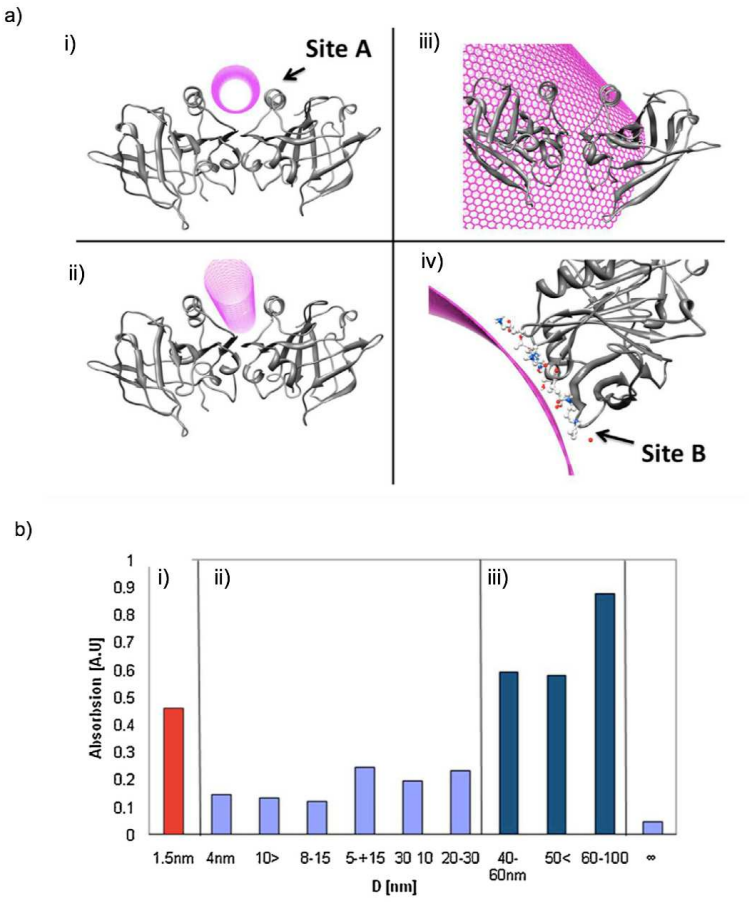

Figure 17. a) Docking models of the β-lactoglobulin interacting with a 1nm diameter CNT in the site A (i and ii) and with a 100 nm diameter CNT in the site B (iii and iv). b) UV-vis absorption of several diameters CNTs organized in zone i), ii) and iii) according to their dispersion efficiency. Adapted with permission from ref. 133. Copyright 2013, Elsevier.

As demonstrated above, the CNT insertion or the external surface adsorption onto proteins inevitably depends on the size and diameter of the GNM, while the orientation between the two strictly depends on the 3D structure and the amount of hydrophobic aa exposed by the interacting protein.[43] Concerning this aspect, a noteworthy confirmation came from the work of Ge *et al.* which described the different interaction processes between SWCNT and several blood proteins (fibrinogen BFG, immunoglobulin Ig, albumin BSA, transferrin Tf and ferritin) both experimentally and computationally.[135] Combining AFM and

CD techniques, the authors report a non-uniform adsorption of BFG and Ig with significant changes in the secondary structure profile that did not recover over the time (Figure 18); conversely, a uniform adsorption was described for Tf and BSA, whose changes in secondary structure were instead recovered over the time.

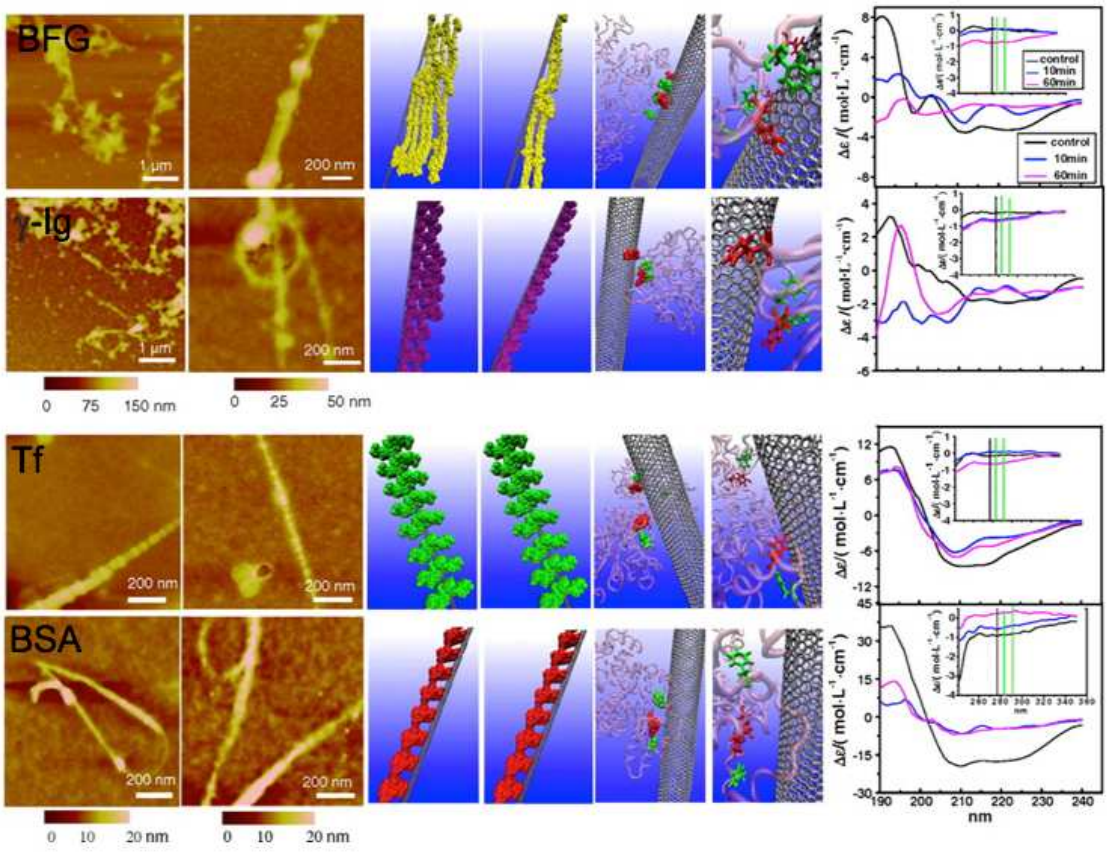

Figure 18. From left to right: AFM images of proteins in complex with SWCNT after 10 mins and 5h (first and second column, respectively). Molecular models of the proteins adsorbed onto the graphitic surface and the highlight of the Tyr (red) and Phe (green) aa. Far-UV CD spectra of proteins incubated with SWCNT. In the inset near-UV CD spectra are also reported. Adapted with permission from ref. 135. Copyrights 2011, National Academy of Science.

These experimental evidences were further elucidated by 150 ns long MD simulations in explicit solvent, shedding lights on the structural aspects of the proteins that influence the different adsorption profiles. In fact, by simulating the complexes formation and their dynamics, it was highlighted the crucial role of the aromatic Tyr, Phe and Trp aa interacting at the CNT/proteins interfaces. Interestingly, the interacting aromatic aa content,

the average contact residue number and the average contact surface area of the simulated systems lead to the rank BFG > Ig > Tf > BSA that is in perfect agreement with the experimental results.[135]

Further and more detailed studies on the interaction between CNT and BSA were reported, as a representative blood protein able to solubilize CNT.[136–138] BSA is α-helical multi-domains protein that folds in a globular tertiary structure including thereby a hydrophobic core at its interior. Both experimental and computational studies hypothesize a stepwise adsorption on CNT along which the secondary structure is conserved, but the globular information is lost exposing the hydrophobic core to the carbon surface.[136,137] The interaction was characterized at the atomistic level by MD simulations confirming the labile nature of the albumin tertiary structure upon adsorption onto the tubular network, in the attempt of exposing the hydrophobic aa. In fact, the orientations that yield a higher interaction energy bear more hydrophobic and aromatic components.[138]

Another well-know macromolecule used to disperse CNT in water, is Lysozyme (LYS) that along with the hydrophobic and π-π interactions, through which can irreversibly bound to CNT, presents a high content of basic residues that consents a pH-sensitive debundling process.[136,139,140] At this regard, the non-covalent interaction between LYS and CNT was skillfully investigated by MD simulations in a recent work by Calvaresi *et al.*.[105] Remarkably, the site in which the CNT preferentially adsorb is found far from the active site of the LYS, assuming the preservation of its functional activity. Furthermore, the secondary as the tertiary structure of the protein was not affected by the binding with the nanomaterial that lead to the formation of a stable hybrid complex. A more in depth analysis reveals that the formation of this complex was mainly driven by the presence of two helical structural motifs bearing Arg residues that act as tweezers in anchoring and solubilizing the CNT. This is in perfect agreement with the previously reported experimental works.[139,140]

In general, small SWCNTs have the suitable size to enter protein structures and nestle in their hydrophobic pockets. On the other hand, big CNTs fail in snuggling within the internal protein pockets but exert a remarkable tendency of interacting and non-covalently bind the external surface of proteins. The adsorption process is ruled by the shape and size of the protein surface and the amount of the exposed hydrophobic, aromatic and charged residues that are demonstrated to play a determinant role depending on the chosen protein.

4. Graphene hybrids

4.1 Graphene and amino acids

As far as aa and GNMs are concerned, their interaction might be influenced by the zwitterionic nature of the aa backbone. At the same time, the amino (N-) and carboxy (C-) *termini* might be capped with an acetyl and N-methyl groups, respectively, thereby resembling the typical peptide bond.

At this regard, in a recent work, Rubel and co-workers performed 40 ns long classical MD simulations modeling the system both in vacuum and in explicit water the 20 proteinogenic aa capped and uncapped, placed with their side chains parallel to graphene.[141] At first, comparing the graphene adsorption of capped and uncapped aa in vacuum, a higher adsorption energy of the former was observed compared to the latter (vertical lined *vs* parallel lined columns, respectively in Figure 19a). This behavior was ascribed to the larger number of atoms within the capped residues contributing to the adsorption energy as it is driven by vdW forces.

Afterwards, focusing on the capped aa, in order to assess the effect of the explicit treatment of water, vacuum/water simulations were compared. A drastic decrease in the adsorption energy of the water capped compared to vacuum capped aa was observed (right oblique *vs* vertical lined columns, respectively Figure 19b), suggesting a negative influence of water molecules in the aa binding onto the graphitic surface. In fact, aa/water interactions were now competing with the aa/graphene complexes, therefore weakening the final adsorption energy to graphene. However, from the adsorption energy plot of the water capped aa reported in Figure 19b, Arg > Trp > Tyr > His > Gln were identified as the most interacting residues. As observed for fullerenes and CNTs (see section 3.1 and 4.1, respectively), positively charged and aromatic aa represent the best residues for the interaction also with graphene, favored by their bigger side chains, as compared to the other aa, able to maximize the vdW contact, and by the aromatic moieties able to stack on the flat surface.[141]

Finally the authors distinguished between capped and uncapped aa in water, observing that the latters tend to desorb from the graphene surface, due to the better solvation of their zwitterionic state. For this reason, while a favorable interaction of water capped aa was detected (negative adsorption energies, right oblique lined columns, Figure 19c) lower or even positive energies were registered for water uncapped aa simulated onto graphene (left oblique lined columns, Figure 19c).

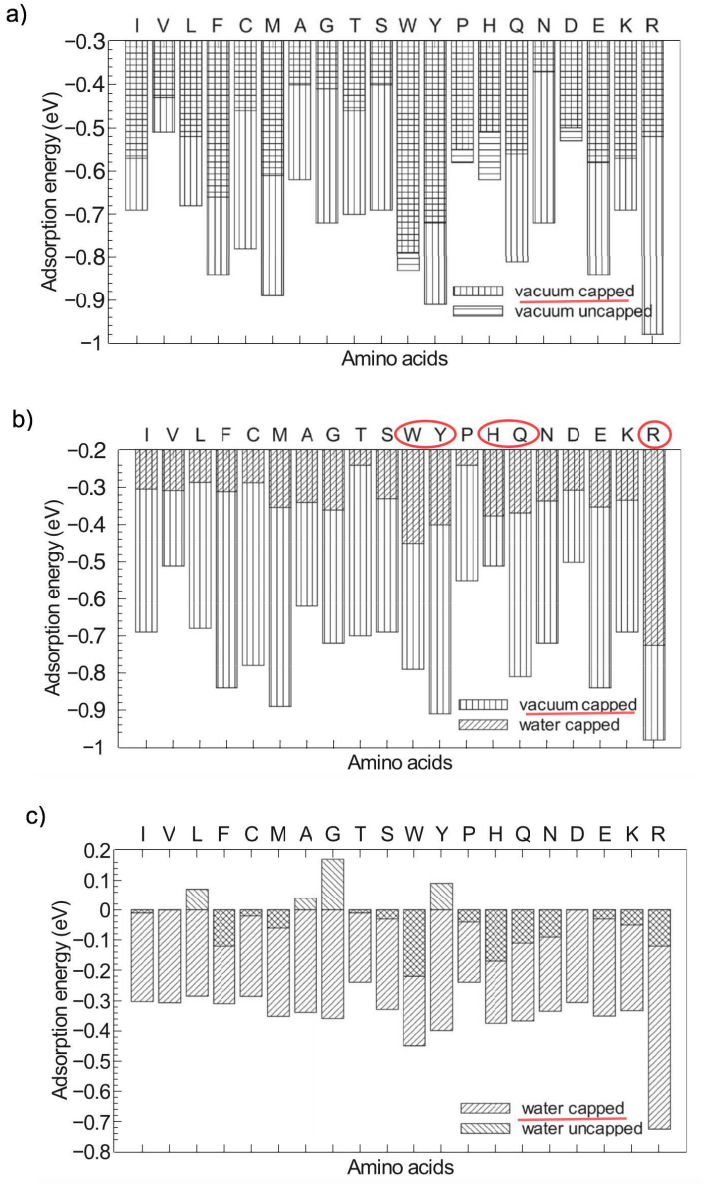

Figure 19. Adsorption energy onto graphene of vacuum capped and uncapped aa (a), of vacuum capped and water capped aa (b) and of water capped and uncapped aa (c). Red lines underline the most graphene interacting system within each simulated pair. Red circles highlight the most interacting water capped aa to graphene (b). The aa are labeled with the one letter abbreviation. Adapted with permission from ref. 141. Rights managed by AIP Publishing LLC.

Consistent results were also obtained by Pandey *et al.* that, by simulating the 20 proteinogenic capped aa adsorbed onto graphene by means of 40 ns long classical MD

simulations, found a similar trend of interaction (Trp > Tyr > Arg > Phe > His > Lys) both in vacuum and explicit water.[142]

In parallel, Camden *et al.* designed a Gly-X-Gly (GXG) tripeptide to quantify the single aa (X) contribution in the adsorption to graphene surface but inserted in a more realistic peptide chain model.[143] The binding energies were calculated from MD simulations in explicit solvent (15 ns long) according to the equation $BE = (E^{SURF+SOLN} + E^{WAT}) - (E^{SOLN} + E^{SURF+WAT})$, where E^{WAT} is the contribution of a water box, E^{SOLN} of a peptide solution, $E^{SURF+SOLN}$ of graphene and peptide, and $E^{SURF+WAT}$ of graphene alone. Furthermore, the contribution of the lateral Gly, modeled in the zwitterionic state, was estimated correlating the binding energy of G-$(G)_n$-G systems to graphene as a function of the chain length. This procedure allows the determination of the lateral Gly energy values, which were then subtracted to the total GXG energy values, obtaining thereby the individual X contribution to the graphene binding.

Among the 20 aa spontaneously adsorbed onto the graphitic surface (negative binding energy values), Arg (-17.5 kcal mol^{-1}), Gln (-15.9 kcal mol^{-1}), Asn (-15.3 kcal mol^{-1}) and Lys (-14.9 kcal mol^{-1}) are the most interacting residues. Analyzing the hydrophaty index of aa where positive (negative) numbers refer to hydrophobic (hydrophilic) side chains,[144] this well correlates to the trend described by the binding energies. As shown in Figure 20, Arg, the aa with highest binding energy (-17.5 kcal mol^{-1}), has the lowest hydropathy index (-4.5 kcal mol^{-1}), as also verified for the other most interacting polar aa (Gln, Asn and Lys). The linear correlation between the hydropathy index and the binding energy confirms the role of hydrophilic (charged and polar) aa in the adsorption to graphene.

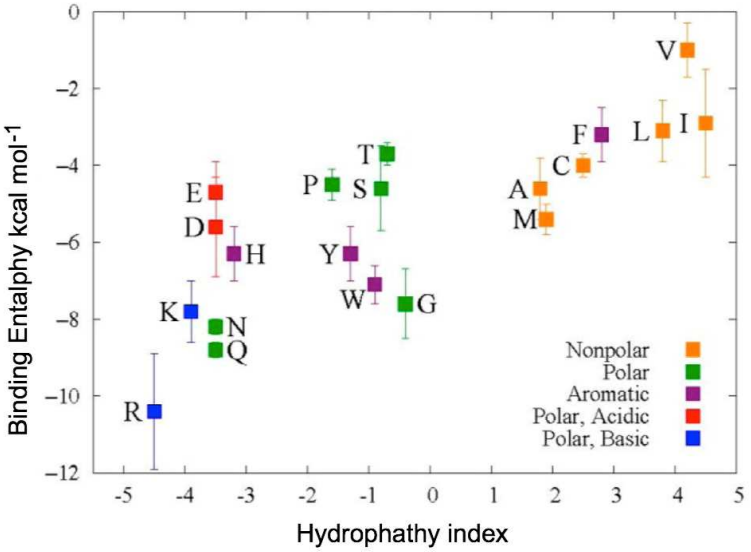

Figure 20. Binding energy of the interacting aa (labeled with the one letter abbreviation) plotted as a function of the hydropathy index. Adapted with permission from ref. 142. Copyright 2013, American Chemical Society.

In line with this, the highest binding energy of hydrophilic aa (blue, red and green residues in Figure 20), , is explained by the favorable coulombic interactions occurring with the negatively charged water oxygen found in the first water shell of waters interacting with the graphene surface. Negatively charged aa, such as Glu, similarly located in the first water shell, display instead a reduced binding energy (-11.8 kcal mol^{-1}) due to the repulsive interactions with these ordered waters.[143] In summary, the prominent role of positively charged aa involved in the interaction between aa, polypeptides, proteins and GNMs was widely explored both experimentally and theoretically, and was now found significant also in the adsorption on the 2D allotropic form of carbon.

This behavior was further verified when the interaction between a well-known bioactive tripeptide Arg-Gly-Asp (RGD) was simulated adsorbed onto the graphitic sheet.[145] DFT/PBE calculations (with DNP basis set) were used to characterize the RGD-graphene non-covalent binding where the zwitterionic form of the tripeptide was modeled on a 240 atoms graphitic surface. As shown in Figure 21a, different RGD conformations adsorbed onto the graphitic sheet were investigated among which the planar flat disposition yields the higher adsorption energy (Figure 21a-i/v).

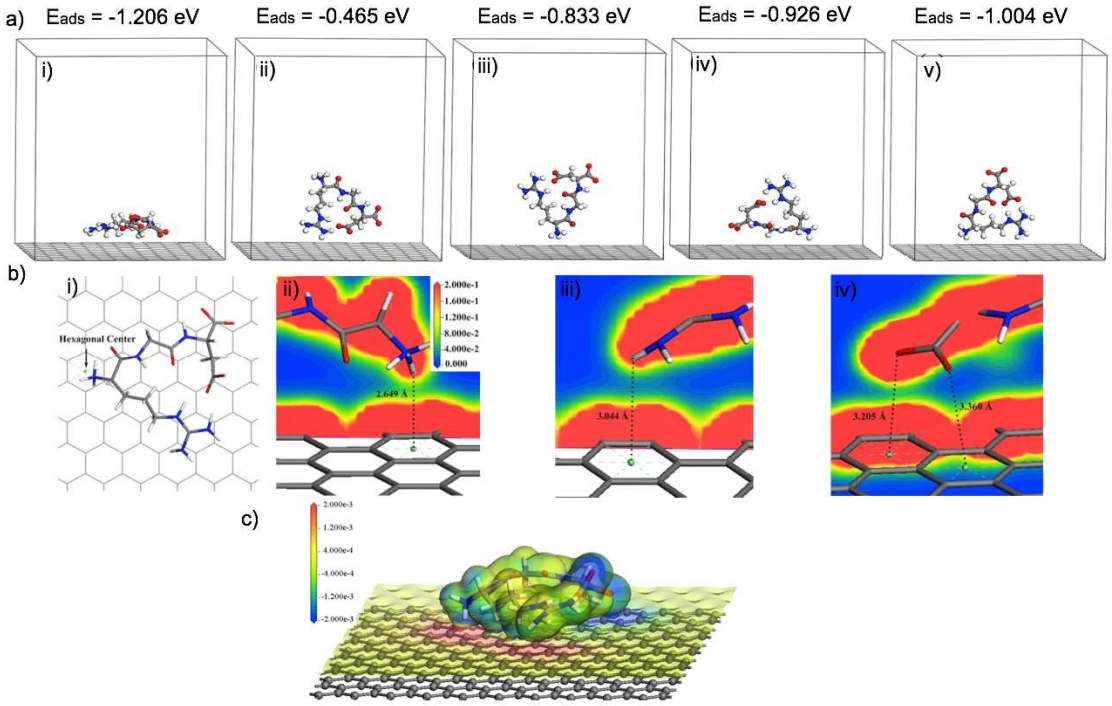

Figure 21. a) 5 configuration of RGD peptide on graphene (i-v). For each of them is reported the adsorption energy, E_{ads} (eV). b) Best ranked RGD conformation adsorbed onto graphene, whose hexagonal center is labeled (i). Electron density and geometrical distance between the functional groups, NH_3^+ (ii), the guanidinium-NH_2 (iii) and the COO^- (iv) and the graphitic hexagonal centers are highlighted. c) Charge accumulation (red) and depletion (blue) are highlighted in the electron density isosurface mapped with electron density difference of the RGD-graphene conformation. Adapted with permission from ref. 145. Copyright 2013, American Chemical Society.

An in depth visual inspection reveals that all the three functional groups within the RGD structure in the best ranked orientation are in contact with the graphitic surface pointing the NH_3^+, the guanidine-NH_2 and the COO^- towards the hexagonal center (Figure 21b-ii/iv). It is worth noting that a charge accumulation on graphene is observed in particular in the area of the amino and guanidine groups, while a charge depletion corresponds to the area of COO^- location (Figure 21c). The low intensity of the electron density is a clear clue of the weak non-covalent interactions coming into play in this binding geometry. This study further confirms the predominant role of positively charged or amino functional groups in the adsorption of aa onto graphene,[145] However, also in this case weak vdW interactions were not accounted by the computational approach employed.

In order to evaluate the solvent effect, the adsorption energy of the RGD/graphene systems with a small number of waters was also calculated. The water molecules result to

intercalate between the NH_3^+ and COO^- groups, inducing thereby a conformational change in the tripeptide structure that is now optimized in a more opened conformation. This allows for a better backbone adhesion onto graphene and for the attainment of higher energy value (-1.713 eV) compared to that in vacuum (-1.206 eV).[145]

Besides the interest in positively charged aa interacting with graphene, the spontaneous adsorption of the hydrophobic aa L-Leu, one of the most common and bioactive protein building block, was also investigated by a combination of DFT and MD calculations.[146] The aa, simulated in the non-ionic uncapped state at the LDA/DNP level of theory, was demonstrated to preferentially adsorb onto the graphene in a flat orientation (named G3-L) pointing the hydrophobic side along with the NH_2 group towards the surface (Figure 22a). The G3-L orientation yields a binding energy of -0.31 eV, which is in good agreement with the aforementioned cases (see Leu among uncapped aa in vacuum displayed in the Figure 19a and 21a).[141,145] The nature of this interaction was thoroughly characterized by analyzing the electronic profile of the HOMO/LUMO orbitals, the electronic density of state (DOS) and the electronic band of structures confirming allover the physisorption process occurring between Leu and graphene (Figure 22a).[146]

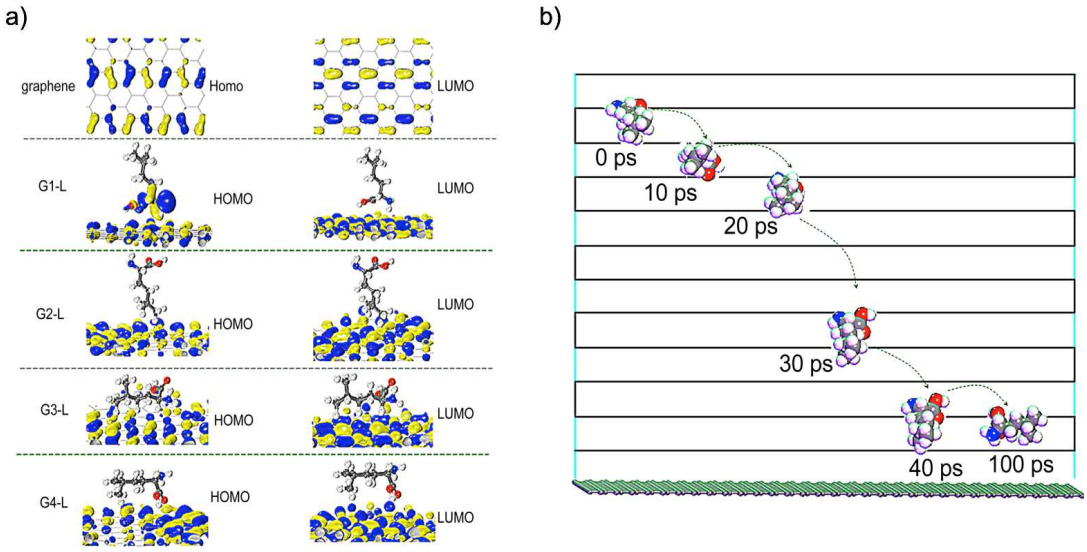

Figure 22. a) HOMO/LUMO mapping for graphene and the four Leu/graphene orientations understudy. b) Dynamic of the adsorption process of Leu onto graphene simulated by means of MD simulation in 100 ps time scale. Adapted with permission from ref. 146. Copyrights 2010, Elsevier.

Additionally, the dynamic aspects of the adsorption were described by the MD simulations in explicit water that, in agreement with the DFT calculations, predict a favorable and spontaneous adsorption within a short time scale (100 ps) with a parallel flat orientation (Figure 22b). A self-assembled parallel Leu organization was also observed when 100 molecules were simulated adsorbing onto the graphitic sheet as driven by intermolecular interactions between the uncapped NH_2 and the COOH moieties (Figure 23).

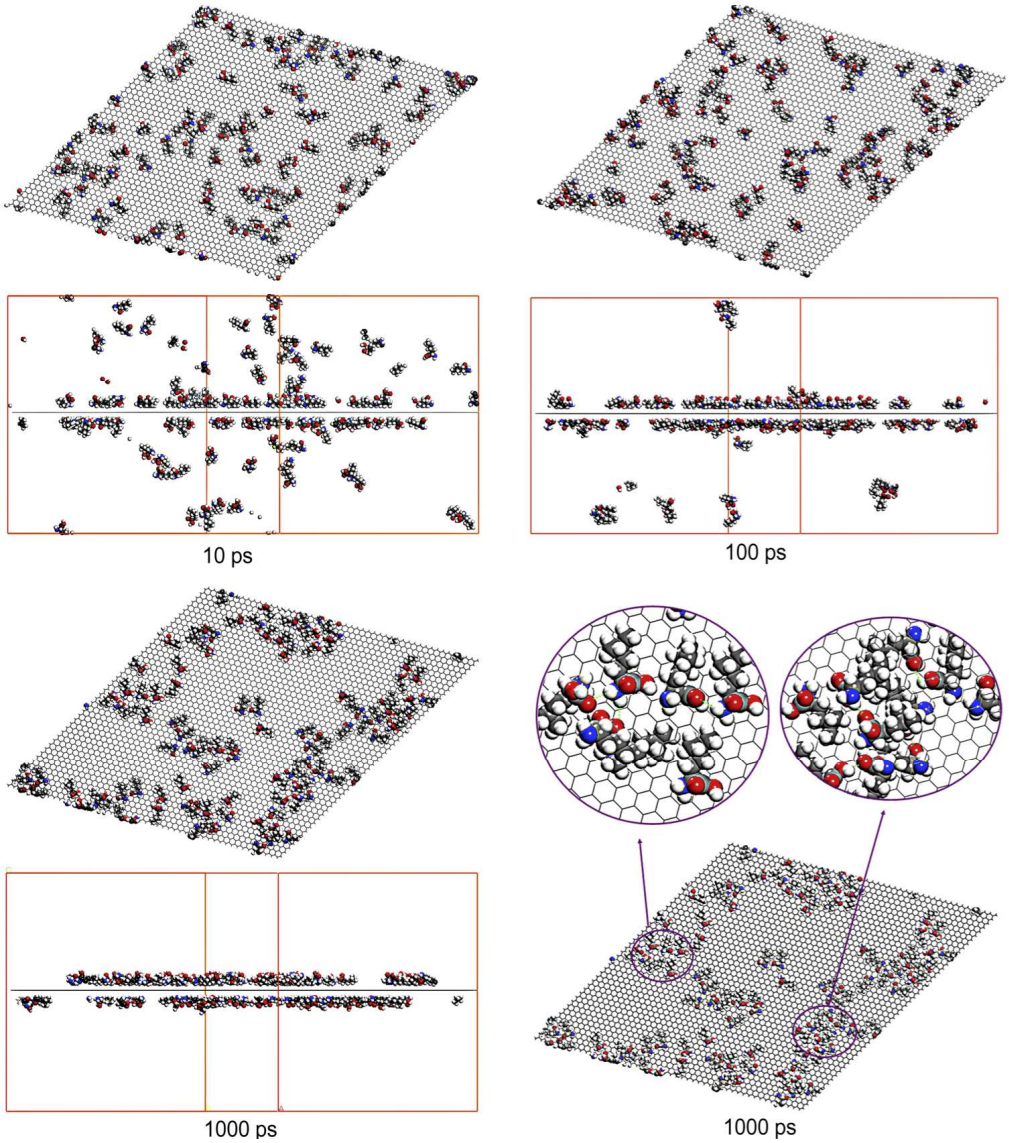

Figure 23. Top and side views of the adsorption process of 100 Leu molecules onto graphene, arranging in a parallel self-assembled organization (inset). Reprinted with permission from ref. 146. Copyrights 2010, Elsevier.

Consistently with the above study, the highly ordered organization of L-Met aa self-assembled onto graphene was proved by scanning tunnel microscopy (STM) and further corroborated by Molecular Mechanics (MM+ and AMBER force fields) calculations.[147–149] The sulfur-containing aa, deposited on the graphitic surface under ambient conditions, was able to achieve a low-coverage (40%) of the surface by organizing in regular rows spaced by a 45 Å gap and 18 Å in width, while a space of 8.6 Å was found between the individual Met molecules (Figure 24a-b).

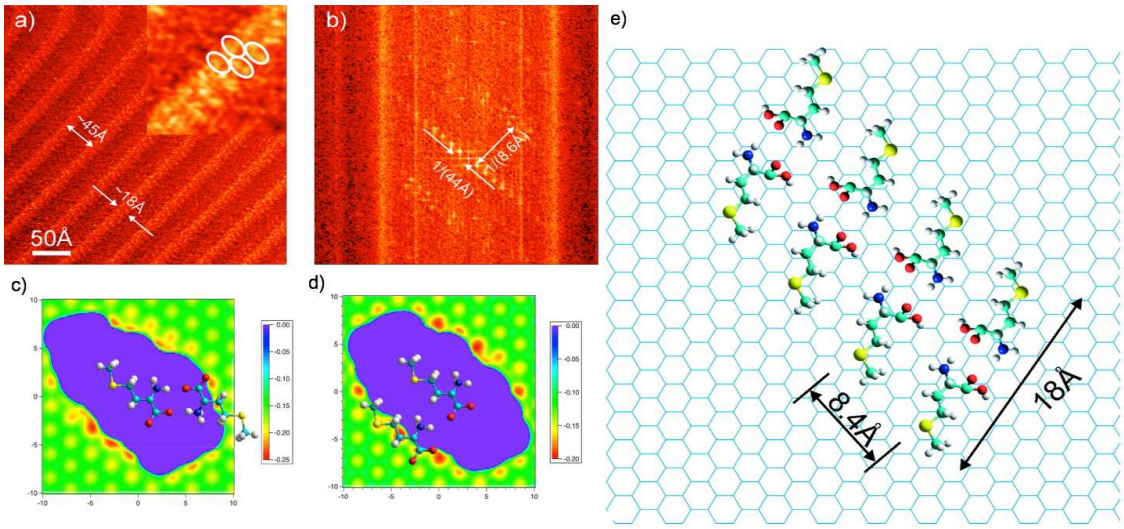

Figure 24. STM images show the low-coverage assembly of Met with the width rows of 18 Å (a), the spacing between the individual Met molecules of 8.6 Å and a row spacing of 45 Å (b). Antiparallel (c) and parallel (d) orientations of two Met molecules plotted over the potential energy. The proposed model for Met adsorption onto graphene surface (e). Adapted with permission from refs. 147 and 148. Copyrights 2009, American Chemical Society and 2010, Elsevier.

Theoretical studies complement the experimental evidences identifying the configurations behind the self-organized wires formation that well match the observed geometrical parameters. In fact, by simulating the orientation of a Met around another Met molecule taken fixed, it was mapped the total potential energy of the possible dimers. By looking at the energy level (lowest and higher energies are colored red and blue, respectively) was identified an antiparallel configuration of two Met molecules interacting through H-bonds between amino and carboxylic groups, the distance of which is in perfect agreement with the experimental ones (Figure 24c). On the other hand, a parallel

organization was also identified, well describing the intermolecular distance along the row (Figure 24d). As a general trend, aa tends to spontaneously adsorb onto the graphene flat platform and in order to maximize the surface contact a flat orientation of the proteinogenic building blocks is always preferred. Additionally, positively charged, aromatic and polar aa are demonstrated to non-covalently bind more tightly than the others 20 aa thanks to the right combination of molecular weight, vdW contribution and hydropathy index within their structure.

The importance of the aromatic participation in the non-covalent interactions of aa and GNMs results slightly surpassed by the positively or amino-containing residues when the adsorption involves individually protein building blocks and graphene. Nevertheless, as observed for CNTs in section 4.1, the choice of the level of approximation in modeling non-covalent interactions might be crucial to the reliability of the final results. At this respect, focusing exclusively on the interaction between aromatic aa and GNMs, Rajesh *et al.* compared the behavior of Trp, Tyr, Phe and His on the flat graphene and the rolled CNT, simulating the complex stability at the DFT/PBE and MP2/6-31G* level of theory in gas phase.[150] The optimized geometries of the selected aa onto the planar and tubular frameworks display a flat orientation of all of them on both the GNMs with similar, although smaller for CNT, interplanar distances found in the range of 3.3 to 3.50 Å (Figure 25). This clearly alludes to π□π interactions. Interestingly, the interaction energies of these systems were calculated depicting, for both the nanomaterials, the predicting classification Trp > Tyr > Phe > His, which perfectly correlate to their calculated polarizability α (362.65, 109.46, 76.35 and 66.71 a.u. respectively). However, it is worth noting that the aromatic aa interact more strongly with the planar graphitic platform rather than with the curved CNT, as the calculated interaction energies reveal (0.84/0.72 eV for Trp on graphene and CNT, respectively).

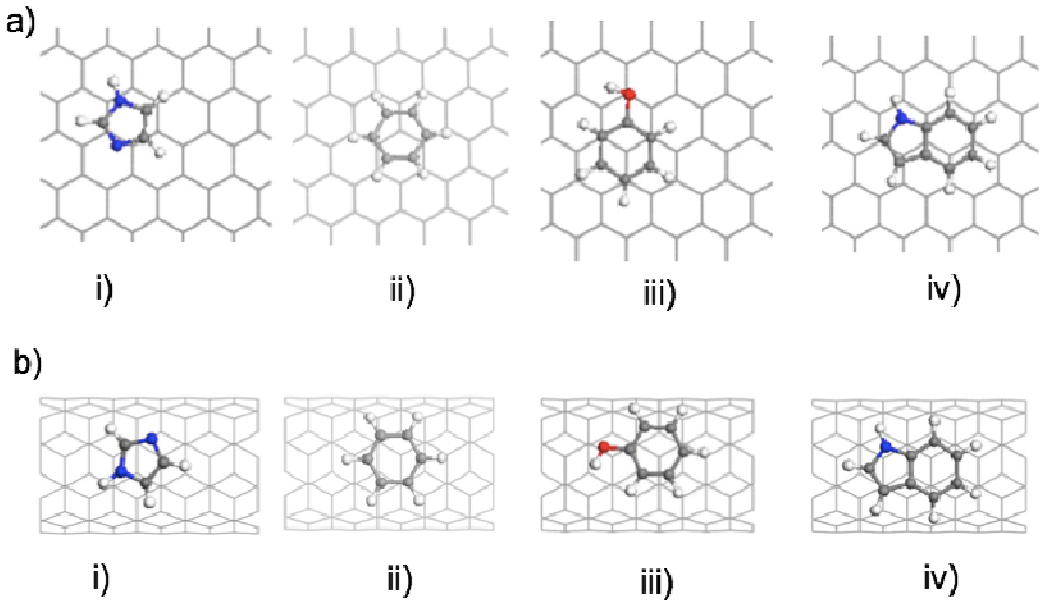

Figure 25. Optimized geometries of His (i), Phe (ii), Tyr (iii) and Trp (iv) on the flat surface of graphene (a) and on the curved CNT (b). Adapted with permission of ref. 150. Rights managed by AIP Publishing LLC.

It gathers that the planar geometry of graphene clearly enhances the π□ π stacking occurring between the aromatic rings and the surface generating smaller interplanar distances when the aromatic aa adsorb on it rather than on CNT. Consequently, higher interaction energies are observed for aromatic aa/graphene complexes demonstrating the stability of these residues on planar graphitic surfaces and the nature of this interaction evidently influenced by the curvature of the GNM.

4.2 Graphene and polypeptides

Thanks to their short length and the ease in their production, polypeptides are a versatile and suitable molecules for studying the interaction of peptide biomolecules with GNMs, such as graphene, to explore potentiality, driving forces and mutual effects involved in the combination of aminoacidic chains interfacing the flat graphitic sheet.[151] In particular, the combinatorial phage display libraries have been widely used to identify specific graphene-binding peptides, which were thereafter investigated adsorbed onto the graphitic surface in the view of designing new biomimetic hybrids.[152]

The structure of a dodecamer peptide, identified as graphene/graphite binding peptide (GBP) by phage display libraries, was thoroughly studied once adsorbed on these GNMs by

means of AFM, Raman, Fourier transform infrared (FTIR) spectroscopy and MD simulations.[153] The authors studied GBP structure first in its powder form by IR spectroscopy demonstrating the formation of an organized α-helical secondary structure (peaks at 1660 and 1530 cm^{-1}), lost when it is immersed in aqueous medium (peak at 1673 cm^{-1}). When deposited onto the graphitic surfaces, the same identical mesh-like adsorption was observed both in graphene and graphite, as proved by the AFM images (Figure 26a-c) and their height analysis (thickness of 0.99 ± 0.63 and 1.10 ± 0.45 for doped graphene and graphite, respectively). Peptide/nanomaterial FTIR spectra, resembling the spectrum of the powder form, clearly show the actual adsorption of GBP with a blue-shifted amide peak centered at 1670 cm^{-1}, as a sign of a different helical organization induced by the presence of the nanomaterial. Aiming at comprehend the structural differences described experimentally, the authors carried out MD simulations modeling the powder form of the GBP in vacuum, the solvated form in explicit water, and the non-covalent adduct adsorbed onto graphene.[153]

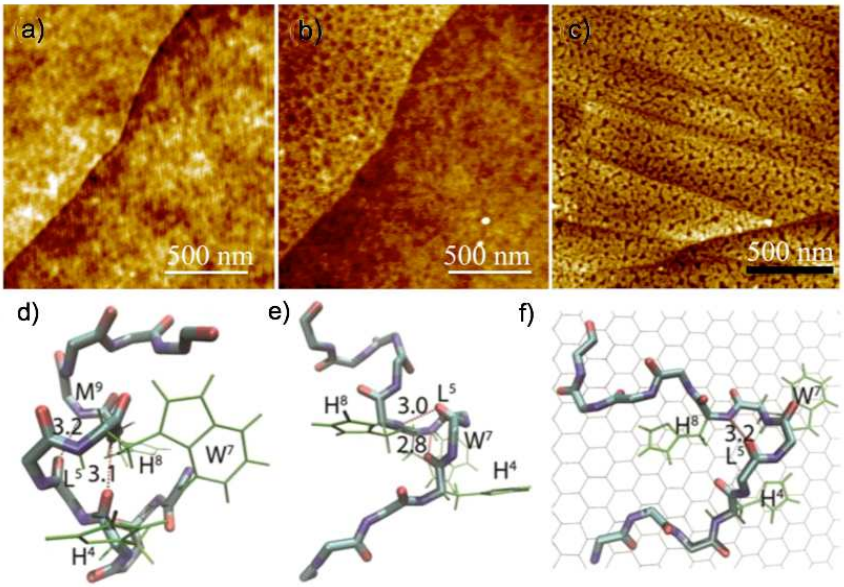

Figure 26. AFM images of graphene in the absence (a) and in the presence of GBP on its surface (b). GBP deposited on graphite (c) is also reported. The α-helical structure of GBP in vacuum is shown along with the intermolecular H-bonds (d), while a destabilized helix is found in water (e) and a fundamental aromatic anchoring of GBP is observed when adsorbed onto graphene (f). Adapted with permission from ref. 153. Copyrights 2012, American Chemical Society.

In good agreement with the experimental outcomes showed by the FTIR, the peptide in vacuum adopts the organized α-helical structure (Figure 26d), which is lost in solution

(Figure 26e) and differently reorganized once adsorbed on the nanomaterial (Figure 26f). Notably, the exposition of the aromatic Trp and His induce the structural reorganization that allows for the anchoring of peptide on the flat surface. Furthermore, their virtual mutation provokes a drastic reduction of the calculated interaction energies (126 ± 0.2 for GBP and 112 ± 0.2 kcal mol^{-1} for Ala-mutated peptide), confirming their fundamental role in the binding.[153] Clearly aromatic aa within the GBP play the determinant role for the favorable adsorption on graphene and graphite. However, edge-specific peptides were identified revealing other non-covalent interactions occurring at their interface. In fact, a phage display identified eptapeptide (P2) was found to bind preferentially to the edges of graphene surface and was compared to another plane-binding dodecapeptide (P1).[154] The peptides adsorption on graphene was monitored by AFM images that clearly show the lateral confinement of P2, even more evident when the latter was coated with gold nanoparticles (AuNPs) (Figure 27a and c). On the other hand, P1 was clearly localized on the central position of the graphitic sheet (Figure 27b).

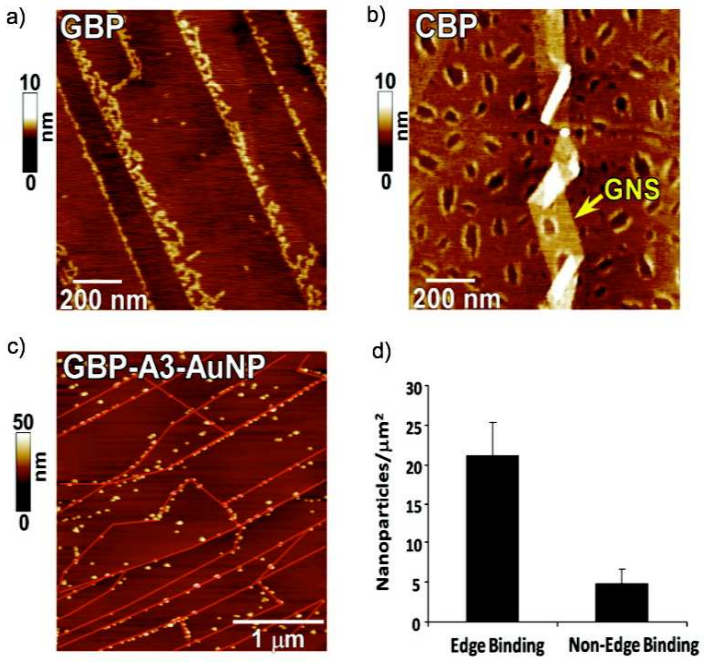

Figure 27. AFM images of P2 adsorbed onto graphene edges (a), P1 adsorbed onto graphene plane (b) and P2 coated with AuNPs adsorbed onto graphene edges (c). Bar plot of the number of AuNPs-coated P2 non-covalently bound to graphene edges or non-edges regions. Adapted with permission from ref. 154. Copyright 2011, American Chemical Society.

In order to fully comprehend the dynamics of the specific surface binding, 20 ns long MD simulations in explicit solvent demonstrated the border placement of P2 thanks to electrostatic interaction between Glu aa and the H-terminated edges, while the preferred central binding of P1 is ascribable to π□π stacking interactions occurring between the highly conjugated graphitic surface and the HYWYF aromatic motif. To further corroborate the electrostatic mechanism, P2 was simulated protonated as well as tested experimentally in acidic conditions, thereby exerting a different binding to the surface. Conversely, P1 behavior remained unaffected by the acidic conditions, unambiguously confirming the hypothesized nature of the interaction. This nicely show how the structural information encoded in the aminoacidic sequence can also influence the polypeptide behavior adsorbed on GNMs, introducing an element of control in the formation of tailored biomimetic surfaces. Clearly, the different aromatic content of P2, the chain length and the vdW contribution explain the graphene plane selectivity of P1. The presence of the aromatic anchoring motif induces a stronger binding as further demonstrated by coarse grained MD simulations.[142] The shorter P2 eptapeptide, lacking of the aromatic anchoring residues, results more flexible and finds its stability at the edges of the surface where can entertain non-covalent stabilizing interactions.

Moreover, a specific aminoacidic sequence can rule and guide the self-assembly of a short peptide onto graphitic surfaces achieving well-organized biostructures exploitable for technological purposes. Noteworthy example was reported by Sarikaya and co-workers, who studied by AFM microscopy the graphite induced self-assembly of another phage display identified dodecapeptide (GrBP).[155] GrBP sequence was characterized by three distinct chemical domains constituted of the hydrophobic domain I, the hydrophilic domain II and the aromatic domain III (Figure 28a). The observed uniform organization that this peptide is able to achieve adsorbed onto graphite was reached by a stepwise process that, monitored by systematic time lapse AFM images acquisition, reveals that the GrBP undergoes an initial binding, followed by an amorphous aggregation that unveils in an ordered phase (Figure 28b-c).

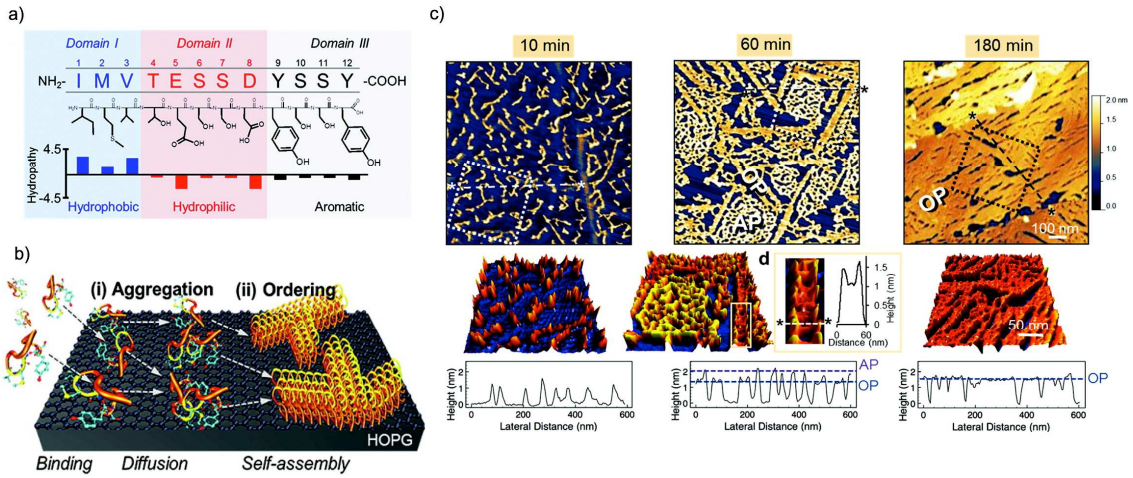

Figure 28. Chemical structure of GrBP characterized by hydrophobic domain I, hydrophilic domain II and aromatic domain III (a). Schematic representation of the stepwise adsorption and self-assembly of GrBP onto graphite (b). (c) Time-lapse AFM images of GrBP assembly after 10, 60 and 180 min of incubation. 3D and classical height analysis as a function of the phase formation. Adapted with permission from ref. 155. Copyrights 2012, American Chemical Society.

To understand in depth the adsorption and self-assembly process, rational mutations of the peptide chain enable the identification of the key residues governing the organization. Starting with the mutation of the aromatic domain (YSSY), the Tyr aa were replaced by an Ala in mutant 1 (M1), knocking out the aromatic contribution, which was then modulated when Tyr was instead substituted by a Trp and Phe in M2 and M3, respectively. M1 completely eliminated the binding capability of GrBP, first demonstrating the crucial role of the aromatic domain in the first phase of binding (Figure 29a). On the other hand, M2 displays a porous network formation assuming a correct binding, while cluster of reduced size were obtained with M3 probably due to the inefficient self-assembly. Additionally, the aggregation rate, dynamics of coverage and the calculated binding affinity reveal that GrBP attains the best self-assembled organization onto graphite over M2 and M3 (Figure 29a).

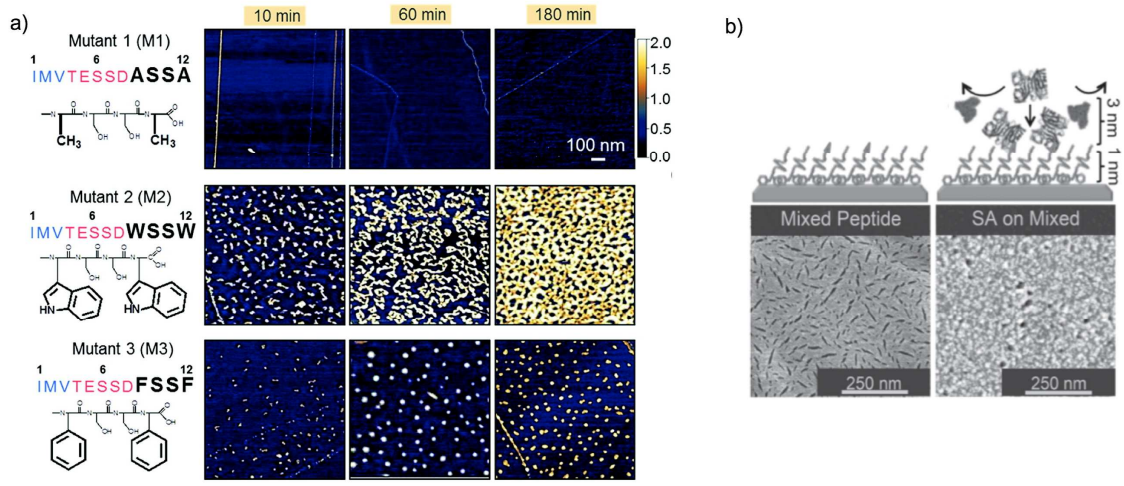

Figure 29. (a) Time lapse AFM images of mutant M1, M2 and M3. (b) Schematic representation of mixed self-assembled monolayer of GrBPs on graphene (top) and AFM images (bottom). On the right panel of image c) the self-assembled monolayer was tested for the detection of streptavidin in the presence of albumin buffer. Adapted with permission from refs. 155 and 156. Copyrights 2012, American Chemical Society and 2014, WILEY-VCH Verlag GmbH & Co. KGaA, Weinheim.

In a second avenue, when the hydrophobic domain was knocked out and replaced by hydrophilic residues, M4 results in a fully hydrophobic peptide that maintains its ability to bind graphite but it was unable to reach the high coverage and the correct folding. This meant that the amphiphilic character, gained by the combination of domain I and II, results crucial for the ordering onto the surface. As a countercheck, a similar amphiphilic mutant was tested (M5) unveiling comparable assembly on the graphitic surface.[155] Based on this concept, the authors designed an upgrade version of GrBP that, organized in dense ordered self-assembly onto graphene, can work as a biosensor exposing a molecular probe able to selectively target a specific protein (bio-GrBP).[156] Furthermore, by producing a mixed self-assembly of bio-GrBP and SS-GrBP mutant with proved anti-fouling properties, they were able to detect specifically streptavidin protein (SA) in a bovine serum albumin buffer (Figure 29b).

From the analysis sieved so far, it was found out that polypeptide structures can interact with GNMs, such as fullerene, CNTs and graphene trough hydrophobic or π-π stacking fashioned interactions occurring between aromatic, hydrophobic or positively charged aa and the different aromatic graphitic surfaces. Although the identified trend looks similar in the three cases, comparative studies have highlighted some differences in the dynamic behavior of the same polypeptide chain facing the different shapes characterizing

the GNMs understudy herein. As it has been clarified by the abovementioned examples, the aminoacidic sequence as well as the GNMs shape and size can reasonably influences the approach to each other. Moreover, the intrinsic conformational freedom that short proteins have before reaching a stable and favorable folded state deserves special attention in this context.

In 2003, in the pioneering work by Wang *et al.* CNTs selective polypeptide sequences were identified (B1-B4),[109] which arise the interest in investigating further their binding ability both on the tubular framework and on the flat graphene platform. A combination of docking studies and explicit solvent MD simulations (OPLS-AA force field) were carried out by Gianese *et al.*[157] aimed at investigating the adhesion process of the B3 phage display-identified polypeptide[109] on both CNT and graphene surfaces. The conformation of the free peptide in water solution reveals a folded state (obtained by 10 ns MD simulations) stabilized by intramolecular H-bonds with a free energy gain of 3.32 kcal mol^{-1} with respect to the unfolded state. B3 was then docked onto both the graphitic surfaces individualizing the best-scored complexes, subsequently characterized by MD simulations (6 ns long). While interacting with the CNT, B3 is shown to readapt its conformation according to the geometry of the tubular framework. Notably, a considerable increase of the contact area with the nanomaterial is observed as compared to the starting point (from 298.7 to 433.2 $Å^2$) corresponding in parallel to an increase of the free energy of binding (from -8.41 to -9.02 kcal mol^{-1}). Free energies of folding and binding were calculated considering the variation of solvation free energies. The stabilization of the complex is accompanied by a further increase of the number of intramolecular H-bonds (from 6 to 11) which, enhancing the structure stability, improves the binding affinity as well. Interestingly, His and Trp were found the most interacting residues from the calculated free energy, even though resulted from a visual inspection non-parallel to the surface. The interaction of B3 and the CNT was clearly characterized by a reorganization and refolding process of the polypeptide over the tubular network, indicating that the strength of this biomolecule stays in its capability to adapt to the surface that interfaces. Remarkably, the same trend is evidenced when B3 is simulated adsorbed onto the flat surface of graphene: increase of the contact area (from 346.3 to 410.2 $Å^2$) is coincidental with a considerable increase of the binding energy (from -7.32 to -9.34 kcal mol^{-1}) and the enhancement of the number of H-bonds (from 6 to 12). Once again, the major contribution comes from the aromatic His and Trp aa, this time found lying parallel to the graphitic surface. The main difference concerns the lack of conformational rearrangement on graphene, the simulation of which shows a more stable

protein backbone Root Mean Square Deviation (RMSD) compared to the simulation with the CNT (0.76 and 2.07 Å, respectively). The comparable results obtained with the two GNMs unveil the versatility of this polypeptide exerting a similar binding affinity for the nanomaterials understudy but with a different dynamic of adsorption. The importance of the peptide flexibility, which supports multiple strong binding conformations, was further stressed.

Similarly, Walsh and co-worker applied their validated implementation of the AMOEBAPRO force field to study the interaction of the strong binders polypeptides B1 and B3[109] both adsorbed on CNT and graphene.[158] The aromatic Trp, peculiarity of the two peptides and responsible of the binding to CNT, was systematically mutated with Tyr (B1Y and B3Y) and Phe (B1F and B3F) and simulated adsorbed on the two nanomaterials via 10 ns long MD simulations. The authors proved that the chosen polarized force field was able to successfully describe non-covalent interactions such that they decided to treat implicitly the solvent contribution.

It clearly emerged that the mutation of Trp with either Tyr or Phe exponentially decreases the normalized interaction energy (interaction energy between the peptide and surface divided by the number of the atoms in the peptide) of the mutants with both CNT and graphene. Indeed, monitoring the radial distribution functions (RDFs) of each residue within the simulated systems, it was found a high distribution of Trp close to the nanomaterials, whereas the distribution of Tyr and Phe mutants was found abundant far from the surface. Additionally, while B1 and B3 display aromatic residues preferentially parallel to the surfaces as the ring-tilt angle demonstrates, all mutants show less ring orientation stability. The aromatic aa ring-tilt angle could indeed vary from 0° (parallel) to 90° (perpendicular to the surface), assuming a continuous rotation of the peptide aromatic rings at the interface (Figure 30a-c).

It is worth noting that all the aromatic residues of the peptides understudy hold increased orientation stability on graphene in comparison with the tubular framework (Figure 30a-c). However, the aromatic orientation is not the only criterion influencing the stabilization of the peptide/nanomaterial complex. In fact, the decrease of binding energy is observed even when the aromatic mutants are displayed parallel to the surface. As example, the authors provided pictures clearly showing a weaker-bound B1Y conformation that, though anchored to graphene through the aromatic Tyr, looses at the same time the contact of other non-aromatic aa and their plausible contribution to the binding energy (Figure 30d).

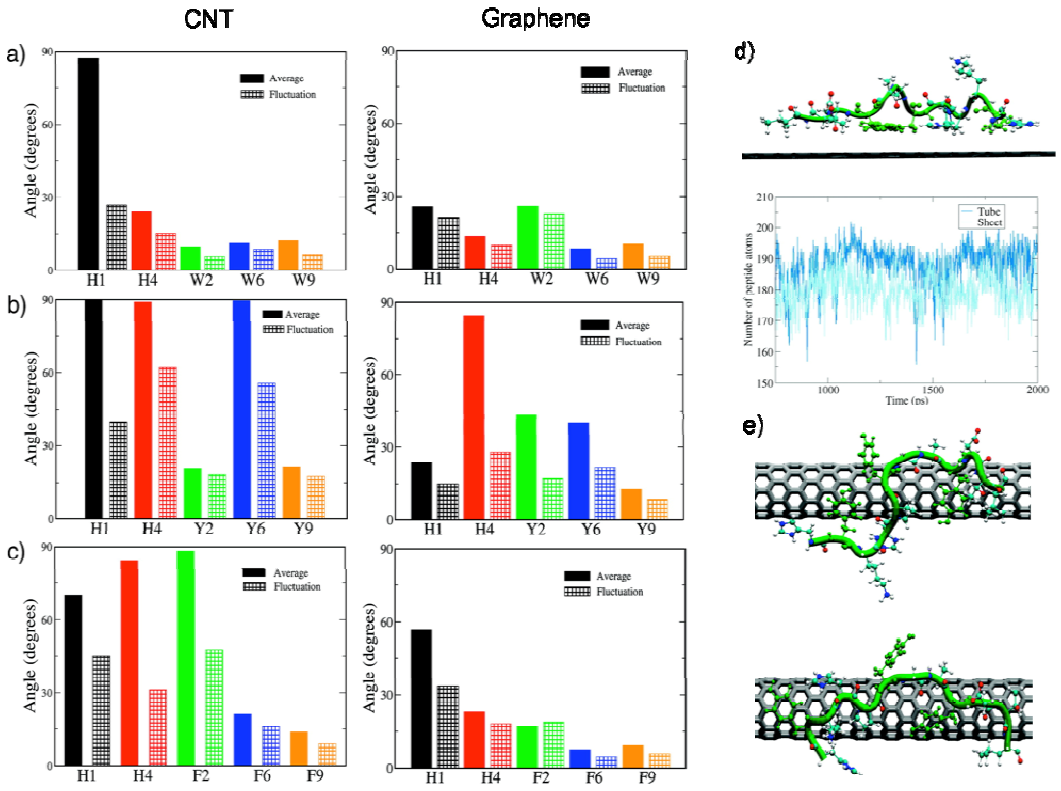

Figure 30. Average and fluctuation of the ring-tilt angle of all the aromatic aa within B1 (a), B1Y (b) and B1F (c) interfacing CNT and graphene. Structural representation of B1Y simulated adsorbed onto graphene (d). Number of atoms within B1 in contact with CNT (sky-blue) and graphene (turquoise) plotted as a function of simulated time (d, bottom). Snapshot of conformations of B1Y interacting with CNT from two different simulations (e). Adapted with permission from ref. 158. Copyright 2009, American Chemical Society.

Looking at the total number of peptide atoms in contact with the graphitic surface, a major number was found at the interface with CNT rather than with the flat graphene (Figure 30d). This is due to the higher flexibility of the B1Y, for instance, adsorbed onto the CNT whose different adopted conformations represent all possible and strong-binding orientations (Figure 30e).

In line with what stated by Gianese *et al.*,[157] peptide affinity can be partially ascribed to its ability to assume a variety of conformations at different interfaces. When the interface is represented by GNMs, no matter whether tubular or planar, the aromatic contribution governs the interaction ranked as follow Trp > Tyr > Phe. As observed above, the protein flexibility can induce the adsorption of the same polypeptide chain to CNT and graphene with comparable binding affinity but with a different dynamic process. At the same time, recently Yarovsky and co-workers demonstrated how the same peptide can adsorb on

different GNMs with different dynamics and binding affinity due to both the protein flexibility and the surface' size and shape.[159] The authors investigated the interaction between GNMs and an amyloidogenic peptide apoC-II(60-70) by means of classical MD simulations in explicit solvent and DFT+D/PBE calculations to explore the relationship of carbon surfaces with amyloid fibrillation.[159] The binding affinity of this polypeptide was demonstrated to inversely scale with the increasing curvature of the nanomaterial, which from graphene to C_{60} has drastic reduction in the exposed surface prone to protein adsorption. During the 100 ns MD simulation of the 79 aa polypeptide onto each graphitic surface, the aromatic aa Tyr and Phe were found to act as anchor points regardless of the type of GNMs (Figure 31a).

Aside from this preliminary similarity, a different profile of the protein contact stabilities at the interface with the GNMs was figured out: clearly, apoC-II(60-70) was stably adsorbed onto graphene more than on CNT and C_{60}. For instance, when the polypeptide is adsorbed onto the smaller spherical GNM, it hardly anchors the C_{60} due to the small and curved surface available, whereas it undergoes intense conformational changes alternating between a β-hairpin arrangement where the aromatic aa can stack between them or with the carbon cage (Figure 31b). Conversely, Tyr and Phe allow for an elongated and extended conformation upon adsorption onto CNT and graphene (Figure 31b).

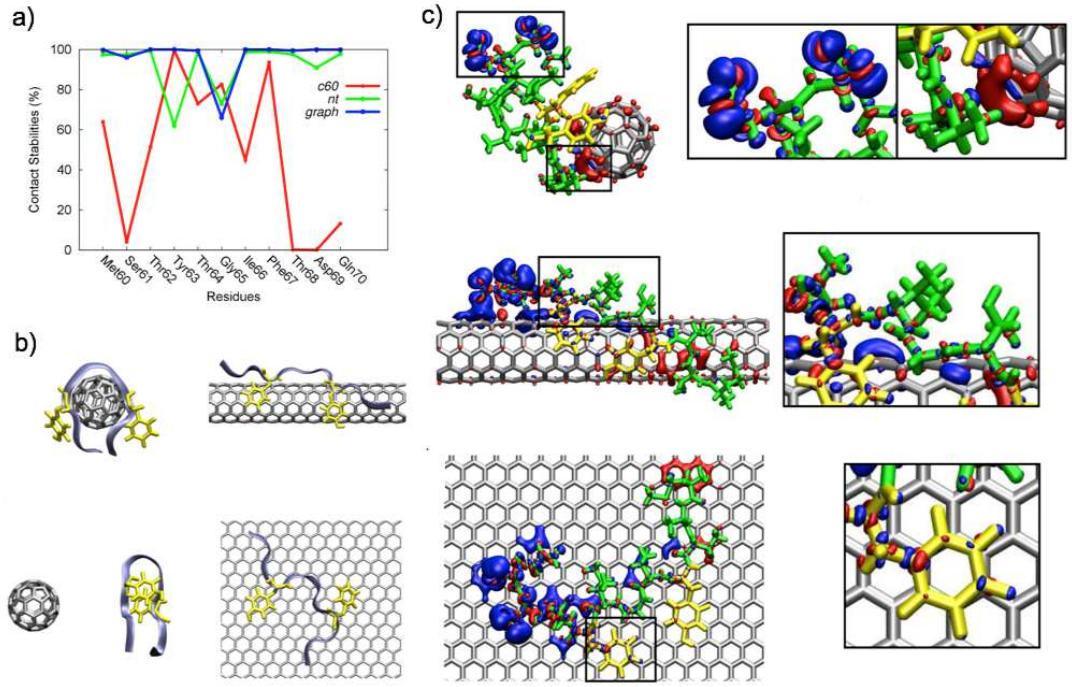

Figure 31. a) Contact stability of the residues within the apoC-II(60-70) structure interacting with C_{60} (red line), CNT (green line) and graphene (blue line). b) Favorable peptide conformation adsorbed onto the nanomaterial or desorbed as for C_{60}. c) The electron density difference maps shows the charge accumulation (red) and the charge depletion (blue) mapped on the complexes. Adapted from ref. 159.

Umbrella sampling simulations nicely showed that the dissociation free energy for the peptides in solution decreases remarkably with increasing the curvature of the graphitic material (1.8, 8.6 and 15 kcal/mol higher dissociation free energies, for C60, CNT and graphene, respectively) considering also different possible binding modes of the peptide on the carbon based material. As clarified by DFT calculations C_{60}/peptide and CNT/peptide complexes are 125 and 41 kcal mol^{-1} less stable than the graphene/peptide adduct, respectively. In line with this, reducing the degree of curvature it increased the aromatic contact area calculated for each complex (0.92, 1.19 and 1.72 nm^2 for C_{60} CNT and graphene, respectively). Additionally, by mapping the electron density displaying in red the charge accumulation and in blue the charge depletion, intra-peptide electrostatic interactions influence the peptide's secondary structure and, thus, its binding affinity to the nanomaterial (Figure 31c). Hence, the combination of the proteinic conformational freedom, such that of the polypeptide apoC-II(60-70), and the nanomaterial's curvature and size is demonstrated to yield a radically different way of interaction where the maximization of the contact area and the aromatic stacking are favored onto the GNMs.

However, polypeptide behavior can drastically change if another aminoacidic sequence is taken into account. For instance, Zuo *et al.* reported on the comparative study of the interaction between a small subdomain (35 aa) of the Villin Headpiece (HP) protein, HP35, and graphene, CNT and C_{60} by means of extensive MD simulations.[160] During the 500 ns simulated time scale, the interaction with graphene was mainly driven by the aromatic residues within the HP35 sequence, namely the Trp and Phe, that were inducing the peptide conformation towards their better exposition and the attainment of π□π stacking with the planar graphitic surface. This was nicely supported by the contact probability as a function of the interaction energy calculated for each HP35 residues facing the three nanomaterials: all the residues are favorably interacting (negative interaction energy values as reported in the plot in Figure 32) with graphene and in particular the aromatic Phe35, Trp23 and Phe10 aa exhibit more than 80% of contact probability (blue colored residues in Figure 32).

On the other hand, the tubular surface of CNT maintains a favorable contact with the aromatic residues (Phe35 and Trp23), whilst with a reduced interaction energy and %

(among 60 and 80 %, cyan colored residues) of contact probability (Figure 32), along with a significant contribution of Lys30 and Gln26, which follow the curved geometry with their alkyl chains. Finally, the interaction energy of the residues adsorbed onto the curved C_{60} surface display hardly negative values and poor stacking ability of the aromatic aa with their 20% of contact probability.

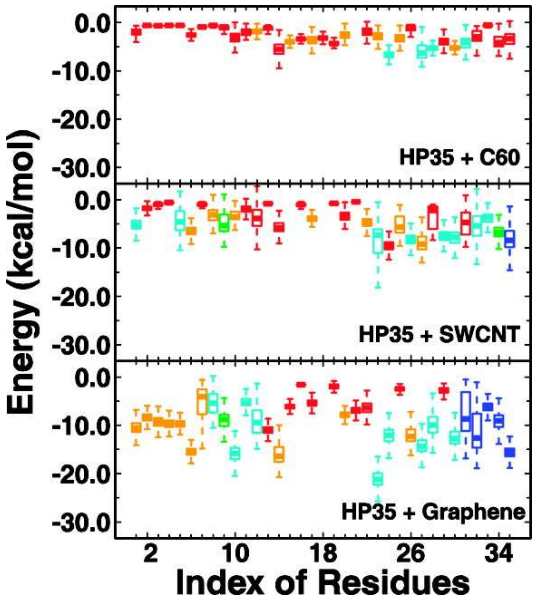

Figure 32. Interaction energy of each HP35 residue and C_{60}, CNT and graphene. The residues are colored according to the contact probability: 0-20% (red), 20-40% (yellow), 40-60% (green), 60-80% (cyan), and 80-100% (blue). Reprinted with permission from ref. 160. Copyright 2011, American Chemical Society.

Following the same comparative approach, recently Yao and co-workers studied the fibrillation process of the Islet amyloid polypeptide fragment 22-28 ($IAPP_{22-28}$) on graphene, CNT and C_{60} by means of extensive MD simulations.[161] This oligomer is known to aggregate in β-sheets like fibrils driven by inter-peptide hydrophobic interactions within its "NFGAIL" sequence. Hence, in order to reproduce the fibrillation process an increased concentration of $IAPP_{22-28}$ (4 and 8 peptides) was simulated alone and in proximity of the GNMs (Figure 33a-b).

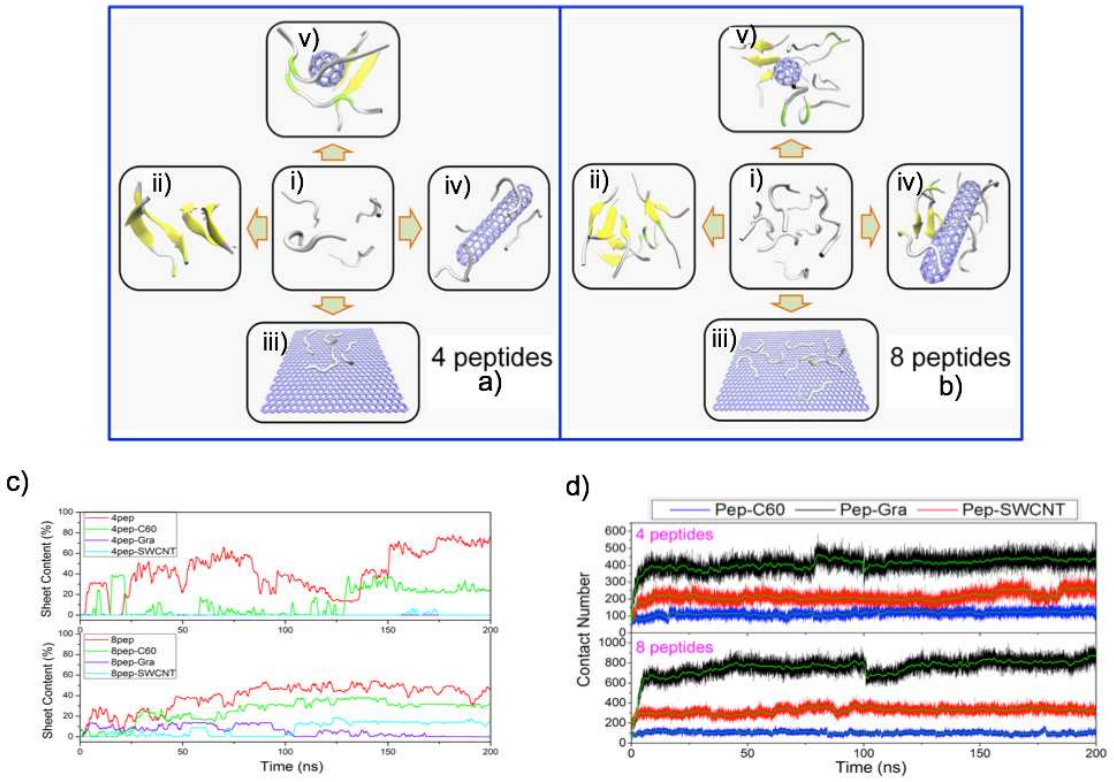

Figure 33. Schematic representation of the starting structures of 4 (a) and 8 (b) peptides alone (i). The conformations after 200 ns simulation of the peptides alone (ii) and in complex with graphene (iii), CNT (iv) and C_{60} (v) are reported. c) β-sheet content as a function of the simulated time is plotted for all the systems. d) Contact number as a function of the simulated time between the peptides and graphene (black lines), CNT (red lines) and C_{60} (blue lines) are reported. Adapted from ref. 161.

Notably, to the formation of fibrils corresponds the increase of β-sheets, whose content was therefore monitored along the 200 ns simulation time in explicit solvent. Interestingly, a β-sheets content of 0% was found when 4 $IAPP_{22-28}$ peptides were simulated in the presence of the flat graphene and the tubular CNT (respectively violet and turquoise lines in Figure 33c). The same β-sheets content was found for the 8-peptide system on graphene, slightly higher on CNT (20%). On the other hand, in the presence of C_{60} two peptides out of four were able to form β-sheets with a 74%, six out of eight with 81%. These behaviors find explanation in the major contacts that the $IAPP_{22-28}$ polypeptides are able to entertain on both graphene and CNT with respect to C_{60} rather than with themselves (respectively black, red and blues lines in Figure 33d). Furthermore, it is worth noting that increasing the number of peptide on C_{60} the number of contacts remains constant, stably

oscillating around 100 (Figure 33d). Analyzing more in depth the nature of these contacts, it results that the aromatic (Phe) and hydrophobic (Ile and Leu) residues of $IAPP_{22-28}$, responsible of the inter-peptide interactions that induce the fibrillation, are now occupied in strong contact with graphene and CNT. Conversely, this is not verified with the spherical cage.

It is evident that the increased available surface of graphene and CNT favors hydrophobic and π-π stacking interactions with $IAPP_{22-28}$ that block the fibril formation, whereas C_{60}, unable to entertain interactions as much as the others GNMs, has a smaller inhibition effect. Additionally, the behavior of a single peptide (examples listed before) can vary as a function of its concentration.

4.3 Graphene and proteins

In the view of evaluating the bioapplicability and biosafety of graphene, several studies have been reported investigating the interaction of the flat 2D allotrope of carbon with numerous proteins, often chosen considering their importance, functionality and abundance in the human blood and body. As already stressed before, when it comes into studying the non-covalent approaching of proteins to GNMs, the tertiary structure of the formers certainly influences the dynamic of adsorption especially on the planar graphitic surface, where the available contact surface is much higher. The multiplicity of the protein repertory displays a variety of globular, multidomains proteins made up of a different combination of secondary structure elements. Needless to say that proteins characterized by only α-helix rather than β-sheets or a combination of the two might interact differently with the graphitic surface. Furthermore, the distinction of the so-called "hard" proteins, those with peculiar internal structure stability, and "soft" proteins, those with low internal stability, reasonably might depict a different scenario in the protein/nanomaterial interaction.[162]

At this regards, Raffaini and Ganazzoli tackle the issue by performing several short MD simulations in a dielectric medium or with a few thousand of water molecules to study solvent distribution around the proteins, comparing the adsorption onto graphite sheets of albumin,[163,164] as the most abundant blood protein, fibronectin,[165] as important protein involved in the blood-clotting cascade, and lysozyme,[166] an essential enzyme involved in hydrolysis of bacterial cell walls. The proteins understudies are not only relevant biomolecules involved in biological and pathological processes, but are also representative of diversified structural features that will allow to draw a picture of the interaction of globular proteins and nanomaterial. In fact, albumin is a globular protein predominantly characterized by α-helixes and the subdomains A and E chosen for the simulations counts 3

α-helixes each, with an amphiphilic character the former and a mean hydropathy value the latter; fibronectin type I module is another globular protein but consisting exclusively of antiparallel β-sheets, while lysozyme comprises both α-helixes and β-sheets in its globular structure.

The validated protocol proposed by the authors consists of a first minimization step of the starting structures adopting different orientations in the surface proximity; the best and the worst ranked orientations were then subjected to MD simulations by using consistent valence force field CVFF in implicit solvent, which allows to achieve reasonable results (as compared to explicit solvent simulations) in a very short time scale (up to 7 ns).[163,165,166] According to their outcomes, during the minimization step, all the biomolecules tend to approach the graphitic surface regardless of the type of secondary structure or of the starting orientations, revealing, at a visual inspection, partial loss of the secondary structure of the protein section in contact with the surface (Figure 34a). The worst interaction mode is often the one oriented with the long axe of the protein perpendicular to the surface (fibronectin and lysozyme Figure 34a bottom). Interestingly, in the three cases the number of contact residues linearly correlates with the interaction energy, ($E_{int} = (E_{free\ prot} + E_{CNT}) - E_{tot}$), and the protein strain energy ($E_{strain} = E_{adsor} - E_{free}$) calculated for the minimized geometries in different possible orientations (Figure 34b). Additionally, the best-fit line through the origin of the E_{int}, energy required to desorb the protein from the surface, and the E_{strain}, energy require to deform the protein upon adsorption compared to the native state, were also derived. E_{int} of 71 (3), 54 (1) and 59 (2) kJ mol^{-1} were obtained for albumin, fibronectin and lysozyme respectively, suggesting a major adsorption of the α-helical globular albumin followed by the mixed α-β lysozyme and the β-sheets fibronectin. On the other hand, E_{strain} of 17 (1), 13 (1) and 12.7 (0.8) kJ mol^{-1} were obtained for albumin, fibronectin and lysozyme respectively, implying larger structural rearrangements occurred for the α-helical globular protein.

Investigating further the dynamic of adsorption by performing 1 ns MD simulation, the globular proteins proceed towards the complete adhesion on the planar network, inducing intense structural rearrangements to maximize the contact points (Figure 34c). The number of albumin aa in contact with the surface significantly increases passing from a maximum of 23/60 in one of the minimized orientations, to the complete aa contact resulting in a monolayer of aa coating the surface (59/60 aa at less than 5 Å far from graphite).[163]

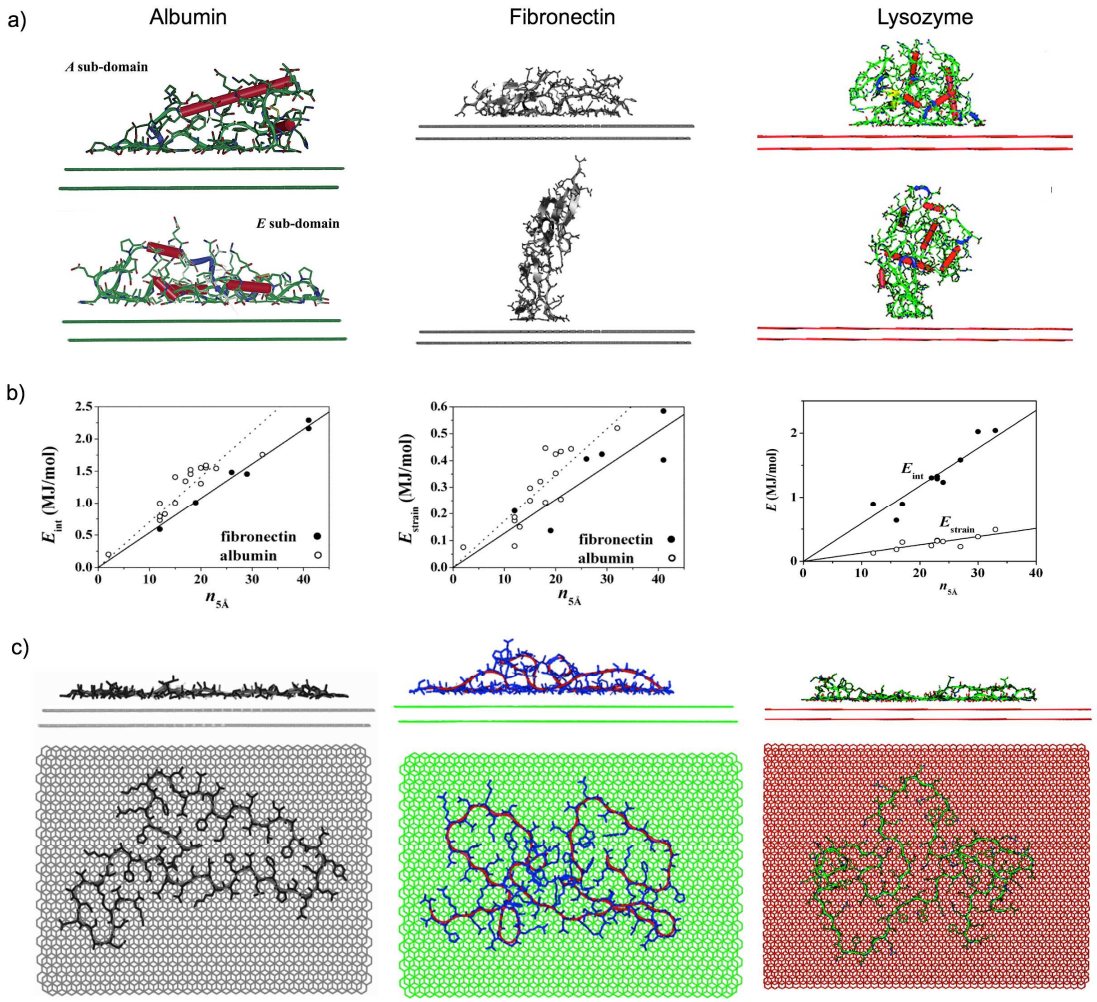

Figure 34. a) From left to right: minimized orientations of two subdomains of albumin, the best (top) and the worst orientations (bottom) of fibronectin and lysozyme. b) Linear correlation between the E_{int} and E_{strain} and the number of contact aa ($n_{5Å}$). c) Side and top view of the final adsorbed proteins after 1ns MD trajectory. Adapted with permission from refs. 164, 165 and 166. Copyrights 2003, 2004 and 2010, American Chemical Society.

Similarly, fibronectin from an initial maximum contact of 41/93 aa, adsorbs 68/93 aa onto the surface and no β-sheets are retained (Figure 34c). Nonetheless, a unique monolayer was not observed in the adsorption of fibronectin, which presents a net of disulfide bonds that holds together the structure preventing it from the complete spreading.[165] This divergent behavior can also refer to the different nature of albumin and fibronectin, considered as a soft and hard proteins,[162] correspondingly.

On the other hand, the lysozyme adsorption was always occurring through the β-sheets side which, probably holding higher affinity to the flat geometry, is the first to adsorb

and lose its secondary structure information.[166] In this case, the adhesion process was followed by the radius of gyration (Rg) of the whole molecule and by the diagonalization of the Rg tensor in its component x, y, z which correspond to the parallel (Rg_x and Rg_y) and perpendicular (Rg_z) directions of the protein to the surface. Remarkably, while Rg_x and Rg_y were increasing during the simulations of the two orientations of lysozyme (from 7.13 and 6.75 Å to 21.67 and 14.56 Å, respectively), the Rg_z was visibly reduced (from 10.18 Å to 2.05 Å considering the least favorable selected orientation), meaning a full parallel spreading of lysozyme as well at the end of the simulation (Figure 34c).[166] As a general trend, all the globular proteins analyzed by Raffaini *et al.* tend to favorably adsorb onto the graphitic surface with a two-steps process: a first adsorption phase where one side of the protein approaches the nanomaterial with local rearrangement of the secondary structure, followed by a complete surface coverage with the formation, in some cases, of one aa monolayer lying on the graphitic network with no secondary structure retention.

In line with the aforementioned reports, another comparative study was recently carried out by Guo *et al.*, which performed extensive MD simulations in explicit water to model the adsorption of WW domain (full β-sheets), BBA protein (mixed α-helix and β-sheets) and λ-repressor (α-helix) on the graphene surface.[167] Placed 10 Å far for the graphitic platform, after 100 ns the three proteins, for which two possible orientations were simulated each, were tightly adhered to the surface (Figure 35).

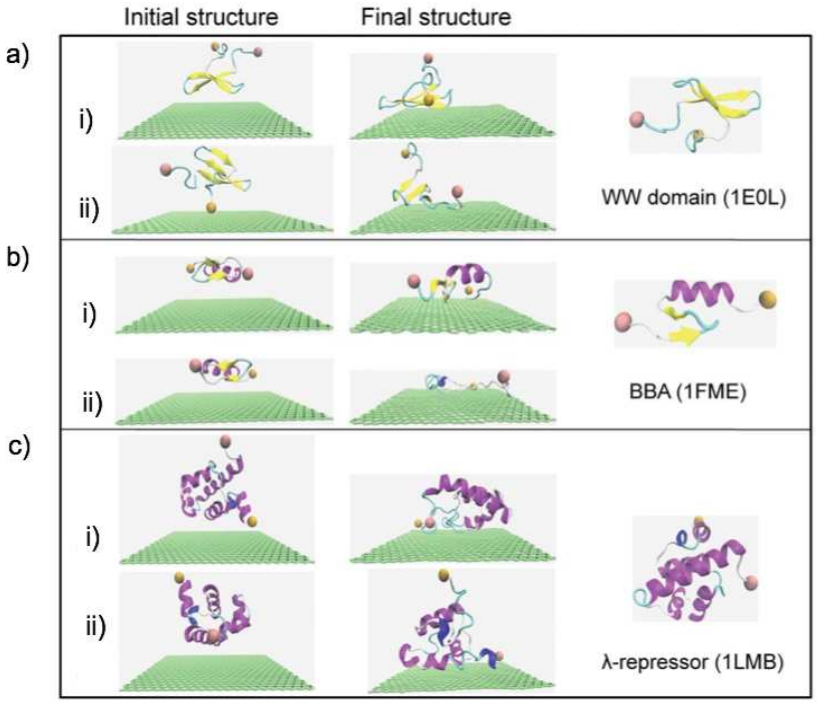

Figure 35. Starting and final geometries of two orientation (i and ii) of WW domain (a), BBA (b) and λ-repressor (c) after 100 ns MD simulations. Adapted from ref. 167. Copyright 2014, Royal Society of Chemistry.

As a matter of fact, all the three proteins similarly display an increasing contact area along the simulation time as a sign of their adsorption and stabilization at the interface with the nanomaterial. Nevertheless, a more in depth analysis reveal some structural and dynamical differences. In fact, the energetic profile reveals that the proteins interacting with the α-helix side, namely BBA in the ii) orientation (Figure 35b-ii), and both orientations of λ-suppressor, bind with higher binding free energy calculated with Molecular Mechanics Poisson Bolzmann Surface Area (MM-PBSA) (-151.65, 136.77 and -119.10 kcal mol^{-1}, respectively) compared to the full β-sheet WW domain and the β-sheets orientation of BBA protein, the energies of which are indeed lower and similar among them (-86.56, -79.36 and -86.49 kcal mol^{-1}). Moreover, by looking at the energetic decomposition, a major vdW contribution can be appreciated produced by the actual interacting residues, whose different location within the six simulated complexes depends on the related orientation (magenta squares in Figure 36).

For instance, while only the residues at the two extremities are shown to contribute the most for BBA-gra(i) complex, a major number of residues distributed allover the protein in BBA-gra(ii) orientation are found to actively interact with the surface, thereby explaining the higher interaction energy displayed by this orientation (Figure 36b). Interestingly the maximization of the contact points is accompanied by different secondary structure dynamics: when the full β-sheets WW domain is adsorbed onto graphene no secondary structure loss is detected for both the orientations (sheet content is 32.43% at the beginning and 29.73 and 35.14% at the end of the simulation for two different orientations, respectively) as also observed when the mixed α-β BBA is interacting with graphene throughout its β-sheets side (β-sheets content is 14.29% for both initial and final conformations, α-helix 35.71% and 32.14% at the beginning and at the end, respectively). Conversely, BBA adsorbed with the α-helix side considerably loses its secondary structure (β-sheets content drops from 14.29% to 0 and the α-helix content from 35.71% to 10.71%), alike the λ-suppressor behavior, which partially loses its α-helix content (from 67.50% to 52.50% and 50% for the two orientations, respectively). Therefore, the orientations interacting more strongly to the graphitic surface are those adsorbed through the α-helix

portion of their structure, which more easily undergoes structural rearrangements to maximize the contact points and stabilize the interaction.

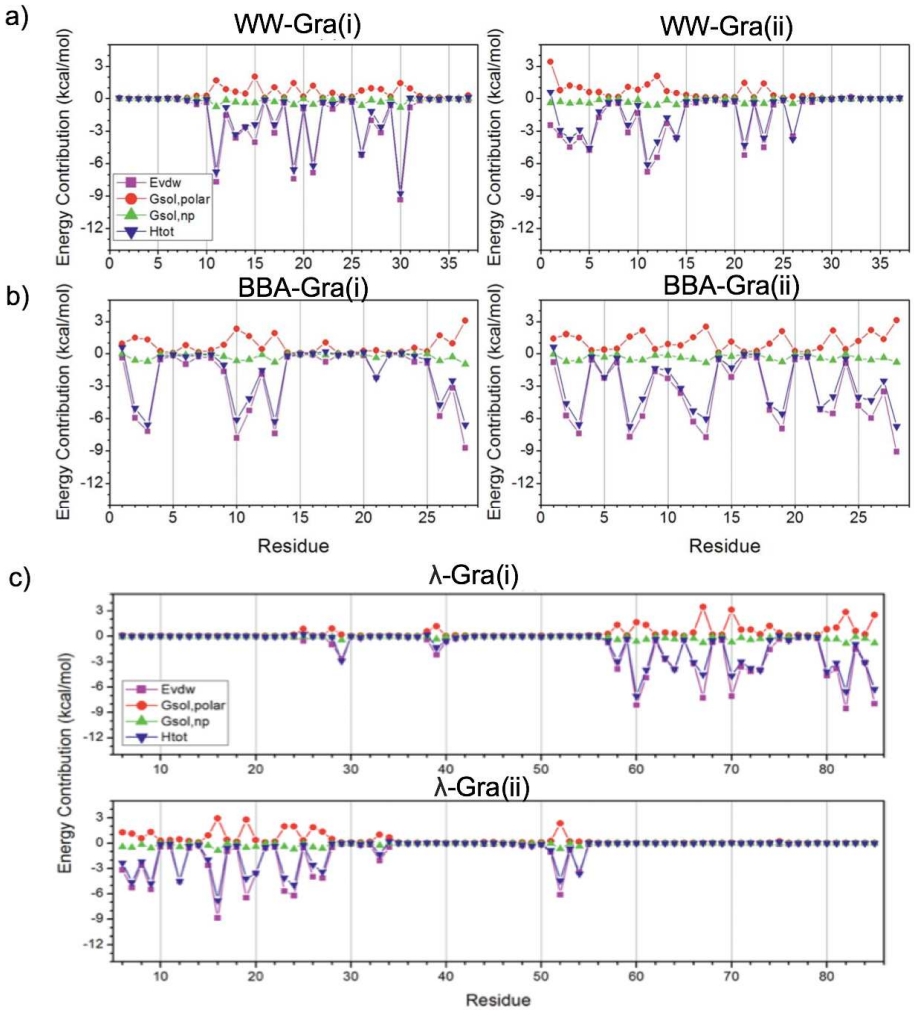

Figure 36. Interaction energies plotted as a function of the simulated time for WW domain (a), BBA (b) and λ-repressor (c) in the two orientation i) and ii). Adapted from ref. 167. Copyright 2014, Royal Society of Chemistry.

Hence, in a scenario in which globular proteins spontaneously interact and tightly adsorb on the flat graphitic surface, it results a major stability of the β-sheets elements over the α-helix.[167] In the adsorption process of globular proteins, considerable structural rearrangements are envisaged causing an increase of the molecular fingerprint along with a loss of the secondary structure folding.[168] Additionally, it has been demonstrated that adsorption of globular proteins induces a flat coating over graphene with a particular parallel

orientation among the strands,[169] assuming an active role of the graphitic template in the amyloid fibrillation.[44]

In parallel, a notable work, aimed at exploiting the β-sheets stabilization and organized assembly directed by the flat graphitic surface, was reported first by Brown *et al.* whom experimentally demonstrated the patterned adsorption and arrangement of a *de novo* designed protein onto graphite.[170] AFM images clearly proved that the deposition of an amphiphilic β-strands on highly ordered pyrolitic graphite (HOPG) leads to the nucleation of fibers with 120° orientated symmetry induced by the hexagonal graphitic template. FTIR probed the antiparallel β-sheets formation with the typical peak at 1621 cm^{-1}.

Furthermore, Wang and co-workers reported on the patterned adsorption of peptides organized in β-sheets upon deposition on the flat HOPG surface with a particular focus on the peptide sequences.[171] In particular, they studied the behavior of two synthetic model peptides, namely $R_4G_4H_8$ and $F_4G_4H_8$, adsorbed onto HOPG by STM images and rationalized the experimental evidences with theoretical studies.[171] The two peptides differ in their sequences by the presence of Arg (R) and Phe (F) aa, which are both followed by four Gly (G) and eight aromatic His (H) residues. Interestingly, the STM images revealed not only the formation of extended aligned lamellae (Figure 37a-b), but gave also significant insights at the atomistic level. The authors found that each peptide strand, aligned in the β-sheets organization, is characterized by three bands with different brightness and lamellae width that nicely account for the corresponding sequence (Figure 37a-ii and b-ii): in the $R_4G_4H_8$ sample, the first band displays a width of 1.2 nm for the 24.5% of the full-length peptide, the second band a width of 1.0 nm for a 25% and the third a width of 2.4 nm for the 49% of the full-length peptide.

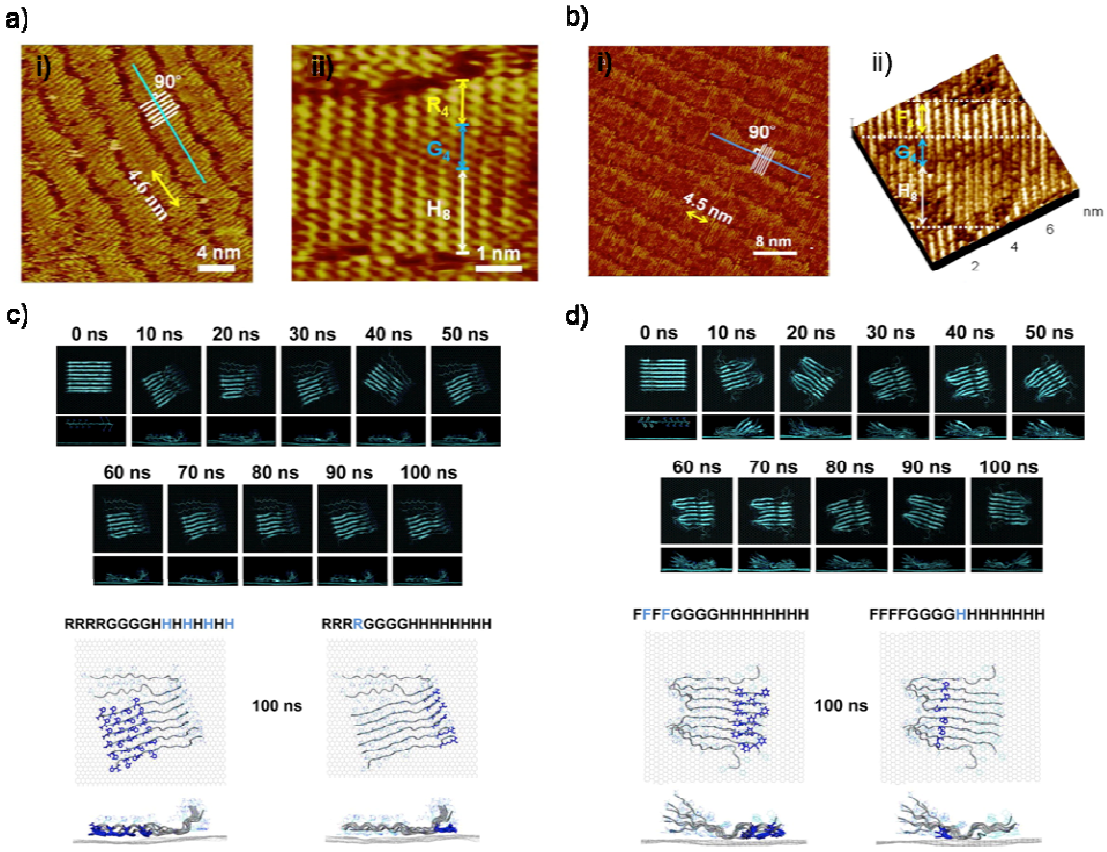

Figure 37. STM images of the $R_4G_4H_8$ (a) and $F_4G_4H_8$ (b) aligned on HOPG surfaces. The three bands with different brightness and length can be distinguished corresponding to the relative sequences (ii). MD simulation snapshots of the $R_4G_4H_8$ (c) and $F_4G_4H_8$ (d). Adapted with permission from ref. 171. Copyright 2013, American Chemical Society.

The width values (1.2:1:2.4) and the % proportion (24.5:25:49) perfectly match with the $R_4G_4H_8$ sequence. Similarly, a proportion of 1.3:1:2.4 nm corresponding to the 28.6:22.4:53% of the total length peptide was observed for $F_4G_4H_8$ peptide. Furthermore, from the STM images was clearly noted that each strand, organized in a parallel orientation as demonstrated by the FTIR, are not perfectly aligned but shifted probably due to inter-peptides interactions. By normalizing the brightness intensity to the reference residue H_8, it was possible to rank the four aa following the order Phe > His > Arg > Gly.

For a deep comprehension of the conformational and dynamics of adsorption, MD simulations aided the experimental observations, ultimately confirming the atomistic details drawn experimentally. 100 ns MD trajectories in explicit solvent were therefore carried out

simulating ten strands of $R_4G_4H_8$ and $F_4G_4H_8$ organized in parallel β-sheets onto graphite surface.

The β-sheets were found to stably interact with the graphitic surface with a slightly shifted alignment showing the aromatic residues anchoring the platform via π-π stacking interactions, while the positively charged Arg interact through their alkyl side chain pointing towards the solvent the guanidinium group (Figure 37c-d). Additionally, the interaction energy perfectly correlate with the brightness intensity detected by the STM images following the trend Phe > His > Arg > Gly of the most interacting residues.

A practical application, exploiting the high affinity of protein for the planar graphitic surface, was reported in the work by Laanksonen *et al.* that employed the amphiphilic microbial adhesion protein HFBI, known to strongly adsorb onto hydrophobic surfaces, to non-covalently bind graphite sheets and promote their exfoliation upon sonication.[172] The method efficiently produces single graphene sheet, as demonstrated by TEM, SEM and Raman measurements. Moreover, to prove the retained activity of the adsorbed protein, variations of HFBI protein were produced and employed in the validated exfoliation procedure. The exfoliated flakes with the modified protein were then labeled through AuNPs able to bind the modified HFBI, as TEM and AFM images nicely confirmed.

So far we highlighted the stable and spontaneous interaction of globular as well as planar proteins with the flat graphitic surface undergoing structural rearrangements that, involving both the tertiary and secondary structures, are directed to the maximization of the whole molecule contacts with the surface. However, having stated the general affinity of proteins to non-covalently attach CNTs as well (see section 4.3), a comparison is now required to evaluate the effect of the curvature and topography of the nanomaterial on the interaction strength and on the dynamics of adsorption of proteins on the GNMs surfaces.

At this regard, Raffaini *et al.* carried out a comparative theoretical study evaluating the behavior of the same model proteins probed on graphite,[163,165] namely albumin and fibronectin, now adsorbed on different diameter CNTs and graphene,[173] by applying the same protocol as the aforementioned works. After the minimization step, both albumin and fibronectin adhered to (8,8) (Figure 38a), (10,10)CNTs (Figure 38b) and graphene (only albumin Figure 38c) with local structural rearrangements at the interface with the graphitic surfaces.

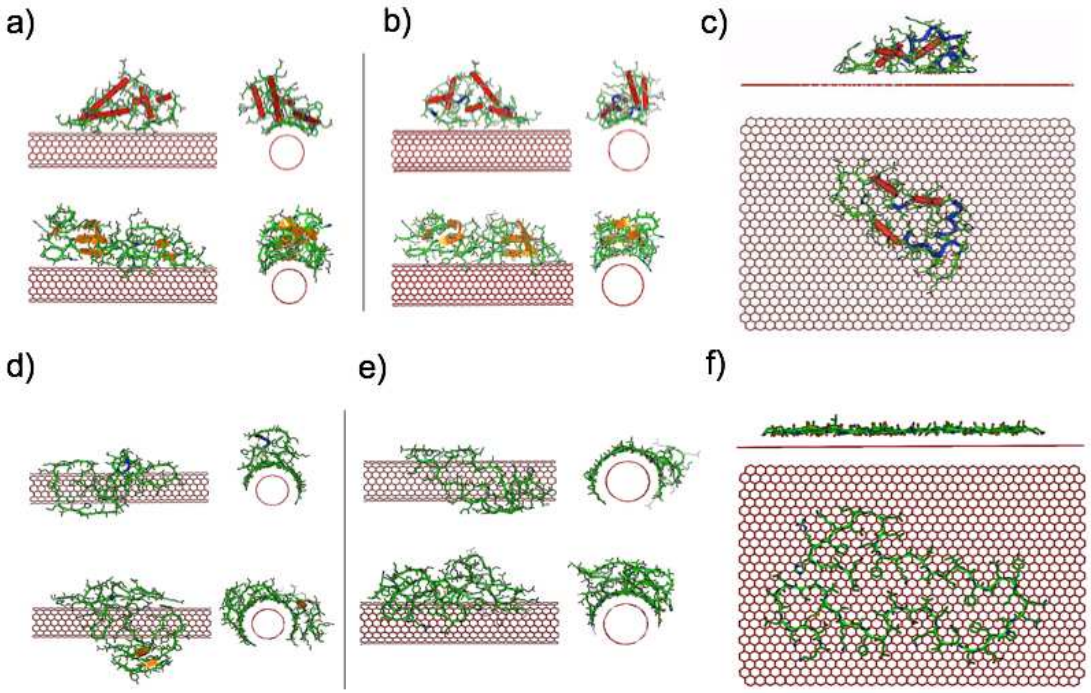

Figure 38. Minimized orientations of albumin subdomain and fibronectin adsorbed on (8,8) (a), (10,10)CNTs (b) and graphene (only albumin, c). The most stable orientations of albumin subdomain and fibronectin adsorbed on (8,8) (d), (10,10)CNTs (e) and graphene (only albumin, f) after MD simulations. Adapted with permission from ref. 173. Copyright 2013, American Chemical Society.

The same linear correlation was found between the E_{int}/E_{strain} and the number of contact residues, while the best-fit line through the origin describes significant differences among each other. Interestingly, the adsorption of albumin onto the one sheet graphene yields similar E_{int}/E_{strain} compared to the simulations on graphite (54.7 (0.9)/11.3 (0.5) and 57 (1)/17(1) kJ mol^{-1}, respectively), whereas lower values were found for the albumin adsorbed on CNT with different diameter (30.7(1.1)/9.2(0.7) and 33.8(1.3)/9.2(0.7) kJ mol^{-1} on (8,8) and (10,10) CNTs, respectively). After 2 ns long MD simulations in implicit solvent, an increased coverage was achieved by both proteins on (8,8) (Figure 38d), (10,10) CNTs (Figure 38e) and on graphene (only albumin Figure 38f) with evident loss of the secondary structure information of the biomolecules spread on the surfaces. Remarkably, the energy values of E_{int} are hardly changed for the albumin/graphene complex (intrinsic E_{int} 53.3 kJ mol^{-1}) compared to the initial adsorbed geometry, while are significantly increased for albumin on (8,8) and (10,10) CNTs (intrinsic E_{int} 44.8 and 43.9 kJ mol^{-1}) as a measure of the increased interacting points. It is worth noting that very similar results are obtained for the

albumin subdomain on either the CNTs, certainly due to the small difference between the diameters taken into account, but especially to the 'soft' nature of this globular protein, which allows it for easier rearrangements and adaptations to the different graphitic surfaces. Conversely the 'hard' fibronectin more visibly differs in the intrinsic E_{int} values that vary from 38.8 to 47.0 kJ mol^{-1} once adsorbed on (8,8) or (10,10) CNTs, correspondingly. The comparable values obtained for graphene and graphite confirm that without changing the topography of the nanomaterial similar interaction strength are observed, while lower energy of interactions has been observed when CNTs are interfaced to.

5. Conclusions

Going through the most recent and representative examples in the field, in this *critical review*, we report a detailed overview of the theoretical and experimental studies unravelling the association forces ruling the non-covalent adsorptions of amino acids, polypeptides and proteins onto graphitic nanomaterials (GNMs) with a special focus on fullerenes, CNTs and graphene. The understanding and mastering of these association processes is a key point if one wants to design functional carbon-based hybrid materials for nanomedicinal applications. We therefore illustrated how progresses blossomed and are currently under development in the understanding of the non-covalent GNMs/proteins interactions ultimately leading to the control and engineering of new biocompatible materials for applications in the biomedical field as well as increasingly represent a guide to predict parasite adsorbing processes that would hit at toxicological implications.

The structural heterogeneity of CNTs and graphene sheets makes any experimental structural determinations and quantitative evaluations of the association complexes with proteinaceous systems experimentally difficult, thus not of sufficient accuracy to provide a unique and comprehensive picture of the governing physicochemical and structural features. In this respect an important aid toward the rationalization of the main forces ruling the non-covalent association process in this kind of systems comes from the computational biophysics/chemistry approaches where the level of approximation in modeling non-covalent interactions as well as a realistic representation of the system is crucial to the reliability of the final results.

From these combined experimental and theoretical efforts, it clearly emerges that, while amino acids and peptides can easily adapt to the shape of GNMs, the binding of proteins on curved GNMs is determined by shape complementarity[101] and it is essentially

governed by the number of the exposed hydrophobic, aromatic and charged residues. In particular, the aromatic aa residues (like Trp, Tyr, Phe) often act the main interfacial anchoring groups driving the adsorption of proteins to GNMs mainly via π–π-type stacking interactions,[83] whereas positively charged aa residues (like Arg and Lys) can favour cation-π contacts or act as polar groups allowing the dispersion of GNMs in aqueous media. These combined studies also revealed that the lowest is the curvature of the GNM the largest is the interaction with the proteins that, depending on its structure and degree of association, might lead to a distortion of its secondary or tertiary structure. For instance, the association of C_{60} and proteins is mainly driven by a shape-complementarity of the recognition site and the chemical structure of the aa endohedrally decorating the cavity. Aromatic and charged aa are particularly prone to interact with fullerene cages through π-π stacking and cation-π interactions.

In spite of the large number of theoretical and experimental studies, an in-depth atomistic investigation of the free energy landscape driving the binding mechanism of amino acids, peptides and protein towards GNMs under mimicking the working conditions is still at infancies and only preliminary works have been tackled. Similarly, it is not yet clear how the presence of the graphitic surface affects the folding kinetics of peptides or proteins, influencing in turn their function or their adsorption mode as influenced by the environmental effects (e.g. solvent, interfaces, physiological solutions to name a few).

Together with the advancements and the developments of new experimental characterizations tools enabling the quantification and structural determination of the intermolecular interactions between macromolecules, one can expect that the ever increasing computer power and theoretical efforts to improve the efficiency and the accuracy of the computational biophysical/biochemical methods[174–177] will progressively complement the experimental outcomes by synergistically understanding and valuing the physical and chemical properties to be used for the design and exploitation of novel biomaterials.

Acknowledgments

D.B. acknowledges the EU through the ERC Starting Grant “COLORLANDS” project, the FRS-FNRS (FRFC contracts n° 2.4.550.09), the Science Policy Office of the Belgian Federal Government (BELSPO-IAP 7/05 project), the “TINTIN” ARC project (09/14-023), the MIUR through the FIRB “Futuro in Ricerca” (“SUPRACARBON”, contract n°

RBFR10DAK6). The Authors acknowledge Alberto De Leo for the artwork used in the TOC figure.

References

1. H. W. Kroto, J. R. Heath, S. C. O'Brien, R. F. Curl, and R. E. Smalley, *Nature*, 1985, **318**, 162–163.

2. S. Iijima, *Nature*, 1991, **354**, 56–58.

3. K. S. Novoselov, A. K. Geim, S. V Morozov, D. Jiang, Y. Zhang, S. V Dubonos, I. V Grigorieva, and A. A. Firsov, *Science*, 2004, **306**, 666–669.

4. W. Krätschmer, L. D. Lamb, K. Fostiropoulos, and D. R. Huffman, *Nature*, 1990, **347**, 354–358.

5. M. Maggini, G. Scorrano, and M. Prato, *J. Am. Chem. Soc.*, 1993, **115**, 9798–9799.

6. W. E. Billups and A. M. Ciufolini, Eds., *Fullerenes: Chemistry, Physics, and Technology*, John Wiley & Sons, 2000.

7. X. Wang, Q. Li, J. Xie, Z. Jin, J. Wang, Y. Li, K. Jiang, and S. Fan, *Nano Lett.*, 2009, **9**, 3137–3141.

8. J. W. G. Wilder, L. C. Venema, A. G. Rinzler, R. E. Smalley, and C. Dekker, *Nature*, 1998, **391**, 59–62.

9. T. W. Odom, J.-L. Huang, P. Kim, and C. M. Lieber, *J. Phys. Chem. B*, 2000, **104**, 2794–2809.

10. J. M. Stephanie Reich, Christian Thomsen, *Carbon Nanotubes: Basic Concepts and Physical Properties*, Wiley-VCH Verlag GmbH & Co. KGaA, 2004.

11. C. N. R. Rao, R. Voggu, and A. Govindaraj, *Nanoscale*, 2009, **1**, 96–105.

12. C. N. Rao, B. C. Satishkumar, A. Govindaraj, and M. Nath, *Chemphyschem*, 2001, **2**, 78–105.

13. J. Wu, W. Pisula, and K. Müllen, *Chem. Rev.*, 2007, **107**, 718–747.

14. K. P. Loh, Q. Bao, P. K. Ang, and J. Yang, *J. Mater. Chem.*, 2010, **20**, 2277–2289.

15. D. Jiang, B. G. Sumpter, and S. Dai, *J. Chem. Phys.*, 2007, **126**, 134701–134707.

16. M. J. Allen, V. C. Tung, and R. B. Kaner, *Chem. Rev.*, 2010, **110**, 132–145.

17. H. Y. Mao, S. Laurent, W. Chen, O. Akhavan, M. Imani, A. A. Ashkarran, and M. Mahmoudi, *Chem. Rev.*, 2013, **113**, 3407–3424.

18. H. Hong, T. Gao, and W. Cai, *Nano Today*, 2009, **4**, 252–261.

19. V. A. Zamolo, G. Valenti, E. Venturelli, O. Chaloin, M. Marcaccio, S. Boscolo, V. Castagnola, S. Sosa, F. Berti, G. Fontanive, M. Poli, A. Tubaro, A. Bianco, F. Paolucci, and M. Prato, *ACS Nano*, 2012, **6**, 7989–7997.

20. M. B. Lerner, J. D'Souza, T. Pazina, J. Dailey, B. R. Goldsmith, M. K. Robinson, and A. T. C. Johnson, *ACS Nano*, 2012, **6**, 5143–5149.

21. S. Okuda, S. Okamoto, Y. Ohno, K. Maehashi, K. Inoue, and K. Matsumoto, *J. Phys. Chem. C*, 2012, **116**, 19490–19495.

22. C. Samorì, H. Ali-Boucetta, R. Sainz, C. Guo, F. M. Toma, C. Fabbro, T. Da Ros, M. Prato, K. Kostarelos, and A. Bianco, *Chem. Commun.*, 2010, **46**, 1494–1496.

23. W. Wu, S. Wieckowski, G. Pastorin, M. Benincasa, C. Klumpp, J.-P. Briand, R. Gennaro, M. Prato, and A. Bianco, *Angew. Chem. Int. Ed.*, 2005, **44**, 6358–6362.

24. C. Ménard-Moyon, E. Venturelli, C. Fabbro, C. Samorì, T. Da Ros, K. Kostarelos, M. Prato, and A. Bianco, *Expert Opini. Drug Discov.*, 2010, **5**, 691–707.

25. G. Pastorin, W. Wu, S. Wieckowski, J.-P. Briand, K. Kostarelos, M. Prato, and A. Bianco, *Chem. Commun.*, 2006, 1182–1184.

26. S. L. Edwards, J. A. Werkmeister, and J. A. M. Ramshaw, *Expert Rev. Med. Dev.*, 2009, **6**, 499–505.

27. S.-T. Yang, Y. Liu, Y.-W. Wang, and A. Cao, *Small*, 2013, **9**, 1635–1653.

28. N. Yanamala, V. E. Kagan, and A. A. Shvedova, *Adv. Drug Deliv. Rev.*, 2013, **65**, 2070–2077.

29. G. Zuo, S.-G. Kang, P. Xiu, Y. Zhao, and R. Zhou, *Small*, 2012, **9**, 1546–1556.

30. X. Hu and Q. Zhou, *Chem. Rev.*, 2013, **113**, 3815–3835.

31. H. Ali-Boucetta and K. Kostarelos, *Adv. Drug Deliv. Rev.*, 2013, **65**, 1897–1898.

32. A. Hirsch, *Angew. Chem. Int. Ed.*, 2002, **41**, 1853–1859.

33. J. L. Bahr, E. T. Mickelson, M. J. Bronikowski, R. E. Smalley, and J. M. Tour, *Chem. Commun.*, 2001, 193–194.

34. F. Diederich and C. Thilgen, *Science*, 1996, **271**, 317–324.

35. M. Prato, *J. Mater. Chem.*, 1997, **7**, 1097–1109.

36. D. Tasis, N. Tagmatarchis, A. Bianco, and M. Prato, *Chem. Rev.*, 2006, **106**, 1105–1136.

37. P. Singh, S. Campidelli, S. Giordani, D. Bonifazi, A. Bianco, and M. Prato, *Chem. Soc. Rev.*, 2009, **38**, 2214–2230.

38. C. A. Dyke and J. M. Tour, *J. Phys. Chem. A*, 2004, **108**, 11151–11159.

39. V. Georgakilas, M. Otyepka, A. B. Bourlinos, V. Chandra, N. Kim, K. C. Kemp, P. Hobza, R. Zboril, and K. S. Kim, *Chem. Rev.*, 2012, **112**, 6156–6214.

40. A. W. Jensen, S. R. Wilson, and D. I. Schuster, *Bioorg. Med. Chem.*, 1996, **4**, 767–779.

41. V. Singh, D. Joung, L. Zhai, S. Das, S. I. Khondaker, and S. Seal, *Prog. Mater. Sci.*, 2011, **56**, 1178–1271.

42. L. Lacerda, A. Bianco, M. Prato, and K. Kostarelos, *Adv. Drug Deliv. Rev.*, 2006, **58**, 1460–1470.

43. M. Calvaresi, F. Zerbetto, V. F. Selmi, and C. G. Ciamician, *Acc. Chem. Res.*, 2013, **46**, 2454–2463.

44. C. Li and R. Mezzenga, *Nanoscale*, 2013, **5**, 6207–6218.

45. A. J. Makarucha, N. Todorova, and I. Yarovsky, *Eur. Biophys. J.*, 2011, **40**, 103–115.

46. D. Bitounis, H. Ali-Boucetta, B. H. Hong, D.-H. Min, and K. Kostarelos, *Adv. Mater.*, 2013, **25**, 2258–2268.

47. M. Mahmoudi, I. Lynch, M. R. Ejtehadi, M. P. Monopoli, F. B. Bombelli, and S. Laurent, *Chem. Rev.*, 2011, **111**, 5610–5637.

48. S. T. Stern and S. E. McNeil, *Toxicol. Sci.*, 2008, **101**, 4–21.

49. S. Sharifi, S. Behzadi, S. Laurent, M. L. Forrest, P. Stroeve, and M. Mahmoudi, *Chem. Soc. Rev.*, 2012, **41**, 2323–2343.

50. S. J. Klaine, P. J. J. Alvarez, G. E. Batley, T. F. Fernandes, R. D. Handy, D. Y. Lyon, S. Mahendra, M. J. McLaughlin, and J. R. Lead, *Environ. Toxicol. Chem.*, 2008, **27**, 1825–1851.

51. C. D. Walkey and W. C. W. Chan, *Chem. Soc. Rev.*, 2012, **41**, 2780–2799.

52. M. P. Monopoli, C. Aberg, A. Salvati, and K. A. Dawson, *Nat. Nanotechnol.*, 2012, **7**, 779–786.

53. I. Lynch and K. A. Dawson, *Nano Today*, 2008, **3**, 40–47.

54. M. Lundqvist, J. Stigler, G. Elia, I. Lynch, T. Cedervall, and K. A. Dawson, *Proc. Natl. Acad. Sci. U. S. A.*, 2008, **105**, 14265–14270.

55. M. Rahman, Laurent, S., Tawil, N., Yahia, L., Mahmoudi, *Protein-Nanoparticle Interactions - The Bio-Nano Interface*, Springer, 2013.

56. A. Bianco, T. Da Ros, M. Prato, and C. Toniolo, *J. Pept. Sci.*, 2001, **7**, 208–219.

57. D. Pantarotto, N. Tagmatarchis, A. Bianco, and M. Prato, *Mini Rev. Med. Chem.*, 2004, **4**, 805–814.

58. J. G. Rouse, J. Yang, A. R. Barron, and N. A. Monteiro-Riviere, *Toxicol. In Vitro*, 2006, **20**, 1313–1320.

59. T. Da Ros and M. Prato, *Chem. Commun.*, 1999, **8**, 663–669.

60. C. Ménard-Moyon, K. Kostarelos, M. Prato, and A. Bianco, *Chem. Biol.*, 2010, **17**, 107–115.

61. C. Klumpp, K. Kostarelos, M. Prato, and A. Bianco, *Biochim. Biophys. Acta*, 2006, **1758**, 404–412.

62. A. Bianco, K. Kostarelos, and M. Prato, *Expert Opin. Drug Deliv.*, 2008, **5**, 331–342.

63. Y. Yang, A. M. Asiri, Z. Tang, D. Du, and Y. Lin, *Mater. Today*, 2013, **16**, 365–373.

64. V. C. Sanchez, A. Jachak, R. H. Hurt, and A. B. Kane, *Chem. Res. Toxicol.*, 2012, **25**, 15–34.

65. S. Guo and S. Dong, *Chem. Soc. Rev.*, 2011, **40**, 2644–2672.

66. L. Lin, A. Liu, Z. Peng, H.-J. L. Lin, P.-K. Li, C. Li, and J. Lin, *Cancer Res.*, 2011, **71**, 7226–7237.

67. S. Bosi, T. Da Ros, G. Spalluto, and M. Prato, *Eur. J. Med. Chem.*, 2003, **38**, 913–923.

68. A. Bianco, K. Kostarelos, and M. Prato, *Curr. Opin. Chem. Biol.*, 2005, **9**, 674–679.

69. A. Bianco, K. Kostarelos, C. D. Partidos, and M. Prato, *Chem. Commun.*, 2005, 571–577.

70. X. Sun, Z. Liu, K. Welsher, J. T. Robinson, A. Goodwin, S. Zaric, and H. Dai, *Nano Res.*, 2008, **1**, 203–212.

71. L. Feng and Z. Liu, *Nanomedicine*, 2011, **6**, 317–324.

72. A. de Leon, A. F. Jalbout, and V. A. Basiuk, *Chem. Phys. Lett.*, 2008, **452**, 306–314.

73. A. de Leon, A. F. Jalbout, and V. A. Basiuk, *Int. J. Quantum. Chem.*, 2009, **110**, 953–959.

74. J. E. Kim and M. Lee, *Biochem. Biophys. Res. Commun.*, 2003, **303**, 576–579.

75. L. Xie, Y. Luo, D. Lin, W. Xi, X. Yang, and G. Wei, *Nanoscale*, 2014, **6**, 9752–9762.

76. S. A. Andujar, F. Lugli, S. Höfinger, R. D. Enriz, and F. Zerbetto, *Phys. Chem. Chem. Phys.*, 2012, **14**, 8599–8607.

77. M. Mahmoudi, H. R. Kalhor, S. Laurent, and I. Lynch, *Nanoscale*, 2013, **5**, 2570–2588.

78. S. H. Friedman, D. L. DeCamp, R. P. Sijbesma, G. Srdanov, F. Wudl, and G. L. Kenyon, *J. Am. Chem. Soc.*, 1993, **115**, 6506–6509.

79. R. Sijbesma, G. Srdanov, F. Wudl, J. A. Castoro, C. Wilkins, S. H. Friedman, D. L. DeCamp, and G. L. Kenyon, *J. Am. Chem. Soc.*, 1993, **115**, 6510–6512.

80. B.-X. Chen, S. R. Wilson, M. Das, D. J. Coughlin, and B. F. Erlanger, *Proc. Natl. Acad. Sci. USA*, 1998, **95**, 10809–10813.

81. B. C. Braden, F. A. Goldbaum, B. X. Chen, A. N. Kirschner, S. R. Wilson, and B. F. Erlanger, *Proc. Natl. Acad. Sci. USA*, 2000, **97**, 12193–12197.

82. M. F. Meidine, P. B. Hitchcock, H. W. Kroto, R. Taylor, and D. R. M. Walton, *J. Chem. Soc., Chem. Commun.*, 1992, 1534–1537.

83. W. H. Noon, Y. Kong, and J. Ma, *Proc. Natl. Acad. Sci. USA*, 2002, **99 Suppl 2**, 6466–6470.

84. T. Mashino, K. Shimotohno, N. Ikegami, D. Nishikawa, K. Okuda, K. Takahashi, S. Nakamura, and M. Mochizuki, *Bioorg. Med. Chem. Lett.*, 2005, **15**, 1107–1109.

85. J. Shang, T. A. Ratnikova, S. Anttalainen, E. Salonen, P. C. Ke, and H. T. Knap, *Nanotechnology*, 2009, **20**, 415101–415109.

86. S. Durdagi, C. T. Supuran, T. A. Strom, N. Doostdar, M. K. Kumar, A. R. Barron, T. Mavromoustakos, and M. G. Papadopoulos, *J. Chem. Inf. Model.*, 2009, **49**, 1139–1143.

87. P. Nedumpully Govindan, L. Monticelli, and E. Salonen, *J. Phys. Chem. B*, 2012, **116**, 10676–11683.

88. X. Meng, B. Li, Z. Chen, L. Yao, D. Zhao, X. Yang, M. He, and Q. Yu, *J. Enzyme Inhib. Med. Chem.*, 2007, **22**, 293–296.

89. X. Bingshe, L. Xuguang, Y. Xiaoqin, Q. Jinli, and J. Weijun, *MRS Proc.*, 2011, **675**, W7.4.1.

90. B. Belgorodsky, L. Fadeev, V. Ittah, H. Benyamini, S. Zelner, D. Huppert, A. B. Kotlyar, and M. Gozin, *Bioconjug. Chem.*, 2005, **16**, 1058–1062.

91. K. H. Park, M. Chhowalla, Z. Iqbal, and F. Sesti, *J. Biol. Chem.*, 2003, **278**, 50212–50216.

92. S.-T. Yang, H. Wang, L. Guo, Y. Gao, Y. Liu, and A. Cao, *Nanotechnology*, 2008, **19**, 395101–39518.

93. N. Iwata, T. Mukai, Y. N. Yamakoshi, S. Haraa, T. Yanase, M. Shoji, T. Endo, and N. Miyata, *Fullerenes, Nanotub. Carbon Nanostructures*, 1998, **6**, 213–226.

94. T. Mashino, K. Okuda, T. Hirota, M. Hirobe, T. Nagano, and M. Mochizuki, *Fuller. Sci. Technol.*, 2001, **9**, 191–196.

95. H. Jin, W. Q. Chen, X. W. Tang, L. Y. Chiang, C. Y. Yang, J. V Schloss, and J. Y. Wu, *J. Neurosci. Res.*, 2000, **62**, 600–607.

96. M. Calvaresi and F. Zerbetto, *ACS Nano*, 2010, **4**, 2283–2299.

97. G. Pastorin, S. Marchesan, J. Hoebeke, T. Da Ros, L. Ehret-Sabatier, J.-P. Briand, M. Prato, and A. Bianco, *Org. Biomol. Chem.*, 2006, **4**, 2556–2562.

98. S. Kraszewski, M. Tarek, W. Treptow, and C. Ramseyer, *ACS Nano*, 2010, **4**, 4158–4164.

99. E. M. Pérez and N. Martín, *Chem. Soc. Rev.*, 2008, **37**, 1512–1519.

100. D. Canevet, E. M. Pérez, and N. Martín, *Angew. Chem. Int. Ed.*, 2011, **50**, 9248–9259.

101. M. Calvaresi and F. Zerbetto, *Nanoscale*, 2011, **3**, 2873–2881.

102. S. Mecozzi and J. Rebek, Jr., *Chem. - A Eur. J.*, 1998, **4**, 1016–1022.

103. L. Pirodini, D. Bonifazi, B. Cantadori, P. Braiuca, M. Campagnolo, R. De Zorzi, S. Geremia, F. Diederich, and E. Dalcanale, *Tetrahedron*, 2006, **62**, 2008–2015.

104. M. Calvaresi, F. Arnesano, S. Bonacchi, A. Bottoni, V. Calò, S. Conte, G. Falini, S. Fermani, M. Losacco, M. Montalti, G. Natile, L. Prodi, F. Sparla, and F. Zerbetto, *ACS Nano*, 2014, **8**, 1871–1877.

105. M. Calvaresi, S. Hoefinger, and F. Zerbetto, *Chem. - A Eur. J.*, 2012, **18**, 4308–4313.

106. A. de Leon, A. F. Jalbout, and V. A. Basiuk, *Chem. Phys. Lett.*, 2008, **457**, 185–190.

107. A. de Leon, A. F. Jalbout, and V. A. Basiuk, *Comput. Mater. Sci.*, 2008, **44**, 310–315.

108. E. A. Meyer, R. K. Castellano, and F. Diederich, *Angew. Chem. Int. Ed.*, 2003, **42**, 1210–1250.

109. S. Wang, E. S. Humphreys, S.-Y. Chung, D. F. Delduco, S. R. Lustig, H. Wang, K. N. Parker, N. W. Rizzo, S. Subramoney, Y.-M. Chiang, and A. Jagota, *Nat. Mater.*, 2003, **2**, 196–200.

110. S. Az'hari and Y. Ghayeb, *Mol. Simul.*, 2014, **40**, 392–398.

111. J. Aihara, *J. Phys. Chem.*, 1994, **98**, 9773–9776.

112. C. D. Sherrill, B. G. Sumpter, M. O. Sinnokrot, M. S. Marshall, E. G. Hohenstein, R. C. Walker, and I. R. Gould, *J. Comput. Chem.*, 2009, **30**, 2187–2193.

113. C. D. Sherrill, *Acc. Chem. Res.*, 2013, **46**, 1020–1028.

114. Z. Yang, Z. Wang, X. Tian, P. Xiu, and R. Zhou, *J. Chem. Phys.*, 2012, **136**, 025103–025113.

115. H. Xie, E. J. Becraft, R. H. Baughman, A. B. Dalton, and G. R. Dieckmann, *J. Pept. Sci.*, 2008, **14**, 139–151.

116. C. Wang, S. Li, R. Zhang, and Z. Lin, *Nanoscale*, 2012, **4**, 1146–1153.

117. W. Fan, J. Zeng, and R. Zhang, *J. Chem. Theory Comput.*, 2009, **5**, 2879–2885.

118. G. R. Dieckmann, A. B. Dalton, P. a Johnson, J. Razal, J. Chen, G. M. Giordano, E. Muñoz, I. H. Musselman, R. H. Baughman, and R. K. Draper, *J. Am. Chem. Soc.*, 2003, **125**, 1770–1777.

119. V. Zorbas, A. Ortiz-Acevedo, A. B. Dalton, M. M. Yoshida, G. R. Dieckmann, R. K. Draper, R. H. Baughman, M. Jose-Yacaman, and I. H. Musselman, *J. Am. Chem. Soc.*, 2004, **126**, 7222–7227.

120. V. Zorbas, A. L. Smith, H. Xie, A. Ortiz-Acevedo, A. B. Dalton, G. R. Dieckmann, R. K. Draper, R. H. Baughman, and I. H. Musselman, *J. Am. Chem. Soc.*, 2005, **127**, 12323–12328.

121. E. J. Wallace, R. S. G. D'Rozario, B. M. Sanchez, and M. S. P. Sansom, *Nanoscale*, 2010, **2**, 967–975.

122. C.-C. Chiu, G. R. Dieckmann, and S. O. Nielsen, *J. Phys. Chem. B*, 2008, **112**, 16326–16333.

123. C.-C. Chiu, G. R. Dieckmann, and S. O. Nielsen, *Biopolymers*, 2009, **92**, 156–163.

124. G. Grigoryan, Y. H. Kim, R. Acharya, K. Axelrod, R. M. Jain, L. Willis, M. Drndic, J. M. Kikkawa, and W. F. DeGrado, *Science*, 2011, **332**, 1071–1076.

125. A. K. Jana and N. Sengupta, *Biophys. J.*, 2012, **102**, 1889–1896.

126. A. K. Jana, J. C. Jose, and N. Sengupta, *Phys. Chem. Chem. Phys.*, 2013, **15**, 837–844.

127. A. Hirano, T. Tanaka, H. Kataura, and T. Kameda, *Chem. - A Eur. J.*, 2014, **20**, 4922–4930.

128. G. Zuo, Q. Huang, G. Wei, R. Zhou, and H. Fang, *ACS Nano*, 2010, **4**, 7508–7514.

129. G. Zuo, W. Gu, H. Fang, and R. Zhou, *J. Phys. Chem. C*, 2011, **115**, 12322–12328.

130. M. Turabekova, B. Rasulev, M. Theodore, J. Jackman, D. Leszczynska, and J. Leszczynski, *Nanoscale*, 2014, **6**, 3488–3495.

131. B. F. Erlanger, B.-X. Chen, M. Zhu, and L. Brus, *Nano Lett.*, 2001, **1**, 465–467.

132. R. Marega, F. De Leo, F. Pineux, J. Sgrignani, A. Magistrato, A. D. Naik, Y. Garcia, L. Flamant, C. Michiels, and D. Bonifazi, *Adv. Funct. Mater.*, 2013, **23**, 3173–3184.

133. F. De Leo, J. Sgrignani, D. Bonifazi, and A. Magistrato, *Chem. - A Eur. J.*, 2013, **19**, 12281–12293.

134. F. Karchemsky, E. Drug, E. Mashiach-Farkash, L. Fadeev, H. J. Wolfson, M. Gozin, and O. Regev, *Colloid. Surface. B*, 2013, **112**, 16–22.

135. C. Ge, J. Du, L. Zhao, L. Wang, Y. Liu, D. Li, Y. Yang, R. Zhou, Y. Zhao, Z. Chai, and C. Chen, *Proc. Natl. Acad. Sci. USA*, 2011, **108**, 16968–16973.

136. K. Matsuura, T. Saito, T. Okazaki, S. Ohshima, M. Yumura, and S. Iijima, *Chem. Phys. Lett.*, 2006, **429**, 497–502.

137. P. Goldberg-Oppenheimer and O. Regev, *Small*, 2007, **3**, 1894–1899.

138. J.-W. Shen, T. Wu, Q. Wang, and Y. Kang, *Biomaterials*, 2008, **29**, 3847–3855.

139. D. Nepal and K. E. Geckeler, *Small*, 2007, **3**, 1259–1265.

140. D. Nepal and K. E. Geckeler, *Small*, 2006, **2**, 406–412.

141. N. Dragneva, W. B. Floriano, D. Stauffer, R. C. Mawhinney, G. Fanchini, and O. Rubel, *J. Chem. Phys.*, 2013, **139**, 174711–174717.

142. R. B. Pandey, Z. Kuang, B. L. Farmer, S. S. Kim, and R. R. Naik, *Soft Matter*, 2012, **8**, 9101–9110.

143. A. N. Camden, S. A. Barr, and R. J. Berry, *J. Phys. Chem. B*, 2013, **117**, 10691–10697.

144. J. Kyte and R. F. Doolittle, *J. Mol. Biol.*, 1982, **157**, 105–132.

145. Y. Guo, X. Lu, J. Weng, and Y. Leng, *J. Phys. Chem. C*, 2013, **117**, 5708–5717.

146. W. Qin, X. Li, W.-W. Bian, X.-J. Fan, and J.-Y. Qi, *Biomaterials*, 2010, **31**, 1007–1016.

147. A. Riemann and B. Nelson, *Langmuir*, 2009, **25**, 4522–4525.

148. A. Riemann and B. E. Owens, *Surf. Sci.*, 2010, **604**, 2084–2090.

149. B. E. Owens and A. Riemann, *Surf. Sci.*, 2014, **624**, 118–129.

150. C. Rajesh, C. Majumder, H. Mizuseki, and Y. Kawazoe, *J. Chem. Phys.*, 2009, **130**, 124911–124917.

151. Y. Zhang, C. Wu, S. Guo, and J. Zhang, *Nanotechnol. Rev.*, 2013, **2**, 27–45.

152. Y. Cui, S. N. Kim, S. E. Jones, L. L. Wissler, R. R. Naik, and M. C. McAlpine, *Nano Lett.*, 2010, **10**, 4559–4565.

153. J. Katoch, S. N. Kim, Z. Kuang, B. L. Farmer, R. R. Naik, S. A. Tatulian, and M. Ishigami, *Nano Lett.*, 2012, **12**, 2342–2346.

154. S. N. Kim, Z. Kuang, J. M. Slocik, S. E. Jones, Y. Cui, B. L. Farmer, M. C. McAlpine, and R. R. Naik, *J. Am. Chem. Soc.*, 2011, **133**, 14480–14483.

155. C. R. So, Y. Hayamizu, H. Yazici, C. Gresswell, D. Khatayevich, C. Tamerler, and M. Sarikaya, *ACS Nano*, 2012, **6**, 1648–1656.

156. D. Khatayevich, T. Page, C. Gresswell, Y. Hayamizu, W. Grady, and M. Sarikaya, *Small*, 2014, **10**, 1505–1513.

157. G. Gianese, V. Rosato, F. Cleri, M. Celino, and P. Morales, *J. Phys. Chem. B*, 2009, **113**, 12105–12112.

158. S. M. Tomásio and T. R. Walsh, *J. Phys. Chem. C*, 2009, **113**, 8778–8785.

159. N. Todorova, A. J. Makarucha, N. D. M. Hine, A. A. Mostofi, and I. Yarovsky, *PLoS Comput. Biol.*, 2013, **9**, 1003360–1003373.

160. G. Zuo, X. Zhou, Q. Huang, H. Fang, and R. Zhou, *J. Phys. Chem. C*, 2011, **115**, 23323–23328.

161. J. Guo, J. Li, Y. Zhang, X. Jin, H. Liu, and X. Yao, *PLoS One*, 2013, **8**, 65579–65589.

162. K. Nakanishi, T. Sakiyama, and K. Imamura, *J. Biosci. Bioeng.*, 2001, **91**, 233–244.

163. G. Raffaini and F. Ganazzoli, *Langmuir*, 2003, **19**, 3403–3412.

164. G. Raffaini and F. Ganazzoli, *J. Biomed. Mater. Res.*, 2006, **76**, 638–645.

165. G. Raffaini and F. Ganazzoli, *Langmuir*, 2004, **20**, 3371–3378.

166. G. Raffaini and F. Ganazzoli, *Langmuir*, 2010, **26**, 5679–5689.

167. J. Guo, X. Yao, L. Ning, Q. Wang, and H. Liu, *RSC Adv.*, 2014, **4**, 9953–9962.

168. G. Raffaini and F. Ganazzoli, *Macromol. Biosci.*, 2007, **7**, 552–566.

169. G. Raffaini and F. Ganazzoli, *J. Phys. Chem. B*, 2004, **108**, 13850–13854.

170. C. L. Brown, I. A. Aksay, D. A. Saville, and M. H. Hecht, *J. Am. Chem. Soc.*, 2002, **124**, 6846–6848.

171. X. Mao, Y. Guo, Y. Luo, L. Niu, L. Liu, X. Ma, H. Wang, Y. Yang, G. Wei, and C. Wang, *J. Am. Chem. Soc.*, 2013, **135**, 2181–2187.

172. P. Laaksonen, M. Kainlauri, T. Laaksonen, A. Shchepetov, H. Jiang, J. Ahopelto, and M. B. Linder, *Angew. Chem. Int. Ed.*, 2010, **49**, 4946–4949.

173. G. Raffaini and F. Ganazzoli, *Langmuir*, 2013, **29**, 4883–4893.

174. K. Lindorff-Larsen, S. Piana, R. O. Dror, and D. E. Shaw, *Science (80-.).*, 2011, **334**, 517–20.

175. R. O. Dror, R. M. Dirks, J. P. Grossman, H. Xu, and D. E. Shaw, *Annu. Rev. Biophys.*, 2012, **41**, 429–452.

176. P. Tiwary and M. Parrinello, *Phys. Rev. Lett.*, 2013, **111**, 230602.

177. C. D. Christ, A. E. Mark, and W. F. van Gunsteren, *J. Comput. Chem.*, 2010, **31**, 1569–1582.